2019

The Magnetocaloric Effect & Performance of Magnetocaloric Materials in a 1D Active Magnetic Regenerator Simulation

Daniel Nicholas Bayer
Wright State University

The Magnetocaloric Effect & Performance of Magnetocaloric Materials in a 1D Active Magnetic Regenerator Simulation

A thesis submitted in partial fulfillment of the
requirements for the degree of
Master of Science

By

DANIEL NICHOLAS BAYER
B.S., Wright State University, 2018

2019
WRIGHT STATE UNIVERSITY

WRIGHT STATE UNIVERSITY

GRADUATE SCHOOL

December 13, 2019

I HEREBY RECOMMEND THAT THE THESIS PREPARED UNDER MY SUPERVISION BY Daniel Nicholas Bayer ENTITLED The Magnetocaloric Effect & Performance of Magnetocaloric Materials in a 1D Active Magnetic Regenerator Simulation BE ACCEPTED IN PARTIAL FULFILLMENT OF THE REQUIREMENTS FOR THE DEGREE OF Master of Science.

Gregory Kozlowski, Ph.D.
Thesis Director

Jason Deibel, Ph.D.
Chair, Department of Physics

Committee on Final Examination

Zafer Turgut, Ph.D.
Thesis Co-Director

Gregory Kozlowski, Ph.D.

Brent Foy, Ph.D.

Barry Milligan, Ph.D.
Interim Dean of the Graduate School

ABSTRACT

Bayer, Daniel Nicholas. M.S. Department of Physics, Wright State University, 2019. The Magnetocaloric Effect & Performance of Magnetocaloric Materials in a 1D Active Magnetic Regenerator Simulation.

Active magnetic regenerators (AMRs) operate according to the magnetothermal phenomenon known as the magnetocaloric effect (MCE), and are at the forefront of magnetic cooling technology. AMR simulations have been shown to be useful tools in predicting the performance of different magnetocaloric materials (MCMs) without the need to develop a physical prototype. In a search to determine the set of operational parameters which would maximize MCM performance, a 1D simulation of an AMR device has been developed in Matlab. Gadolinium, the most well-documented MCM, is used as a benchmark material to study the effects of varying certain operational parameters such as mass flow rate, cycle frequency, amount of MCM mass, strength of applied magnetic field, and regenerator temperature span. In conjunction with the AMR simulation, a mean-field model of ferromagnetic materials is developed in Matlab in order to obtain the magnetothermal properties of gadolinium. Upon determining the effects of various operational parameters, a study of the performance of a $Ni_{0.50}Mn_{0.19}Cu_{0.06}Ga_{0.25}$ alloy after a stress-assisted thermal cycling (SATC) treatment is conducted. The effect of heat capacity on MCM performance is carried out by creating hypothetical adiabatic temperature change and heat capacity curves, with other material properties similar to those of the Ni-Mn-Cu-Ga alloy.

TABLE OF CONTENTS

Page

LIST OF FIGURES

Page

LIST OF TABLES

Page

NOMENCLATURE

A_c	Regenerator cross-sectional area	$\dot{m}_f$	Mass flow rate
a_s	Volume-specific surface area	N	Number of atoms
B	Applied magnetic field	N_{Av}	Avogadro's number
B_J	Brillouin function	Nu	Nusselt number
c	Specific heat capacity	p	Pressure
$\bar{c}_s$	MCM maximum heat capacity at zero field	Pr	Prandtl number
d	Regenerator bed diameter	$\dot{Q}_{ref}$	Absorbed heat
d_h	Hydraulic diameter	$\dot{Q}_{rej}$	Rejected heat
d_p	Particle diameter	R	Universal gas constant
E_n	Eigenvalues of the Hamiltonian	Re	Reynolds number
F	Free energy	S	Entropy
f	Frequency	T	Temperature
g_J	Landé factor	T_C	Curie temperature
$\mathcal{H}$	Hamiltonian	T_D	Debye temperature
h	Convective heat transfer coefficient	T_M	Martensitic start temperature
I	Exchange integral	t	Time
J	Total angular momentum	t_c	AMR cycle duration
k	Thermal conductivity	t_r	Mean transit time
k_B	Boltzmann constant	U	Internal energy
L	Regenerator length	V	Volume
M	Magnetization	v	Interstitial velocity
m	Mass	v_D	Darcy velocity

W	Work	***Subscripts***	
X	Brillouin function argument	*CHEX*	Cold heat exchanger
x	Position along regenerator bed	*eff*	Effective
Z	Partition function	*el*	Electronic
		f	Fluid phase
Greek		*HHEX*	Hot heat exchanger
γ	Electronic heat capacity coefficient	*lat*	Lattice
ε	Porosity	*mag*	Magnetic
η	Pump efficiency	*s*	Solid phase
λ	Weiss molecular field coefficient		
μ_B	Bohr magneton	***Acronyms***	
ρ	Density	*AMR*	Active magnetic regenerator
σ	Reduced magnetization	*FOMT*	First-order magnetic transition
Φ	Utilization factor	*MCE*	Magnetocaloric effect
		MCM	Magnetocaloric material
Superscripts		*MCS*	Magnetic cooling system
*	Reduced quantity	*SATC*	Stress-assisted thermal cycling
M	Martensitic	*SOMT*	Second-order magnetic transition

ACKNOWLEDGEMENTS

I would first like to acknowledge my Thesis Advisor, Dr. Gregory Kozlowski, for informing of the opportunity to do research at WPAFB/AFRL. I am extremely fortunate to have been in contact with someone so diligent and determined to bring me onboard such an amazing research opportunity, and for the many resources he shared with me throughout my project. It has been a long journey and he has been with me through its entirety.

I also want to acknowledge my government POC and Research Advisor, Dr. Zafer Turgut, for his many efforts to get me access onto the base and do research within his group under such difficult conditions. I am very grateful for the hard work he did to welcome me into his group, and for his continual kindness and patience throughout the duration of this project. I would like to thank Dr. Michael McLeod, another AFRL colleague, for his help in understanding the magnetocaloric effect and magnetocaloric materials. I also want to thank the many people who helped me work on my simulation throughout the course of my project including Dr. Nicholas Niedbalski, Dr. Mohamed Sulman, and Dr. Ajani Ross. Without the aid of these individuals I would not have the understanding of Matlab that I do today. I am beyond thankful for the time they gave me.

Lastly, I would like to thank my friends and family for the support I was given in furthering my education. It has been a long and difficult journey, and I am grateful to have such a wonderful group of people by my side along the way.

I. GOALS

The goal of this project is to develop a 1D numerical simulation of an AMR-type magnetic cooling system for the purpose of testing the performance of various magnetocaloric materials. Gadolinium is to be used as a reference material in order to validate the simulation since it is commonly used as a benchmark material in other simulations and is by far the most extensively studied magnetocaloric material. A mean-field model of magnetic materials is developed in conjunction with the AMR simulation so that the relevant physical and magnetic properties of gadolinium, or other second order magnetic transition materials, can be calculated and used as inputs in the AMR simulation. The main material property inputs that the simulation requires are the heat capacity and adiabatic temperature change at varying magnetic field strengths, thermal conductivity, and mass density. Of these four required quantities, the mean field model provides the heat capacity and adiabatic temperature change for different magnetic field strengths. Upon verifying the AMR simulation and assessing the effect of main operational parameters using gadolinium, the performance of other magnetocaloric materials, namely a $Ni_{0.50}Mn_{0.19}Cu_{0.06}Ga_{0.25}$ Heusler alloy after stress assisted thermal cycling (SATC), may be evaluated. Furthermore, a study of the effect that heat capacity has on MCM performance is evaluated by means of creating hypothetical adiabatic temperature change and heat capacity curves.

II. INTRODUCTION

Magnetic cooling is an emerging solid-state cooling technology that, within the past few decades, has shown great potential as an alternative to other types of cooling systems, namely vapor compression systems. While magnetic cooling has been used for many years in low temperature applications, such as cryogenics and gas liquefaction, its applications in the room temperature regime has been far more scarce. Since the development of the first room temperature magnetic cooling system by Brown in the mid-1970s [1], researchers have been vigilant to study the designs and types of materials that would optimize this technology and push it into the mainstream.

Cooling devices that operate around room temperature environments are heavily represented by vapor compression-type systems. However, vapor compression technology has been improved over the past century and has basically achieved its apex in terms of development, meaning that any further improvements to efficiency seem unlikely [2]. Magnetic cooling systems (MCSs) hold a few advantages over conventional vapor compression systems. They are able to operate at higher efficiencies, up to 60% of the theoretical Carnot efficiency, and use no harmful gasses such as chlorofluorocarbons (CFCs) making MCSs a green technology [3]. Through the use of liquid heat transfer fluids (HTFs) instead of gasses, MCSs have a reduced likelihood of fluid leakage, helping to fortify their operative reliability. For MCSs operating around room temperature, it is common to see water, or a water-glycol mixture used as a HTF due to water's favorable thermal properties and ease of availability.

Magnetic cooling systems operate based on the materials phenomenon known as the magnetocaloric effect (MCE). Simply put, the MCE is observed as a temperature

change in a magnetic material when it is exposed to an external magnetic field. Through proper insulation of the magnetic material, so that there is no heat exchange between it and the environment, this temperature change is considered adiabatic. For certain ferromagnetic materials exposed to a magnetic field, this change in temperature is positive, causing the material to heat up. Other types of MCMs display a negative change in temperature upon exposure to a magnetic field, which is the manifestation of the inverse magnetocaloric effect. The origin of the adiabatic temperature change is due to variation of the magnetic entropy during magnetization/demagnetization processes. The MCE can be observed in all magnetic materials, as it is an intrinsic property, however not all of them exhibit a strong enough MCE for construction of a heat pump.

The magnetic materials that do possess a large enough MCE to be considered for magnetic cooling purposes are referred to as magnetocaloric materials (MCMs). Within this great family of materials, MCMs are further classified by the strength of their MCE as well as the order of their magnetic transition at their Curie temperature. The MCE is casually quantified in terms of just the adiabatic temperature change. A more precise quantification of the MCE, however, also considers the magnitude and shape of the magnetic entropy change under isothermal conditions. The isothermal magnetic entropy change of a MCM gives insight into how much heat can be drawn per operative cycle in a MCS [4].

The main focus of this work will be on the performance of magnetocaloric materials by means of a 1D AMR simulation implemented in Matlab. An AMR is a specific design of regenerator used in magnetic cooling systems and will be discussed in detail in *Sec. 2.2*. Due to the scarcity of readily available magnetocaloric material data, a

mean-field model of ferromagnetic materials is developed for gadolinium in conjunction with the AMR simulation. The mean-field model is often employed in AMR simulations in order to provide thermodynamically accurate material data and will provide a strong base for model verification and operational parameter testing. Once the model has verified, the influence of the main AMR operational parameters is determined using gadolinium as a reference material.

A study into the effects of stress-assisted thermal cycling (SATC) on magnetocaloric material performance is conducted as well. Experimental material data for a $Ni_{0.50}Mn_{0.19}Cu_{0.06}Ga_{0.25}$ alloy after a SATC treatment is input into the AMR simulation so that the performance of the material may be tested. To study the effect that heat capacity has on MCM performance, hypothetical adiabatic temperature and heat capacity curves are created of varying magnitude. This hypothetical material is simulated using material properties similar to those of the Ni-Mn-Cu-Ga alloy, and is simulated under similar working conditions.

In *Ch. II* of this thesis, general topics such as the magnetocaloric effect, active magnetic regenerator (AMR), and magnetocaloric materials are discussed to provide a base of understanding for the physical aspects of the AMR simulations.

Ch. III states the main objective of this thesis which, in general, is to create a 1D AMR simulator in order to predict various MCM performance and test the effects of various operational parameters.

Ch. IV discusses the foundation of both the mean-field model and 1D AMR simulator developed in Matlab, presenting the relevant equations used and descriptions of how the simulations are implemented in Matlab.

The results of the simulations performed in this thesis are presented in *Ch. V*. The outputs of the mean-field model and AMR simulator for gadolinium are presented first, with the results of the Ni-Mn-Cu-Ga alloy after SATC and hypothetical material appearing after.

The conclusions drawn from all simulation results are presented in *Ch. VI*, along with suggestions for moving forward with the AMR simulator.

The code in its entirety for the mean-field model and AMR simulator with relevant functions that are called during execution are listed in *App. A* and *App. B*, respectively. A brief exploration into the range of uncertainty of the AMR simulator is presented in *App. C*.

Through the development of the mean-field model and AMR simulator, the goal of this project may be realized. The mean-field model allows for the magnetothermal properties of SOMT materials to be calculated for use in the AMR simulation. For materials of the FOMT-type, their measured magnetothermal properties may be input into the AMR simulator and their performance may then be evaluated. In this thesis, the magnetothermal properties of gadolinium are evaluated using the mean-field model and its performance in the AMR simulator is used as a reference for other materials' performance. Upon characterizing gadolinium in the AMR simulation, the performance of a Ni-Mn-Cu-Ga alloy is then determined.

III. THEORETICAL INTRODUCTION

3.1 THE MAGNETOCALORIC EFFECT

Magnetic cooling systems operate based on the magneto-thermodynamic phenomenon known as the magnetocaloric effect (MCE). In magnetic materials the MCE can be observed as a temperature change when the material is exposed to a varying, external magnetic field under adiabatic conditions. While all magnetic materials intrinsically display the MCE, certain materials called magnetocaloric materials (MCMs) display a strong enough MCE to be useful for the purposes of magnetic cooling systems.

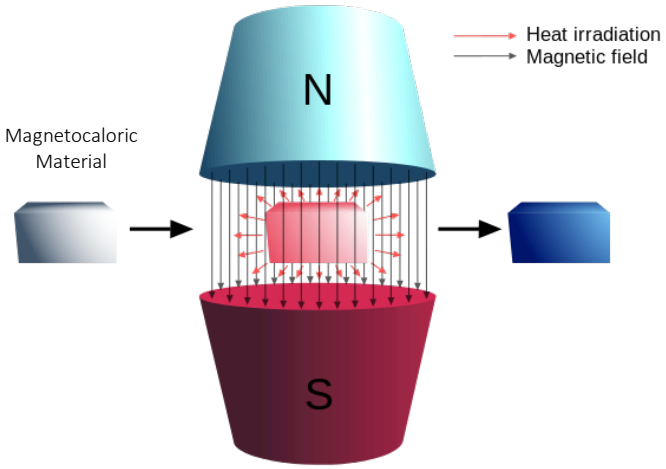

Figure 1: Illustration of the magnetocaloric effect.

For many magnetocaloric materials, the MCE causes an increase in temperature when exposed to a magnetic field and a decrease in temperature when the field is removed. In order to explain how the MCE arises in these magnetic materials, it is

common to look at the total variation of entropy in a magnetic system, as Tishin does in his book [5]. By considering a system of spins, either ferromagnetic or paramagnetic around its magnetic ordering temperature, the total entropy can be described, in general, by three individual contributions: a lattice, magnetic, and electronic contribution:

$$S_{Tot} = S_{lat} + S_{mag} + S_{el} \quad (1)$$

For simplicity the electronic contribution to the total entropy is often ignored, as it is negligible when compared to the magnitude of the lattice and magnetic contributions, allowing the total entropy equation to be written as:

$$S_{Tot} = S_{lat} + S_{mag} \quad (2)$$

Here, the lattice contribution to the entropy corresponds to the temperature of the system and the magnetic contribution corresponds to the degree of magnetic ordering.

Since the magnetic field is applied to the material adiabatically (no heat exchange between the material and its surroundings), the change in entropy of the system must remain constant:

$$\Delta S_{Tot} = \Delta S_{lat} + \Delta S_{mag} = 0 \quad (3)$$

When the system is adiabatically exposed to a magnetic field (magnetization) the magnetic moments comprising the system will become ordered and the magnetic contribution to the total entropy will decrease. This means that the lattice contribution, and thus the temperature of the system, must increase in order to keep the total entropy of the system constant. Similarly, for the opposite process, the adiabatic removal of the magnetic field (demagnetization), the temperature of the system will decrease. It is in this adiabatic change of temperature that the MCE manifests itself in magnetic materials.

By exploiting the magnetocaloric effect in suitable materials, a heat pump device can be constructed and used for cooling applications. In order to reinforce the applicability of the MCE to magnetic cooling systems, an analogy can be made to a vapor compression cooling system.

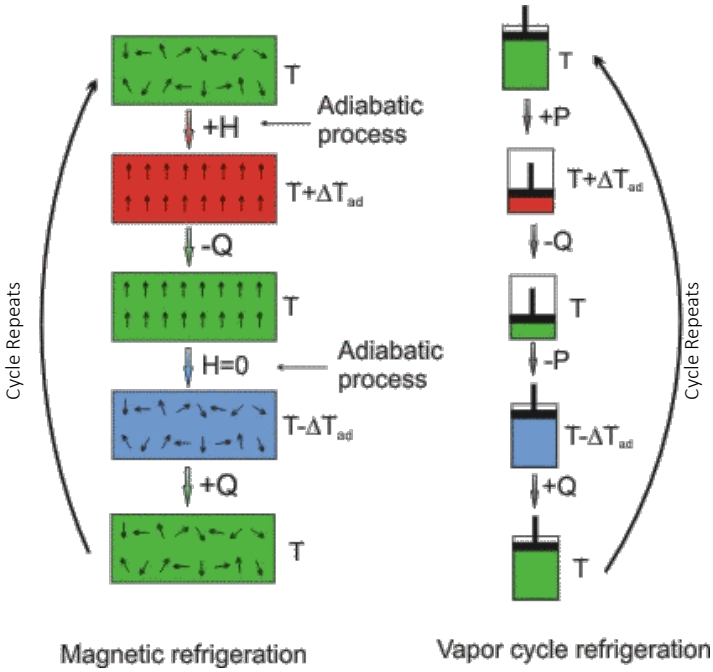

Figure 2: Analogy of magnetic cooling system to vapor compression cooling system.

The main analogy between these two cooling systems is that the application and removal of pressure in a vapor compression system is conceptually the same as the application and removal of a magnetic field in a magnetic cooling system.

Initially, the magnetocaloric material is at some temperature (T) with unordered magnetic moments. By applying a magnetic field, the magnetic moments align, and the temperature of the material increases adiabatically. Excess heat is removed from the system and the temperature of the MCM is brought back down to its initial value. Now the magnetic field is removed, causing the magnetic moments to again become disordered and the temperature of the MCM to decrease. Heat can then be absorbed from

the load, increasing the MCM temperature back to its initial value, and then the cycle repeats itself.

The magnetocaloric effect is often defined by a combination of three quantities: the adiabatic temperature change (ΔT_{ad}), isothermal magnetic entropy change (ΔS_{mag}), and Curie temperature (T_C). The larger the magnitude of the adiabatic temperature change, the greater the magnetocaloric effect will be. While the magnitude of ΔT_{ad} is important, the shape of the curve when plotted against temperature is of importance as well. A wider ΔT_{ad} curve means that the MCE will be applicable to a wider range of operating temperatures. In general, the magnetocaloric effect can be calculated through the following equation for the adiabatic temperature change:

$$\Delta T_{ad} = MCE = -\int_{B_i}^{B_f} \frac{T}{c_p}\left(\frac{\partial M}{\partial T}\right)_B dB \tag{4}$$

where c_p represents the heat capacity at a given magnetic field strength B and M represents the magnetization at that field strength.

The shape and magnitude of the isothermal magnetic entropy change also plays a role in the strength of the MCE. A wider magnetic entropy change indicates that larger amounts of heat can be drawn per operative cycle. Both the adiabatic temperature change and isothermal magnetic entropy change are greatly affected by the strength of the applied magnetic field. As can be seen in *Fig. 3*, the magnitude and width of the magnetic entropy change are increased with increasing magnetic field strength.

The Curie temperature is also an important parameter that influences the magnetocaloric effect in magnetic materials. At the Curie temperature a ferromagnetic material becomes paramagnetic. This change in magnetic properties at the Curie point result in a greater magnetocaloric effect.

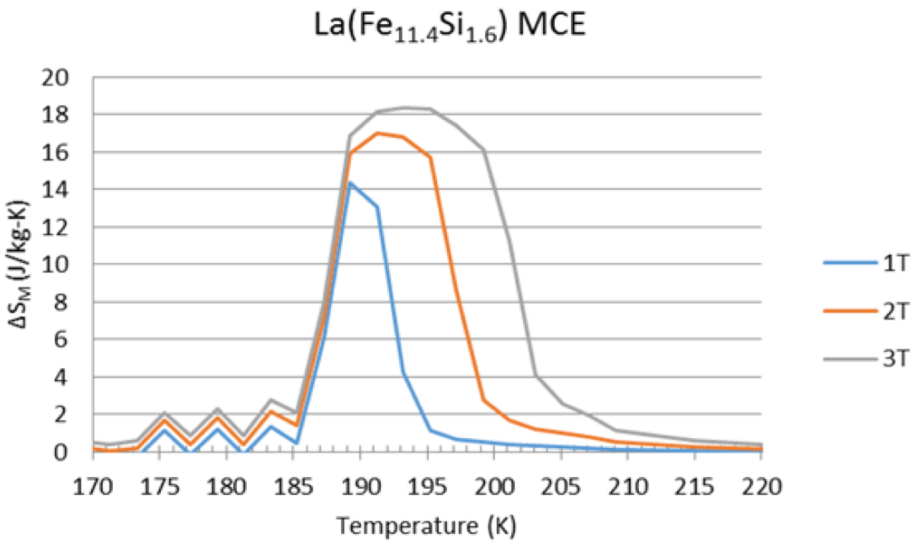

Figure 3: Influence of magnetic field on the isothermal magnetic entropy change.

In selecting a material to be used in a magnetic cooling system, the Curie temperature is considered so that it is included within or very near to the desired operating temperature range of the device.

The description of the magnetocaloric effect thus far has assumed a material displaying a forward MCE: the material heats up when adiabatically exposed to a magnetic field. There exists another family of materials that exhibit an inverse magnetocaloric effect, where the material cools down when adiabatically exposed to a magnetic field. The majority of inverse MCE materials are of the first-order magnetic transition-type, to be described later in *Sec. 2.3*. For example, materials such as gadolinium exhibit a forward MCE in the presence of a magnetic field while materials belonging to the Ni-Mn-Ga family present an inverse MCE.

Inverse MCE materials undergo an increase in magnetic entropy in the presence of an externally applied magnetic field, resulting in a temperature decrease from the corresponding decrease in lattice entropy. For the opposite process of the adiabatic

removal of the magnetic field the material heats up from the accompanying entropy balance that must take place. Forward and inverse MCE materials are operationally the same though, with both undergoing a heating and cooling cycle required by a magnetic cooling system.

3.2 THE ACTIVE MAGNETIC REGENERATOR

The active magnetic regenerator (AMR) is a type of magnetic cooling system that has shown the most promise as an alternative to other types of cooling systems. AMRs use magnetocaloric materials as a solid refrigerant in contrast to other cooling systems which use fluid refrigerants. The magnetocaloric material serves a dual purpose in the AMR: as the refrigerant material and as the regenerator for the heat transfer fluid. The dual purpose that the MCM serves allows the temperature span of the regenerator to be increased further than what is caused by the MCM's adiabatic temperature change. As a result, the AMR has proven to be the only viable type of magnetic cooling system capable of competing with other modern cooling technologies.

An active magnetic regenerator cooling system has five main components, as schematized in *Fig. 4*.

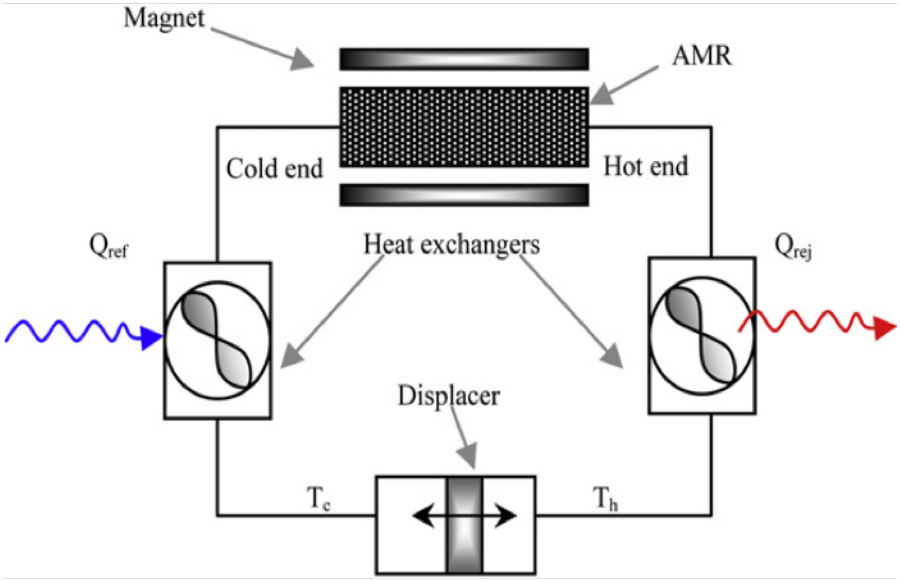

Figure 4: Simplified schematic of an AMR magnetic cooling system [6].

An AMR cooling system consists of a regenerator, magnetization system, pumping system, hot heat exchanger, and cold heat exchanger. The regenerator is composed of the magnetocaloric material and is responsible for creating the temperature span between the heat exchangers. The magnetization system provides the magnetic field necessary for the magnetocaloric effect and determines the operational frequency of the system. The pumping system flows the heat transfer fluid through the regenerator to absorb and supply heat. The heat exchangers are the AMRs connection to the environment by absorbing heat from the load and rejecting heat to the environment. Of these AMR components, the selection of the regenerator bed geometry and magnetization system have the most influence on overall performance.

The three regenerator geometries that are most commonly used are particle packed beds, parallel plates, and pin arrays. The main considerations when selecting a regenerator geometry are the heat transfer coefficient and porosity. The porosity is defined as the ratio of void volume to the total volume of the regenerator, so larger porosity values correspond to less magnetocaloric material contained within the regenerator. Geometries with larger heat transfer coefficients are desirable, as they increase the amount of heat transfer between the MCM and heat transfer fluid. To this extent, particle packed bed regenerator geometries, typically spherical particles, have been extensively used in AMR prototypes. Spherical particle packed beds have the benefit of high heat transfer coefficients at relatively low porosities, although the pressure drop across the regenerator is larger for this type of geometry. *Fig. 5* shows some examples of the three different regenerator geometries.

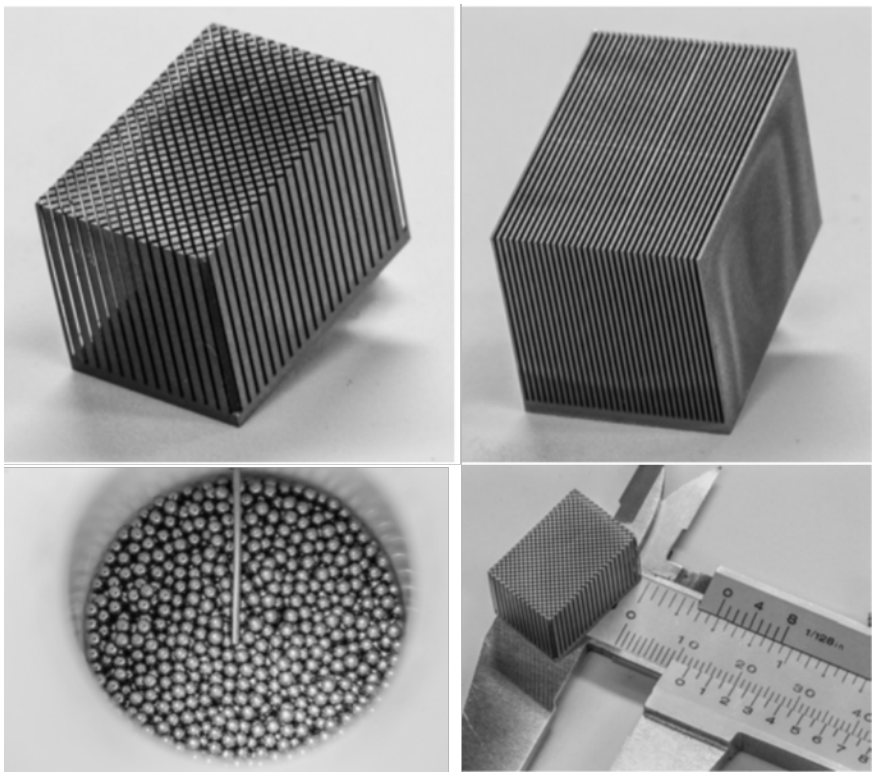

Figure 5: Example AMR geometries and general size [7].

Moving from the top left to bottom right of *Fig. 5* shows the pin array, parallel plate, and spherical particle packed bed regenerator geometries. In the bottom right of the figure the typical regenerator size is shown. AMR regenerators are quite small, usually just a few centimeters long, but are placed in series with one another to create longer beds.

The AMRs magnetization system is also a vital system component. Since the strength of the magnetocaloric effect is heavily dependent on the strength, a magnetization system capable of providing the largest possible magnetic field is preferred. There are two families of magnetization systems that are considered for magnetic cooling systems: permanent magnet assemblies or superconducting magnets. While superconducting magnets are capable of providing much larger fields than permanent magnet assemblies, they require more significant power inputs to the AMR

and reduce the overall efficiency of the device. Due to this, permanent magnet assemblies are often employed in AMR prototypes.

In order to deal with the fact that the regenerator bed needs to be magnetized and demagnetized over an operative cycle, a permanent magnet system known as the Halbach array is often utilized.

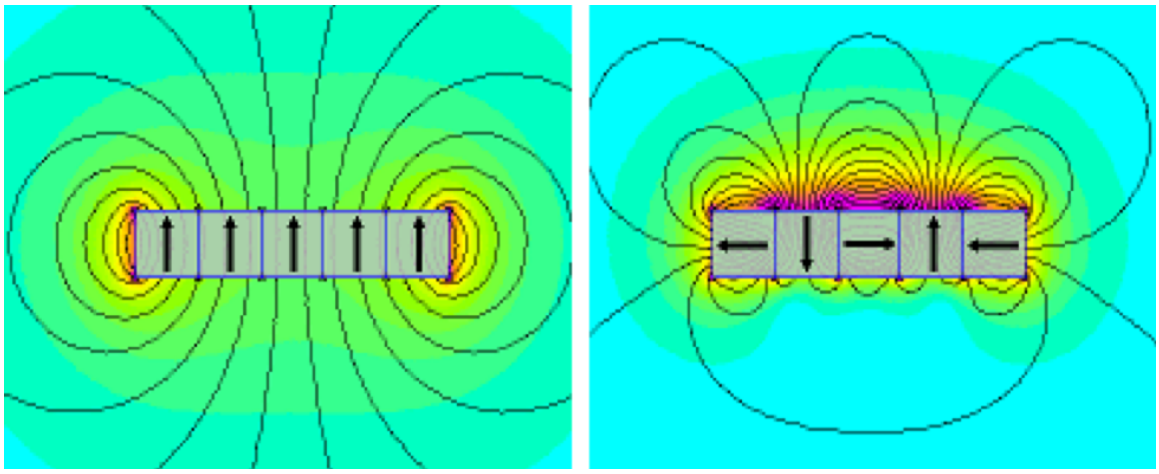

Figure 6: A typical arrangement (left) and Halbach array (right) permanent magnet orientations.

As can be seen from *Fig. 6*, a typical arrangement of permanent magnets produces a uniform magnetic field on either side of the assembly. In the case of a Halbach array, permanent magnets are oriented in such a way that a maximum magnetic field is produced on one side of the assembly while nearly cancelling out to zero field on the other.

For applications to AMR devices a magnetization system design known as the nested Halbach cylinder has shown to be the most viable option for producing moderate strength magnetic fields without the need for a superconducting magnetization system. The same principle of specific magnet orientation that applied to the linear Halbach array

also applies to the cylindrical case. An example of the permanent magnet arrangements for a nested Halbach cylinder can be seen in *Fig. 7*.

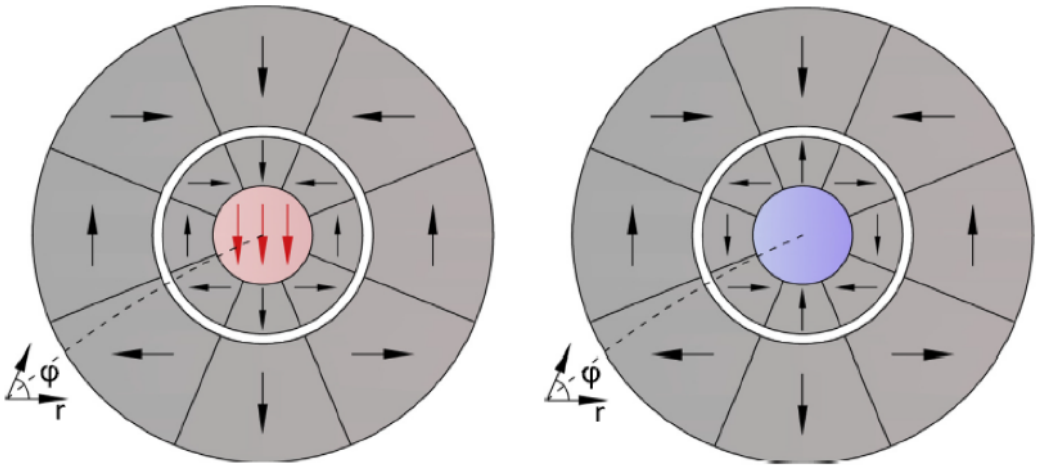

Figure 7: Nested Halbach cylinder magnet orientation [7].

The arrangement of magnets on the left side of *Fig. 7* show the orientation which provides maximum field in the center of the cylinder, while the arrangement on the right shows the orientation resulting in zero field.

Up until recent years, the largest magnitude magnetic field obtainable from permanent magnet system was approximately 1.5 T. With further development of nested Halbach cylinders, and magnet material composition, fields of approximately 1.8 T have been achieved. *Fig. 8* shows maximum magnetic field value, plotted against the length of the cylinder, of a current nested Halbach cylinder design. The most optimal location of a regenerator is in the flat region sitting around 1.8 T of the red line, which represents the Halbach cylinder's length. Within this region of the cylinder the magnetic field is greatest, hence the magnetocaloric effect would be the greatest as well. The blue line in *Fig. 8* denotes the strength of the magnetic field along the cylinder's width.

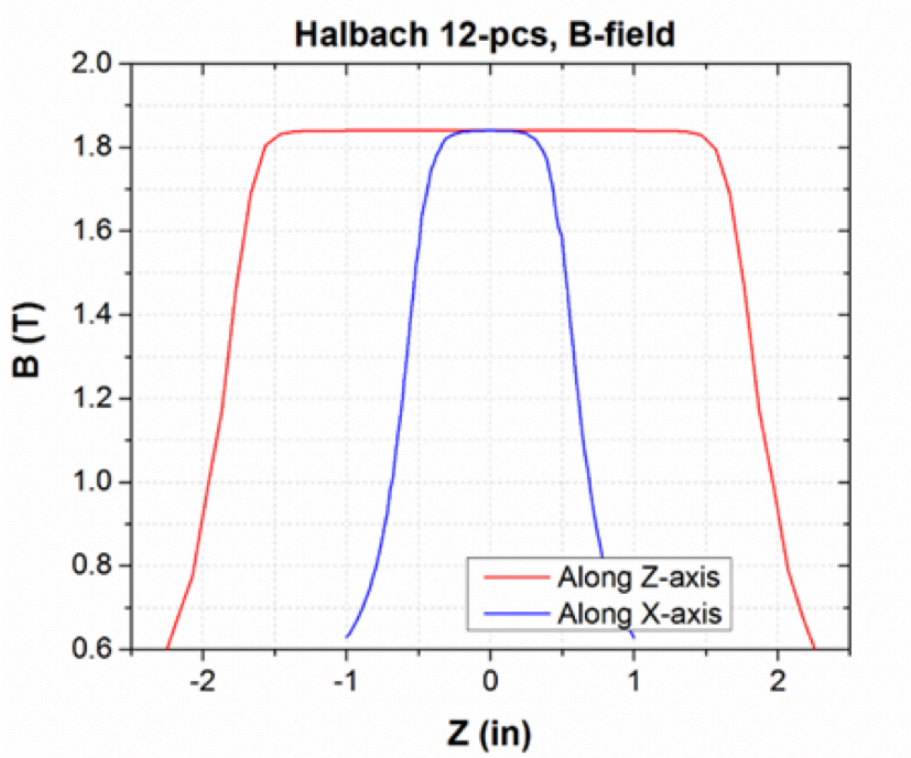

Figure 8: Magnetic field strength distribution of a new generation Halbach cylinder.

These locations where the field is maximum within the Halbach cylinder set limitations on the size of the regenerator to be placed inside.

Active magnetic regenerator cooling systems operate according to a cyclic set of four processes: magnetization, warm blow, demagnetization, and cold blow. This set of processes, called the AMR cycle, are shown in *Fig. 9*. Before explaining each of the steps in the AMR cycle, there are a few things to note in diagram so that it may be better understood. First, the T vs. x plots that can be seen during each step are meant to represent the temperature of the regenerator containing the MCM, with "x" denoting the position inside the regenerator. In this way the plots themselves may be viewed as the regenerator. Second, the dashed lines on the plots show the temperature profile at the beginning of each step and the solid lines show the temperature profile at the end of the step.

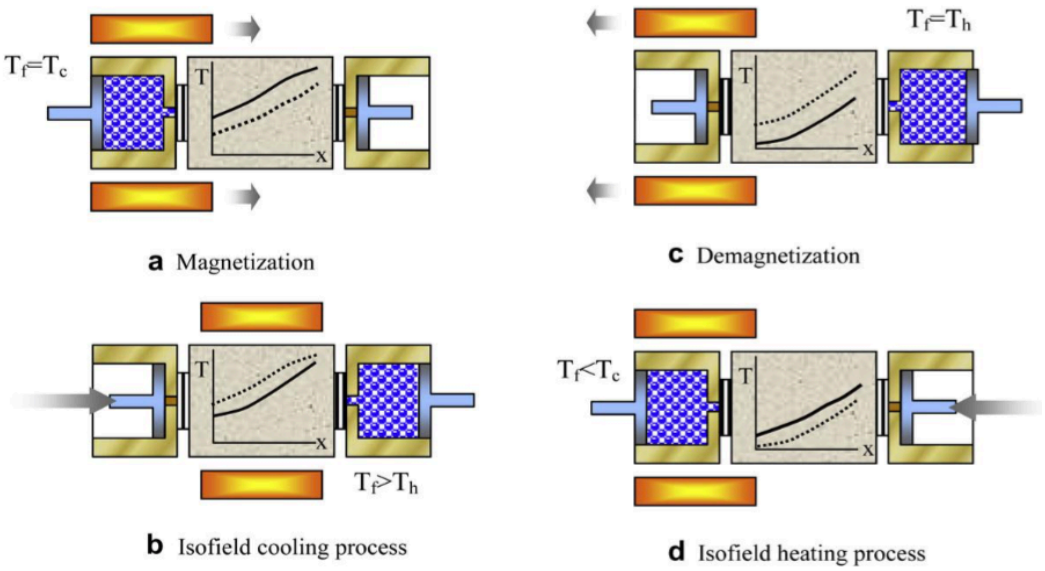

Figure 9: Four stages of the AMR thermodynamic cycle [6].

It can be seen that the solid line of a given step becomes the dashed line of the proceeding step.

The AMR cycle begins with the adiabatic magnetization of the regenerator bed. During this process the MCM contained within the regenerator heats up as a result of the magnetocaloric effect. During the magnetization process there is no fluid flow through the regenerator. The heat transfer fluid is held static in the cold (left) heat exchanger and matches the temperature of this reservoir.

With the magnetic field still applied, the warm blow process begins. In this process the heat transfer fluid is pumped through the system, picking up heat from the regenerator and increasing the fluid temperature. Excess heat is expelled to the hot (right) heat exchanger, and the temperature of the regenerator decreases back down to its original value.

The next step of the AMR cycle is the adiabatic demagnetization process. The magnetic field is now removed from the regenerator causing its temperature to decrease

now as a result of the magnetocaloric effect. Just as in the magnetization process the fluid remains static, but now residing in the hot heat exchanger. The fluid temperature once more remains constant during this process.

The cold blow process is the final step in the AMR cycle. Now, the temperature of the cold end of the regenerator is less than that of the cold heat exchanger. The heat transfer fluid is then pumped through the system, picking up heat from the load and transferring it to the regenerator in order to raise its temperature. Once the temperature of the heat transfer reaches that of the cold heat exchanger the cycle then repeats itself.

There are four popular AMR cooling system designs that are implemented in physical prototypes. These designs involve either the regenerator or magnetization system moving in a linear fashion, as is the case for reciprocating designs, or these components moving in a rotational fashion, as is the case for rotary designs. While there are no substantial benefits or drawbacks in either system design, rotary-type AMR systems usually require a more complex valve system and timing in order to flow the heat transfer fluid through the regenerator.

A rotary-type AMR magnetic cooling system has been developed in 2014 by Arnold et al at the University of Victoria [8]. A 3D rendering and image of this physical prototype can be seen in *Fig. 10*. In this prototype a spherical particle packed regenerator bed containing gadolinium as the MCM and an 80-20 water-glycol heat transfer fluid is used. The total mass of magnetocaloric material contained within the regenerator is 0.650 kg and the mean particle diameter is 500 μm with a porosity of 0.38 (38% void volume). This prototype utilizes a nested Halbach cylinder magnetization system consisting of three concentric cylinders, with 12 permanent magnet segments in each cylinder.

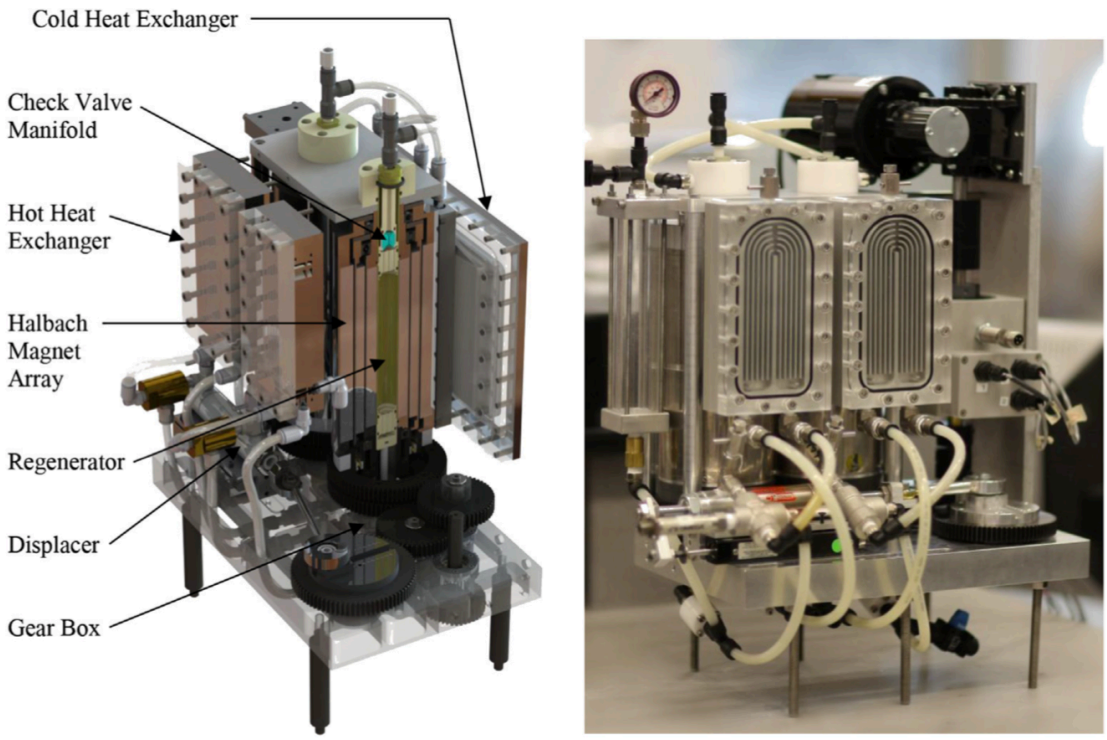

Figure 10: Rotary AMR developed by the University of Victoria [8].

The maximum obtainable magnetic field from this design is approximately 1.54 T. In this AMR design, magnetization and demagnetization is carried out by rotating the Halbach cylinder about a stationary regenerator bed. This device was tested at low frequencies of 0.5 Hz and 0.8 Hz.

Another recent AMR prototype has been developed in 2014 by Legait et al [9] of the reciprocating type. A rendering of this AMR system is presented in *Fig. 11*. The main goal of this study was to investigate the performance of parallel plate regenerator geometries using three different magnetocaloric materials. The three materials used as a regenerator material in this study are $Pr_{0.65}Sr_{0.35}MnO_3$ (1 mm thick plates, 1 mm gaps), $La(FeCo)_{13-x}Si_x$ (1 mm thick plates, 1 mm gaps), and gadolinium (1 mm thick plates, 0.3 mm gaps). A Halbach cylinder magnetization is utilized in this AMR prototype and produces a maximum magnetic field strength of 0.8 T.

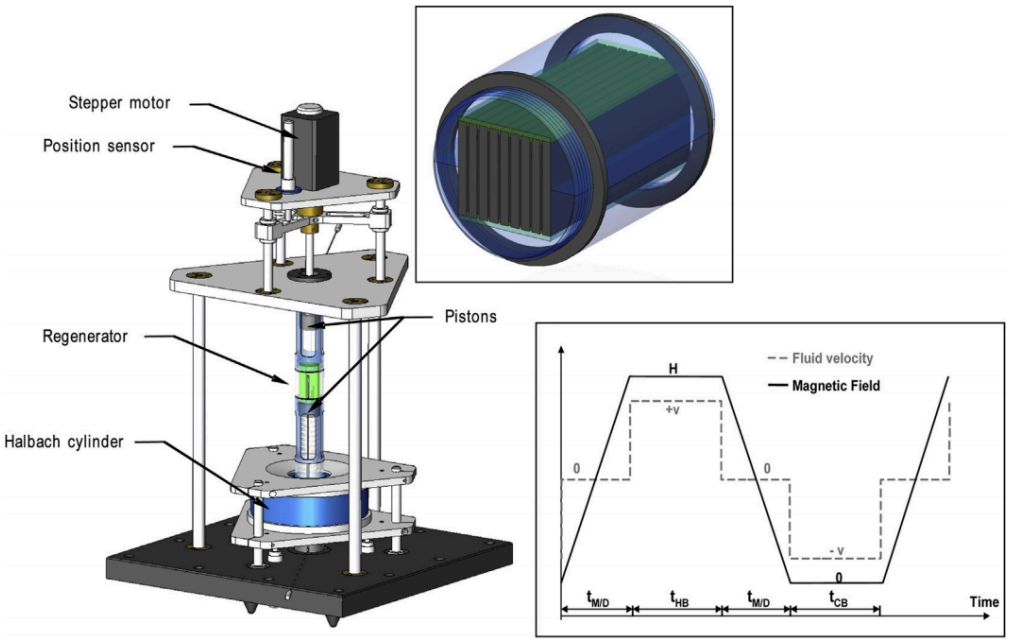

Figure 11: Model of the linear-type AMR developed by Legait et al [9].

In the linear AMR design, the magnetization system remains stationary while the regenerator bed is reciprocated back and forth to achieve magnetization and demagnetization of the MCM. This device was tested over a range of frequencies between 0.1 Hz and 1.43 Hz.

An extensive study of AMR devices has been performed by Gimaev et al [2] in an effort to assess the current state of magnetic cooling technology. *Tab. 1* lists some of the reviewed AMR devices along with the relevant regenerator and operational parameters.

From the data collected regarding the AMR prototypes, some conclusions may be drawn about regenerator geometries, maximum magnetic field strength, choice of heat transfer fluid, and operational parameters. AMR cooling systems with a packed bed regenerator appear to use spherical particles with average particle diameters ranging from 200-800 µm. Regenerators composed of parallel plates have average plate thicknesses of 1 mm.

Table 1: Data of AMR prototypes and corresponding operational parameters.

AMR Type	Regenerator Geometry	MCM (Particle/Plate Size)	Magnetic Field Strength [T]	Heat Transfer Fluid	Operating Frequency [Hz]	Reference
Linear	Packed Bed	Gd (600 μm)	1	Water	0.35	[10]
Linear	Parallel Plate	Gd (0.8 mm)	1.55	50-50 water-ethanol	≤ 0.25	[11]
Linear	Parallel Plate	$Pr_{0.65}Sr_{0.35}MnO_3$ (1 mm), $La(FeCo)_{13-x}Si_x$ (1 mm), Gd (1 mm)	0.8	-	0.1-1.43	[9]
Linear	Parallel Plate	Gd (1 mm)	1.45	Silicon oil	0.5	[12]
Linear	Packed Bed	Gd (200-500 μm)	1	Ethylene glycol	0.025	[13]
Rotary	Packed Bed	Layered LaFeSiH (177-246 μm)	1.44	Water-antifreeze	4	[3]
Rotary	Parallel Plate	Gd (0.3 mm)	0.98	Water	0.25-4	[14]
Rotary	Parallel Plate, Packed Bed (spheres)	Gd (0.5 mm), Gd (550-800 μm)	1.4	pH 8 Alkaline solution	0.5-1.25	[15]
Rotary	Packed Bed	Layered $Gd_{0.92}Y_{0.08}$, $Gd_{0.84}Dy_{0.16}$, $Gd_{0.87}Dy_{0.13}$, $Gd_{0.89}Dy_{0.11}$ (600 μm)	0.77	Water	3.33	[16]
Rotary	Parallel Plate	Gd (1 mm)	1.5	Helium gas	1.5	[17]

All reviewed cooling systems use some type of permanent magnetic Halbach array, with most achieving a maximum field strength of approximately 1.5 T. Water is prevalently used as the main heat transfer fluid, with some prototypes using a mixture of water with an anticorrosive agent. Mixtures like these are often used for regenerators containing gadolinium as they prevent the inherent corrosion that occurs over many operative cycles [18]. AMR cooling systems operate at very low frequencies, ranging from 0.025-4 Hz, with linear-type AMRs tending to operate at the low end of this range. This leads to the conclusion that operational frequency depends heavily on the type of AMR system, with rotary-type AMRs capable of attaining higher working frequencies.

3.3 MAGNETOCALORIC MATERIALS

Perhaps the most important component of a magnetic cooling system is the choice of magnetocaloric material. There has been much research done in recent years to develop new materials as well as efforts to improve upon the properties of existing magnetocaloric materials through alloying and other means. Since magnetic cooling systems can be used in a wide variety of applications, each with their own operative temperature range, selection of a material with favorable properties within this range is vital. When selecting a magnetocaloric material for use in a MCS the important quantities to consider are the adiabatic temperature change, the Curie temperature, and the order of magnetic transition that occurs at the Curie temperature.

Before discussing the properties of some of the more common magnetocaloric materials, it is important to first understand the characteristics of different magnetic transition orders. There are two families of materials in regard to the magnetic phase change that occurs at the Curie temperature: first-order magnetic transition (FOMT) and second-order magnetic transition (SOMT) materials. In general, FOMT materials display larger peaks in the adiabatic temperature change and magnetic entropy change but suffer from many more operational issues than SOMT materials. Gadolinium and many of its simple alloys are SOMT materials, while materials such as Heusler alloys are of the FOMT family.

FOMT materials experience a crystalline structure change that coincides with magnetic dipole ordering. Due to the atomic motion associated with the crystalline structure change, the MCE takes more considerable time to develop in these materials, typically on the order of seconds. The time it takes for the MCE to fully develop can

decrease the performance of a magnetic cooling system anywhere from 30-50% [19]. The structural transformation also poses the issue of material deterioration over many operating cycles, lessening its desirability for long-term cooling applications. Also, of note, these materials will display magnetic and thermal hysteresis. The degree of hysteresis varies from material to material, and this effect can be lessened through slight changes in alloy composition.

SOMT materials align their magnetic dipoles in the presence of a magnetic field at the Curie temperature, and do not undergo a crystalline structure change. The magnetocaloric effect is near instantaneous, typically on the order of microseconds, and these materials do not suffer from deterioration over the course of many operative cycles since no lattice change occurs. These materials also do not display any magnetic or thermal hysteresis.

Gadolinium is by far the most extensively studied and characterized magnetocaloric material and is one of few materials that has a strong enough MCE in its pure elemental form to be used in magnetic cooling systems. Gadolinium has a Curie temperature close to room temperature, at approximately 293 K, and for this reason it is often utilized for cooling in room temperature environments. The adiabatic temperature change and, by extension, the magnetic entropy change of gadolinium peak at moderate values and cover a wide range around room temperature.

The experimental measurements presented by Dan'kov et al [20] in *Fig. 12* give a visual representation of the magnetocaloric effect that exists in gadolinium. Both the adiabatic temperature change and the change in magnetic entropy increase and widen under the application of stronger magnetic fields.

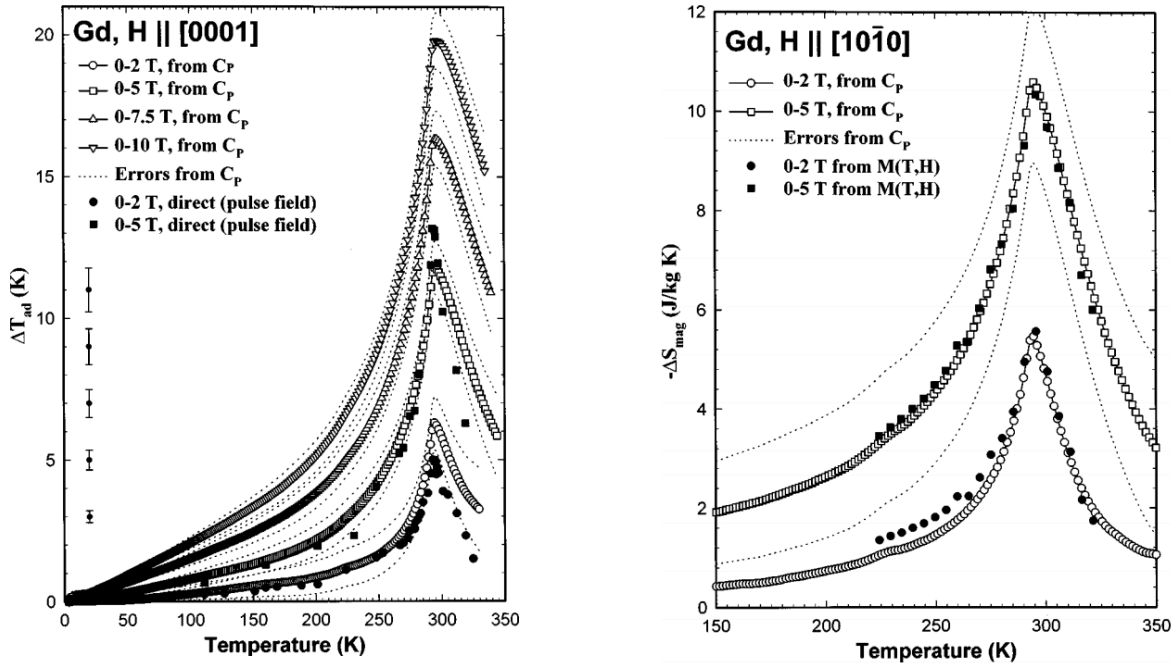

Figure 12: Experimental measurements of the MCE for gadolinium [20].

These quantities also exhibit a strong non-linearity around the Curie temperature of 293 K; this behavior can be observed around any MCM's Curie temperature. Figures of the adiabatic temperature change and magnetic entropy change are useful tools when determining the optimal material for a specific operating temperature range.

The magnetothermal properties of gadolinium can also be modified through alloying with other materials to tune the location of the Curie temperature. According to the research done by Engelbrecht et al [19], alloying gadolinium with elements in the lanthanide series such as terbium, dysprosium, or erbium will lower the Curie temperature. In order to raise the Curie temperature, gadolinium can be alloyed with palladium to form Gd_7Pd_3. All of these gadolinium alloys display a similar magnetocaloric effect to that of pure gadolinium, in addition to remaining SOMT materials, and are often utilized in regenerator bed layering to achieve a maximum MCE at different locations along the regenerator. The main drawback of gadolinium and its

alloys lie in the higher cost of rare earth metals when compared to other magnetocaloric materials.

Some FOMT materials that have been thoroughly researched in recent years are $Gd_5(SiGe)_4$, La(FeSi), $MnFeP_{1-x}As_x$, and $Ni_{2+x}Mn_{1-x}Ga$ alloys. Although FOMT materials run into more operational issues, such as deterioration or magnetic and thermal hysteresis, the large MCE that accompanies this family of MCM's is attractive. The increased MCE observed in these materials is due to a crystalline structure change coinciding with a magnetic structure change at the same temperature. By changing the stoichiometry of these alloys, the transition temperature can be tuned. Considering the Heusler alloy of stoichiometric Ni_2MnGa, which usually has a magnetic transition at a temperature of 376 K and a structural transition at 220 K, the nickel and manganese composition can be altered in order to make these two temperatures coincide.

According to the work of Stadler et al [21], it has also been found that altering the composition of $Ni_{2+x}Mn_{1-x}Ga$ alloys through atomic substitution with In, Fe, Co, or Cu also shifts the location of the two transformation temperatures. In the case of Ni-Mn-Ga Heusler alloys, the structure change that occurs on heating of the material is a martensite-austenite transformation that occurs at T_M. Substitution of In in these alloys lowered both the magnetic and structural transition temperatures with increasing In concentration, while substitution of Fe increased the magnetic transition temperature and lowered that of the structural transition. Of greater interest are the results from substitution with Co or Cu, which lowers the magnetic transition temperature while increasing the structural transition temperature allowing the two temperatures to coincide. Using increasing

concentrations of Cu according to the formula $Ni_2Mn_{1-x}Cu_xGa$ the peak magnetic entropy change occurs at higher temperatures, as seen in *Fig. 13*.

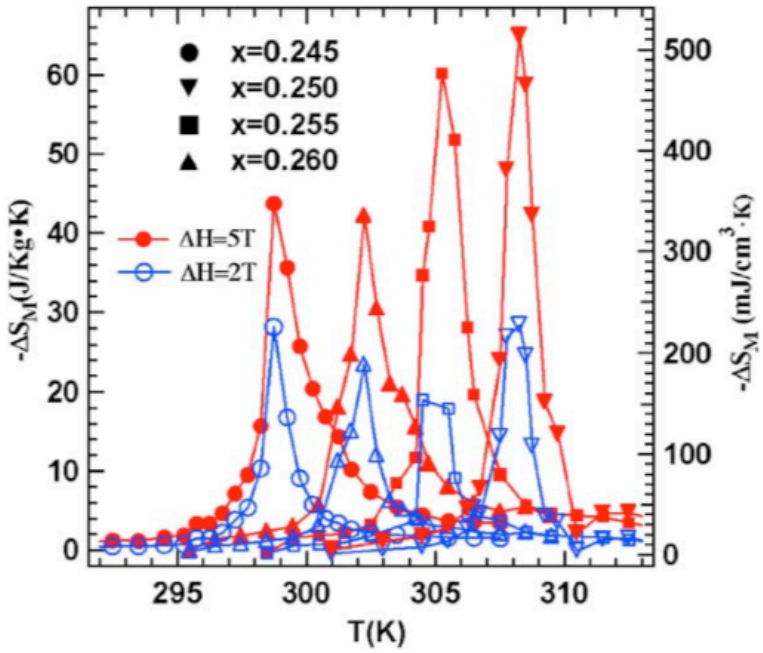

Figure 13: $-\Delta S_M$ as a function of temperature for various Cu concentrations [21].

Aside from altering the concentration MCM alloys, a processing technique known as stress-assisted thermal cycling (SATC) has also shown promise in improving upon magnetothermal properties in shape-memory alloys. In the work of McLeod et al [22], stress-assisted thermal cycling of polycrystalline Ni-Mn-Ga Heusler alloys showed large MCE increases as large as 84%. SATC is performed by thermally cycling an alloy through its martensite-austenite transformation temperature under a constant mechanical load in order to gain a preferred orientation of the easy magnetization axis. When a magnetic field is then applied along the easy magnetization axis, the material is trained to more readily transform between austenite to martensite upon cooling.

The main material of interest for this study is a $Ni_{0.50}Mn_{0.19}Cu_{0.06}Ga_{0.25}$ alloy that has undergone SATC. An example of the change in magnetic entropy before (AR) and

after SATC taken from experimental measurements during magnetization is presented in *Fig. 14*.

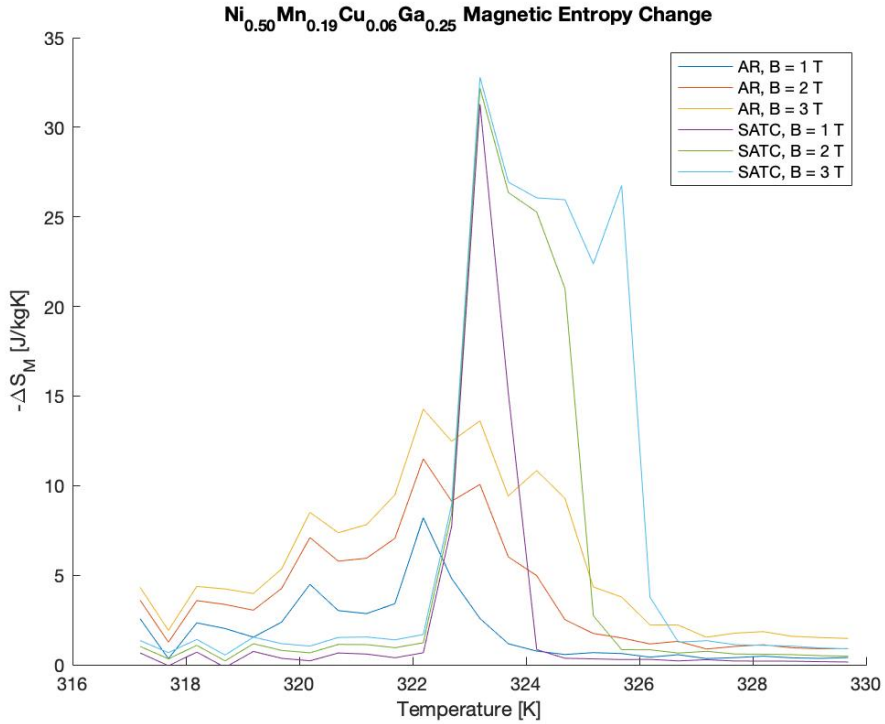

Figure 14: Comparison of $-\Delta S_M$ before and after SATC during magnetization.

There is a significant increase in magnetic entropy change that is observed in the alloy after SATC. While the magnitude of the magnetic entropy change increases after the SATC processing, the width of these curves decreases.

IV. MODELING AND SIMULATION

In this section the foundation of the mean-field model and the dynamic 1D AMR simulation are presented. Dynamic AMR simulations are frequently used as a means to test various operational parameters and the performance of different magnetocaloric materials. Dynamic models are beneficial because they are time-dependent, allowing for the temperature evolution of the regenerator bed to be examined. They rely on the solutions of coupled differential equations describing the regenerator bed and heat transfer fluid temperature profiles. While these types of models can be made to accurately describe the nature of functioning AMR devices, they have large computational costs and can take a large amount of time to complete the calculations when using a standard computer. Both the mean-field model and AMR simulator are implemented in Matlab and will both be described in detail in *Sec. 4.1* and *Sec. 4.2*, respectively . The full code for the mean-field model and AMR simulator are presented in *App. A* and *App. B* as well.

4.1 MEAN-FIELD MODEL OF FERROMAGNETIC MATERIALS

The mean-field model (or molecular field theory) is often utilized in conjunction with AMR simulations in order to provide thermodynamically accurate material data such as magnetization, heat capacity, magnetic entropy change, and adiabatic temperature change for various magnetic field strengths. One of the main reasons this method is employed is due to the scarcity of magnetocaloric material data available for specific compositions and field strengths. The mean-field model has the limitation of only being applicable to SOMT materials, as this family of materials can safely assume a separation of its three total entropy contributions: lattice entropy (S_{lat}), magnetic entropy (S_{mag}), and electronic entropy (S_{el}). The foundation of the mean-field theory, as applied to ferromagnetic MCMs, is described in great detail in Tishin's book *The Magnetocaloric Effect and its Applications* from pages 10-28 [5]. A slightly more succinct explanation of the model is presented in this section.

Using a statistical mechanics approach, the statistical sum for a system can be described by:

$$Z = \sum_n e^{-E_n/k_B T} = Spe^{-\mathcal{H}/k_B T} \tag{5}$$

where $\mathcal{H}$ is the Hamiltonian of the magnetic system, E_n are its eigenvalues, k_B is the Boltzmann constant, and T is the temperature. The Hamiltonian for an isotropic ferromagnetic system takes on the following form:

$$\mathcal{H} = -\sum_{i>j} I_{ij}\left(J_i J_j\right) - \sum_i g_J \mu_B J_i B \tag{6}$$

In *Eq. (6)*, I_{ij} represents the exchange integral for the interaction between i and j ions in the system, J is the total angular momentum, g_J is the Landé factor, μ_B is the Bohr magneton, and B is the amplitude of applied magnetic field.

The free energy is a function of temperature, volume, and magnetic field strength. The equation for the free energy, as well as its differential form, are given by:

$$F = U - TS \tag{7}$$

$$dF = -SdT - pdV - MdB \tag{8}$$

By knowing the expression for the statistical sum Z, the free energy of the system can be calculated using the following expression:

$$F = -k_B T \ln(Z) \tag{9}$$

and the internal system parameters of entropy, pressure, and magnetization can be determined through conjugating the external parameters of temperature, volume, and magnetic field strength using the following three equations of state:

$$S(T,V,B) = -\left(\frac{\partial F}{\partial T}\right)_{V,B} \tag{10}$$

$$p(T,V,B) = -\left(\frac{\partial F}{\partial V}\right)_{T,B} \tag{11}$$

$$M(T,V,B) = -\left(\frac{\partial F}{\partial B}\right)_{T,V} \tag{12}$$

Looking at the case of a single atom, the partition function takes on the form:

$$Z_J(X) = \sum_{m=-J}^{J} e^{mX/J} \tag{13}$$

where X is defined as:

$$X = \frac{g_J \mu_B J B}{k_B T} \tag{14}$$

A summation of *Eq. (13)* yields:

$$Z_J(x) = \sinh\left(\frac{2J+1}{2J} X\right) / \sinh\left(\frac{1}{2J} X\right) \tag{15}$$

which can then be plugged into an expression for the magnetic part of the free energy:

$$F_M = -k_B T \ln\left(Z_J(X)\right)^N \tag{16}$$

where N is the number of magnetic atoms in the system. Using *Eq. (16)* for the magnetic free energy, and applying *Eq. (12)*, an expression for the magnetization can be determined:

$$M(X) = N_{Av} g_J \mu_B J B_J(X) \tag{17}$$

where B_J is the Brillouin function of the form:

$$B_J(X) = \frac{2J+1}{2J} \coth\left(\frac{2J+1}{2J} X\right) - \frac{1}{2J} \coth\left(\frac{1}{2J} X\right) \tag{18}$$

In the mean-field model, the exchange integral in *Eq. (6)* is replaced with an effective exchange field that is given by:

$$B_m = \lambda M \tag{19}$$

where λ is the Weiss molecular field coefficient. By adding this molecular field to the externally applied magnetic field in *Eq. (14)*, it then becomes:

$$X = \frac{g_J \mu_B J (B + \lambda M)}{k_B T} \tag{20}$$

with the equation for the Weiss molecular field coefficient being defined as:

$$\lambda = \frac{3 k_B T_C}{N_{Av} g_J^2 \mu_B^2 J(J+1)} \tag{21}$$

We now arrive at the final pieces of the mean-field model, which are the equations that describe the three components of the total entropy. For completeness in this section, the total entropy equation will be provided again:

$$S(T, B) = S_{lat}(T, B) + S_{mag}(T, B) + S_{el}(T, B) \tag{22}$$

It is worth reinforcing that this equation is only correct for second order magnetic transition materials, such as the magnetic rare earth metals. As can be seen in *Eq. (22)*, all three contributions depend on both temperature as well as magnetic field. However, in the approximation provided by the mean-field model, it can be assumed that the lattice

and electronic contributions depend only on the temperature and all magnetic field dependence is carried only by the magnetic contribution of entropy. The expressions for the lattice, magnetic, and electronic contributions are given, respectively, by:

$$S_{lat} = R\left[-3\ln\left(1 - e^{T_D/T}\right) + 12\left(\frac{T}{T_D}\right)^3 \int_0^{T_D/T} \frac{y^3}{e^y - 1} dy\right] \tag{23}$$

$$S_{mag} = R\left[\ln\left(\frac{\sinh\left(\frac{2J+1}{2J}X\right)}{\sinh\left(\frac{1}{2J}X\right)}\right) - XB_J(X)\right] \tag{24}$$

$$S_{el} = \gamma_{el} T \tag{25}$$

where R is the universal gas constant, T_D is the Debye temperature, y is an integration variable (whose variable assignment holds no significance), and γ_{el} is the electronic heat capacity coefficient.

The main quantities of interest that result from the mean-field model are magnetization, magnetic entropy, change in magnetic entropy, heat capacity, and adiabatic temperature change for varying magnetic fields. In order to obtain all of these quantities, an issue pertaining to the magnetization must first be solved. The equation for the magnetization (*Eq. (17)*) in its current state is self-consistent, since a term for magnetization appears within the Brillouin function argument X. The graphical method of Weiss is one of the simplest ways to get around this problem, and is what is used in this thesis, else some numerical method must be employed.

The graphical method of Weiss involves finding the intersection of two functions when plotted against the input argument of the Brillouin function. This intersection provides a self-consistent solution for the magnetization. In order to use this method, some manipulation of the equations containing the magnetization term is required. The

first manipulation involves *Eq. (18)*, and simply requires the division of the constants on the right-hand side of the equation:

$$\sigma = \frac{M(X)}{N_{Av} g_J \mu_B J} = B_J(X) \tag{26}$$

This equation describes a reduced magnetization, as denoted by σ, and will serve as the first function for Weiss' method. Upon inspection it is clearly seen that this is nothing more than the Brillouin function already defined above.

The second function originates at *Eq. (20)*, with the first step being the isolation of the molecular field term:

$$\frac{k_B T}{g_J \mu_B J} X - B = \lambda M \tag{27}$$

Now a substitution can be made, using *Eq. (26)*, to get rid of the magnetization term and replace it with the reduced magnetization:

$$\frac{k_B T}{g_J \mu_B J} X - B = \lambda N_{Av} g_J \mu_B J \sigma \tag{28}$$

The final step for creating the second function is to isolate the reduced magnetization term, which yields the following equation:

$$\sigma = \frac{k_B T}{\lambda N_{Av} (g_J \mu_B J)^2} X - \frac{B}{\lambda N_{Av} g_J \mu_B J} \tag{29}$$

The form of this equation reveals that it is linear, with the slope of the line holding the temperature dependence and the y-intercept holding the field dependence. Now that two functions of reduced magnetization have been created, they can be plotted against the Brillouin input argument and their intersection can be determined.

An example of the graphical method of Weiss can be seen in *Fig. 15*. The intersection of these two curves gives a self-consistent solution for the reduced magnetization at a given temperature.

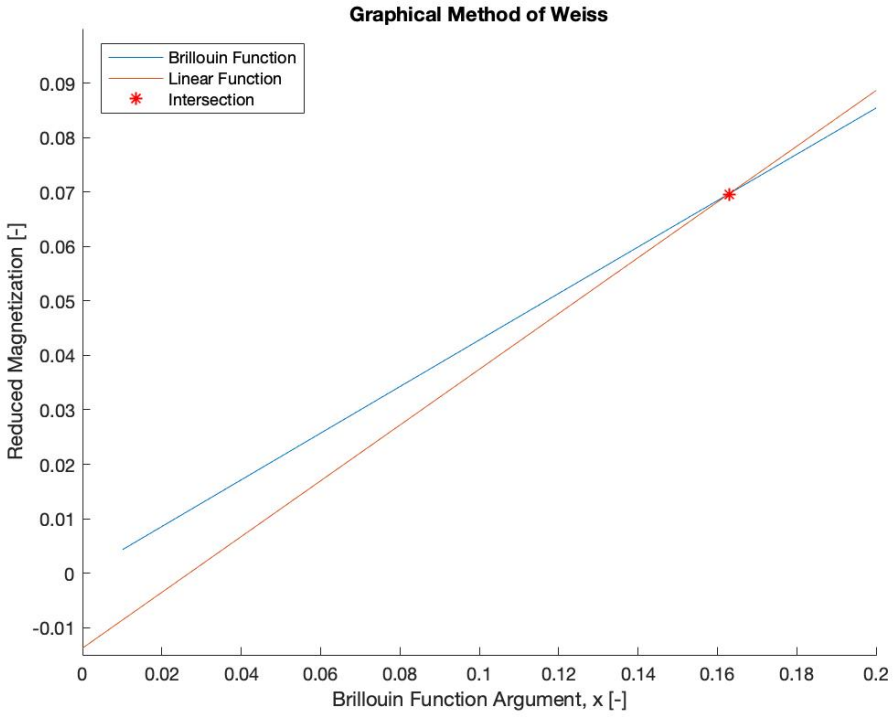

Figure 15: Graphical method of Weiss.

In order to retrieve the actual value of the magnetization for a range of temperatures and magnetic field strengths, the value of X must be plugged back into the Brillouin function and then *Eq. (17)* can be utilized.

The mean-field model is implemented in Matlab and begins with the inputs of general physical constants such as the universal gas constant, Avogadro's constant, Boltzmann's constant, and the Bohr magneton. Next, material specific inputs are required including the Landé factor, total angular momentum quantum number, Curie temperature, Debye temperature, molar mass, and the electronic heat capacity coefficient (if one chooses to include this contribution). The desired magnetic field strength and range of temperature is then input and a "for" loop is executed to sweep through these

temperatures and determine the value of the intersection of the two reduced magnetization functions at each temperature.

In order to determine the value of the intersection point the “fzero” function is utilized. This function finds the zero point of the subtraction of the two reduced magnetization functions, and hence where the two functions are equal. The “fzero” function requires a guess value to give a location for the function to start looking for the zero point. Since the guess value requires updated values depending on the applied magnetic field strength and current temperature, a routine is developed to change the guess value as the program sweeps through temperatures. It should be noted that the guess value does not need to be exact and can hold the same value for a large range of temperatures. However, this section of the program may require updated guess values when different material properties are input into the system in order to obtain physically meaningful magnetization results.

Once the values of the intersection points are found for all desired temperatures the magnetization, change in total entropy, and change in magnetic entropy may be immediately computed. In order to determine the change in total entropy, the “diff” function is utilized to numerically approximate the value of the derivative. To compute the change in magnetic entropy, magnetic entropy data for zero applied field must already be computed since the equation for this quantity involves the change in the magnetic contribution to entropy between a nonzero field value and zero field. The heat capacity may be computed after the change in total entropy is obtained, according to the following equation:

$$c_p = T\left(\frac{\partial S_{Tot}}{\partial T}\right)_B \tag{30}$$

Lastly, the adiabatic temperature change of the material is computed once values for both the heat capacity and change in magnetic entropy have been obtained.

In order to verify the mean-field model the results from this simulation will be compared with those of Bouchekara and Nahas [23]. From this work, the magnetothermal properties of gadolinium are computed using the mean-field model. A list of the required input properties for gadolinium are shown in *Tab. 2*. The value of the electronic heat capacity coefficient for gadolinium is obtained from the work of Brown [1].

Table 2: Gadolinium input parameters for the mean-field model.

Material	g_J	J **[N•m•s]**	T_C **[K]**	T_D **[K]**	γ_{el} **[J/mol•K^2]**	MM **[kg/mol]**
Gadolinium	2	3.5	293	184	0.0108784	0.157

In the work presented by Bouchekara and Nahas the electronic contribution to the total entropy is ignored, so for the sake of this comparison it will also be ignored for now. The plots of the magnetization, as well as the heat capacity, for gadolinium as determined by Bouchekara and Nahas are presented in *Fig. 16*. In *Fig. 17*, the results of the magnetization and heat capacity provided by the model developed in this thesis are presented. An acceptable agreement can be seen between the two models, thus ensuring that the developed mean-field model works as intended. The remaining quantities obtained from the mean-field model, including the electronic contribution to the total entropy, will be presented in the *Results* section of this thesis.

One final important remark about the mean-field model pertains to the case of zero applied magnetic field. As can be seen in *Fig. 17*, the magnetization rapidly goes to zero when approaching the Curie temperature of the material in the absence of an externally applied magnetic field. Below the Curie temperature, SOMT materials are ferromagnetic and experience a spontaneous magnetization.

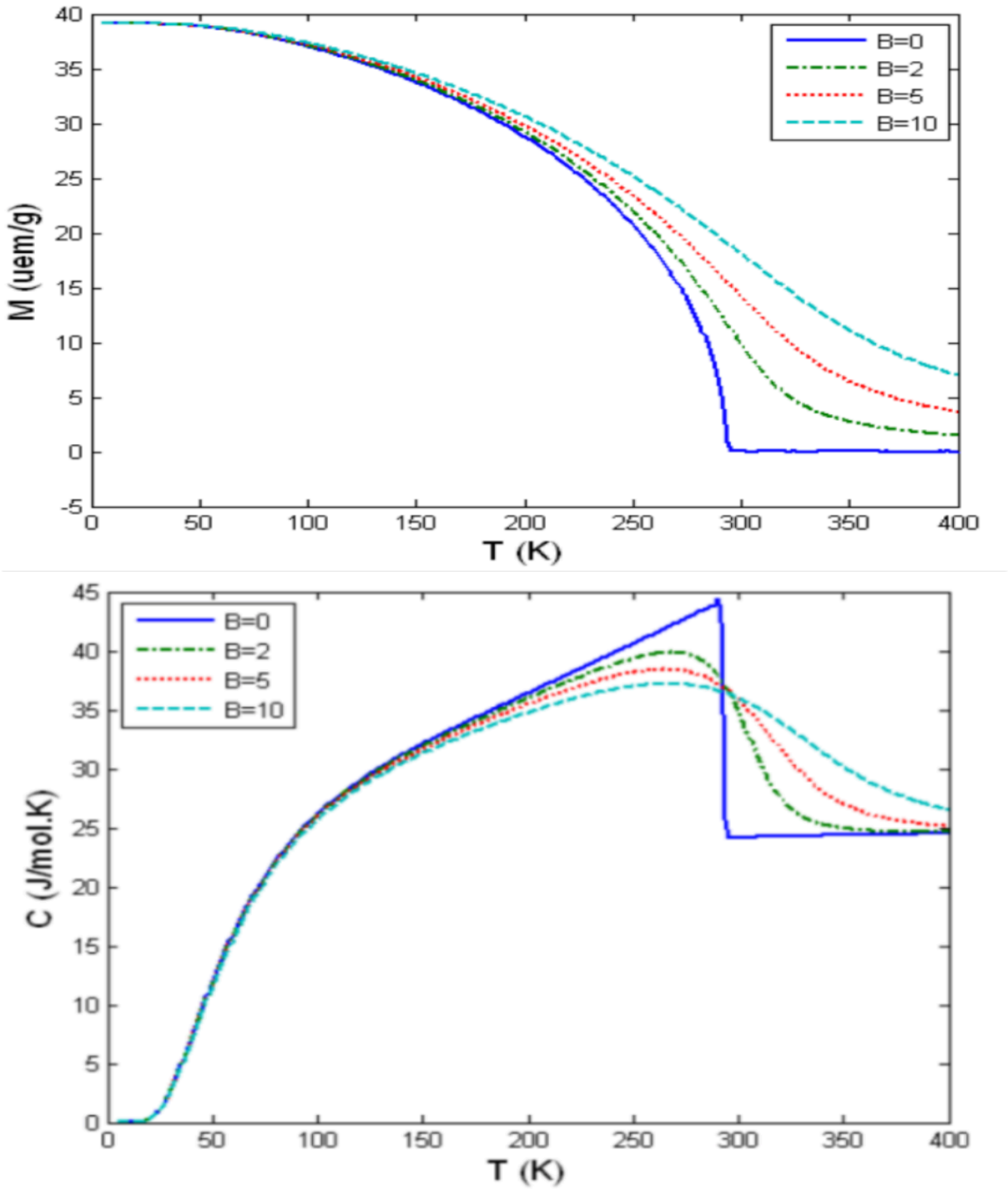

Figure 16: Magnetization and heat capacity curves for gadolinium as determined by Bouchekara and Nahas [23] (w/out electronic contribution to total entropy).

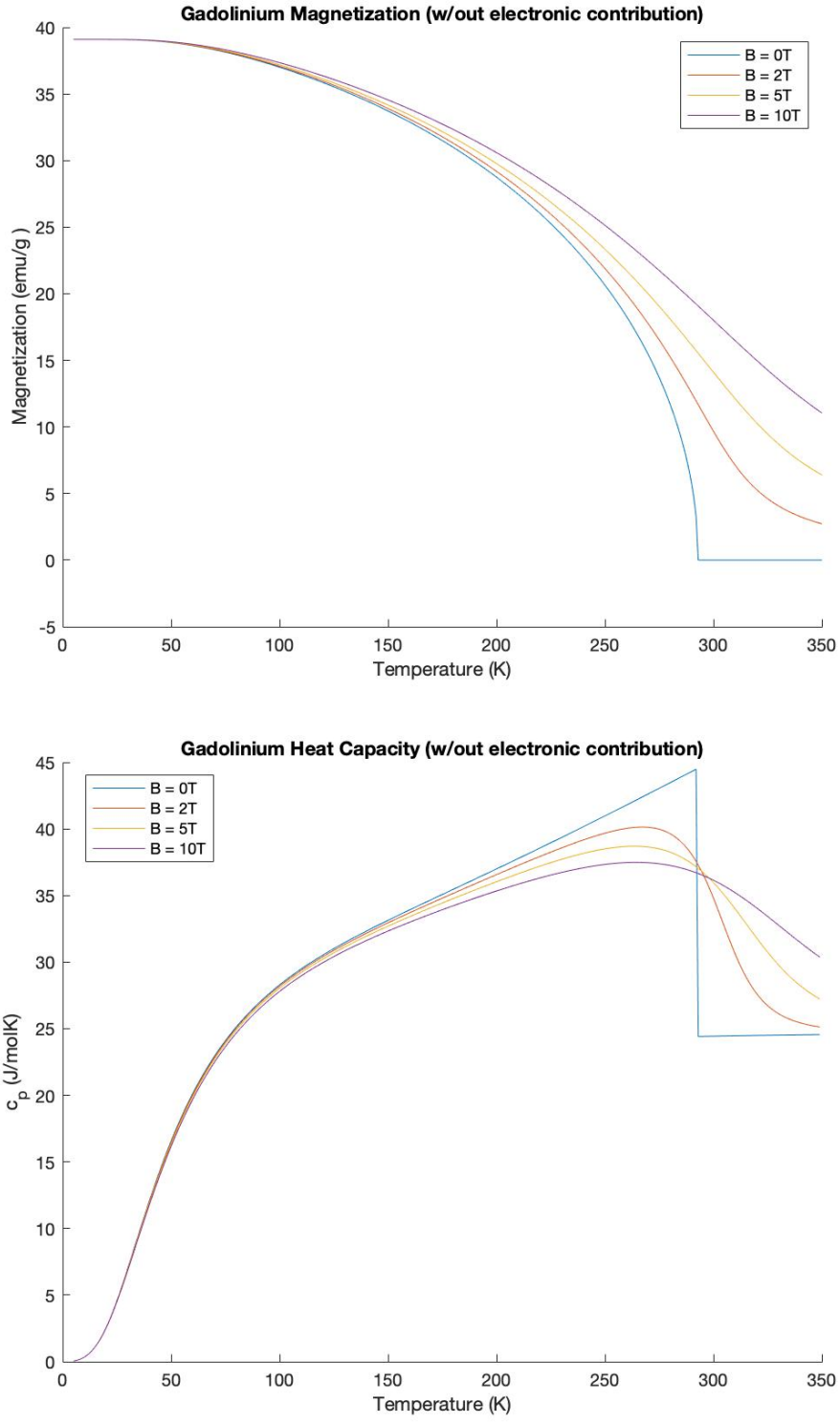

Figure 17: Magnetization and heat capacity curves for gadolinium from the MFM developed in this thesis (w/out electronic contribution to total entropy).

However, when above the Curie temperature, the materials become paramagnetic and do not retain any magnetization without the aid of an applied field.

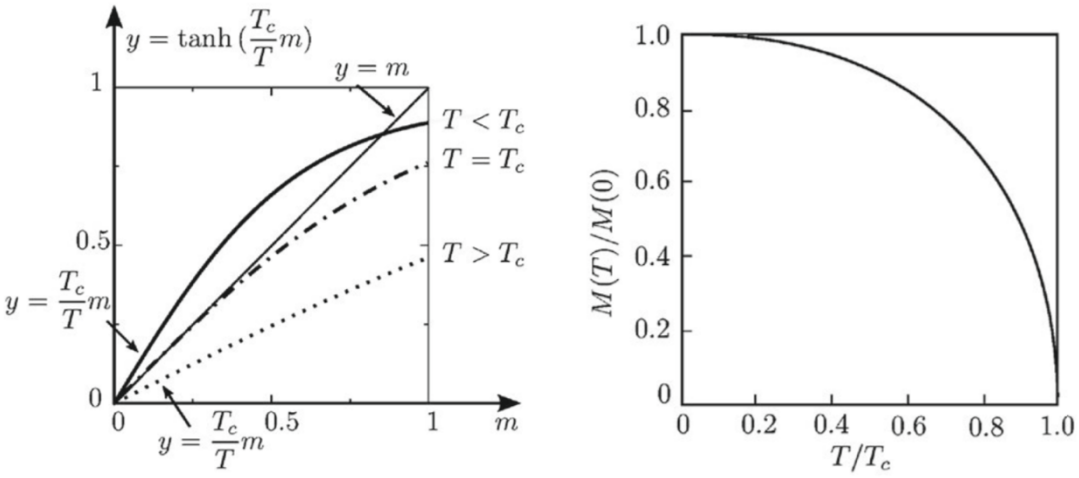

Figure 18: Reduced magnetization curves for various temperature regimes [24].

With the aid of the *Fig. 18* it is clearly visible that for temperatures below the Curie point there is a non-trivial solution for the magnetization, but for temperatures greater than or equal to the Curie point there is only the trivial solution. In order to account for this, in the current development of the mean-field model, a routine is implemented for the case of zero applied field that sets the slope term of *Eq. (29)* to zero when temperatures exceed that of the Curie temperature.

4.2 1D ACTIVE MAGNETIC REGENERATOR MODELING

The purpose of the AMR simulation developed for this thesis is to have the ability to test the performance of various magnetocaloric materials without the need to build a physical prototype. The program is capable of numerically modeling the four main processes of the AMR cycle: magnetization, warm blow, demagnetization, and cold blow. A spherical particle packed bed regenerator geometry will be considered in this simulation, as it appears to be the most abundantly used geometry in other simulations and will provide a basis for comparison among other models, namely the model created by Borbolla [4].

The five basic components of an AMR system are modeled either explicitly or implicitly. The regenerator bed is the only explicitly modeled component while the magnetization system, heat exchangers, and pump are all modeled implicitly. The effects of these components can be seen through boundary conditions or other parameters in the simulation. In order to simplify the modeling and reduce computation time, the following assumptions are made:

1. The regenerator bed is perfectly insulated; no heat transfer occurs between the regenerator and the environment.
2. The surface area of the regenerator is distributed evenly throughout its volume; the porosity of the regenerator bed is the same at any point.
3. There is negligible axial conduction at the ends of the regenerator bed.
4. The magnetization and demagnetization processes are isentropic and instantaneous.

5. The physical properties of the heat transfer fluid are constant in both time and temperature.

6. The velocity of the heat transfer fluid is constant, and flow is laminar for the duration of a blow process.

7. The heat exchangers have a high efficiency such that fluid temperature is constant when exiting a heat exchanger and equal to the temperature of the heat exchanger.

The modeling of the two blow processes is achieved from the solution of two coupled partial differential equations. The first PDE describes the temperature profile of the MCM contained within the regenerator bed and the second describes the temperature profile of the heat transfer fluid flowing through the regenerator. Both equations describe the temperature profile evolution in time and in a single spatial dimension. The governing equation for the solid regenerator bed is given by:

$$\frac{\partial T_s(x,t)}{\partial t} = \frac{1}{\rho_s c_s(T_s,H)}\left[\frac{h a_s}{(1-\varepsilon)}\left(T_f(x,t) - T_s(x,t)\right) + k_{eff,s}\left(\frac{\partial^2 T_s(x,t)}{\partial x^2}\right)\right] \quad (31)$$

The term on left-hand side of the equation describes the variation of the solid (MCM) temperature with time. The first term within the brackets on the right-hand side of the equation describes the convective heat transfer between the fluid and solid and the second term describes the heat flux due to axial conduction.

The governing equation for the heat transfer fluid is given by:

$$\frac{\partial T_f(x,t)}{\partial t} = \frac{1}{\rho_f c_f}\left[\frac{h a_s}{\varepsilon}\left(T_s(x,t) - T_f(x,t)\right) + k_{eff,f}\left(\frac{\partial^2 T_f(x,t)}{\partial x^2}\right) - \frac{\dot{m}_f c_f}{\varepsilon A_c}\left(\frac{\partial T_f(x,t)}{\partial x}\right)\right] \quad (32)$$

The left-hand side of the equation is the variation of the fluid temperature with time. On the right-hand side of the equation the first term within brackets represents the convective heat transfer between the solid and fluid, the second term describes the heat flow due to axial dispersion, and the third term is the change in enthalpy of the fluid.

The governing equations for the solid and fluid both contain a convective heat transfer term that links the two PDEs, and thus the solid and fluid temperatures, together. Within this term is the convective heat transfer coefficient, h, which depends on the effective thermal conductivity of the fluid and hydraulic diameter of the regenerator bed according to the following equation:

$$h = \frac{k_{eff,f} Nu}{d_h} \tag{33}$$

where Nu is the Nusselt number. This form of the convective heat transfer coefficient is based on the empirical correlation developed by Wakao et al [25] and is quite frequently expressed in this general form in other AMR simulations.

The Nusselt number is a dimensionless parameter that pertains to convective heat transfer. This parameter is defined as the ratio between the heat transfer done by convection to the heat transfer done by conduction and is often expressed as a function of the Reynolds number (Re) and the Prandtl number (Pr). The correlation that is used for this simulation is derived from the work of Frischmann et al [26] where a correlation was developed specifically for spherical particle packed beds of magnetocaloric material. This Nusselt number correlation is given by:

$$Nu = 0.70 Re^{0.60} Pr^{0.23} \tag{34}$$

Another quantity that need be defined in order to calculate the convective heat transfer coefficient is the effective thermal conductivity. In the work done by Feng et al [27] a generalized model is developed for the effective thermal conductivity of porous media. The interpretation of this model, as performed by Aprea et al [6], is how the effective thermal conductivities for the solid and fluid will be defined. The effective conductivity for the solid phase is:

$$k_{eff,s} = (1-\varepsilon)k_s \tag{35}$$

and for the fluid phase is:

$$k_{eff,f} = \varepsilon k_f + 0.5\left(PrRe\frac{d_p}{d_h}\right)k_f \tag{36}$$

where k_s and k_f are the thermal conductivities of the solid MCM and heat transfer fluid, respectively.

The final quantities to be defined for the solid and fluid governing equations are the volume specific surface area, a_s, and the cross-sectional area of the regenerator, A_c. The volume specific surface area depends on the geometry of the regenerator, porosity, and average particle diameter. For a spherical particle packed bed, the equation reads:

$$a_s = \frac{6(1-\varepsilon)}{d_p} \tag{37}$$

For different regenerator geometries, such as parallel plates or pin arrays, a different expression for the volume specific surface area must be employed. Assuming the volume of the regenerator to be a cylinder packed with magnetocaloric material, the expression for the cross-sectional area is:

$$A_c = \pi\left(\frac{d}{2}\right)^2 \tag{38}$$

where d is the diameter of the regenerator bed.

In order to fully simulate the four main AMR processes a number of equations and boundary conditions must be utilized. The following set of equations show the influence of the magnetization system, heat exchangers, and pumping system on the overall simulation. The magnetization system supplies the magnetic field required to adiabatically increase or decrease the temperature of the MCM contained within the regenerator bed. Its influence on the system is seen through altering the magnitude of the

adiabatic temperature change and heat capacity of the material, as well as defining the frequency of operation. The heat exchangers' influence is felt through the boundary conditions they impose during a blow period. The influence of the pumping system is to provide the mass flow rates and direction of fluid flow through the AMR.

The first process in the AMR cycle is the adiabatic magnetization of the regenerator. In this step the fluid is taken to be stationary in the cold heat exchanger and the magnetic field is at its maximum value, causing the temperature of the regenerator bed to increase adiabatically. This process can be described by the following magnetization equation:

$$T_s(x, 0^+) = T_s(x, 0^-) + \Delta T_{ad}^{mag}(T_s(x, 0^-), \Delta B) \tag{39}$$

The term on the left side of this equation describes the temperature of the MCM at a position along the regenerator just after magnetization has occurred. The first term on the right-hand side of the equation describes the temperature of the MCM just before magnetization and the second term describes the adiabatic temperature change resulting from exposure to an externally applied magnetic field.

After magnetization of the regenerator bed occurs, the warm blow process of the AMR cycle begins. The warm blow process runs from $t = 0$ to $t = t_c / 2$, where t_c is the total AMR cycle duration assuming the magnetization and demagnetization processes to be instantaneous. The fluid velocity is taken to be positive, flowing from left to right within the regenerator, and the fluid temperature at the left boundary is assumed to initially be the same value as the cold heat exchanger temperature. This step involves the simultaneous solving the two governing equations, for the solid and fluid, with the imposed warm blow boundary conditions set by the heat exchangers:

$$\left.\frac{\partial T_s}{\partial x}\right|_{0,t} = 0,\ \left.\frac{\partial T_s}{\partial x}\right|_{L,t} = 0,\ \left.\frac{\partial T_f}{\partial x}\right|_{L,t} = 0 \tag{40}$$

These boundary conditions state that the MCM temperature is not changing with position at either end of the regenerator, and that the fluid temperature is not changing with position at the hot (right) end of the regenerator; these are adiabatic surface boundary conditions.

Once a warm blow period has finished, the regenerator bed is demagnetized and the temperature of the MCM decreases adiabatically. Fluid flow is once again considered null, with the fluid residing in the hot heat exchanger. The equation for demagnetization during this step is:

$$T_s\left(x, \frac{t_c}{2}^+\right) = T_s\left(x, \frac{t_c}{2}^-\right) + \Delta T_{ad}^{demag}\left(T_s\left(x, \frac{t_c}{2}^-\right), -\Delta B\right) \tag{41}$$

The term to the left of the equals sign denotes the temperature of the MCM at a position along the regenerator just after demagnetization has occurred. On the right-hand side of the equation, the first term represents the MCM temperature just before demagnetization while the second term represents the adiabatic reduction in temperature resulting from removal of the applied magnetic field. It should be noted that there may be different values for the adiabatic temperature change depending on if the material is being magnetized or demagnetized. However, for SOMT materials such as gadolinium the two are the same.

The final step that occurs after demagnetization is the cold blow process. The cold blow runs from $t = t_c / 2$ to $t = t_c$, thus completing the AMR cycle. During this step the fluid velocity is taken to be negative, flowing from right to left within the regenerator, and the fluid temperature at the right boundary is initially assumed to be that of the hot

heat exchanger temperature. Once again, the solid and fluid governing equations are solved simultaneously, but with the cold blow boundary conditions imposed:

$$\left.\frac{\partial T_s}{\partial x}\right|_{0,t} = 0,\ \left.\frac{\partial T_s}{\partial x}\right|_{L,t} = 0,\ \left.\frac{\partial T_f}{\partial x}\right|_{0,t} = 0 \tag{42}$$

These boundary conditions state once more that the MCM temperature does not change at the regenerator ends, but now states that the fluid temperature is not changing at the cold (left) end.

Aside from the direction of fluid flow, as mentioned in the two blow periods, the pumping system also provides the mass flow rate for the system. It is necessary to express the mass flow rate as a normalized quantity so that the performance of AMR systems operating at different frequencies or different sizes may be directly compared. This quantity, known as the utilization factor, is expressed as:

$$\Phi = \frac{t_c \dot{m}_f c_f}{2 m_s \bar{c}_s} = \frac{\dot{m}_f c_f}{2 f m_s \bar{c}_s} \tag{43}$$

where $\dot{m}_f$ is the mass flow rate in units of kg/s and $\bar{c}_s$ is the maximum specific heat capacity of the MCM at zero magnetic field [28]. According to the work done by Tagliafico et al [29], a suitable range of values for the utilization factor lie between 0.5 and 3.5.

Also pertaining the pumping system is the input work required to operate the device, which will affect the overall AMR efficiency. In order to calculate the pumping work, the pressure drop of the fluid as it flows through the regenerator must be determined. A fluid experiences a pressure drop moving through a packed bed due to loss factors such as friction. The Ergun correlation is often employed to express the friction factor in porous media as a function of a modified Reynolds number and is useful in

determining the pressure drop of a regenerator. The pressure drop according to the Ergun correlation is:

$$\Delta p = \frac{L\rho_f}{2d_h}\left(\frac{133}{Re} + 2.33\right)\left(\frac{v_D}{\varepsilon}\right)^2 \tag{44}$$

where v_D is the Darcy velocity. The coefficients of 133 and 2.33 are found from the work of Yang et al [30] where these coefficients are used for flow through a randomly packed bed of spherical particles. Using this correlation for the pressure drop, the pumping work may be determined by:

$$W_{pump} = \dot{m}_f \left(\frac{\Delta p}{\eta \rho_f}\right) \tag{45}$$

where η is the efficiency of the pump. Following the example of Borbolla [4] the pump efficiency will be taken to be 0.8, as this is a common estimation made in fluid mechanics literature.

To assess the performance of the simulated magnetocaloric materials, two main performance metrics will be considered: the coefficient of performance (COP) and the cooling capacity (absorbed heat). The COP is a common performance metric used to estimate the efficiency of an AMR as a cooling system and compares the output cooling power to the total input power of the system, namely the power to operate the pump and motor for the magnetization system. The cooling capacity is calculated at the end of a cold blow period according to the following equation:

$$\dot{Q}_{ref} = \frac{1}{t_c}\int_{\frac{t_c}{2}}^{t_c} \dot{m}_f c_f \left(T_{CHEX} - T_f(x=0,t)\right) dt \tag{46}$$

where T_{CHEX} is the temperature of the cold heat exchanger. It is also necessary to compute the heat rejected to the environment after the completion of a warm blow period, which is achieved through use of the equation:

$$\dot{Q}_{rej} = \frac{1}{t_c}\int_0^{\frac{t_c}{2}} \dot{m}_f c_f \left(T_f(x = L, t) - T_{HHEX}\right) dt \tag{47}$$

where T_{HHEX} is the temperature of the hot heat exchanger. The COP is then defined as:

$$COP = \frac{\dot{Q}_{ref}}{W_{mag} + W_{pump}} \tag{48}$$

where the magnetic work term is expressed as:

$$W_{mag} = \dot{Q}_{rej} - \dot{Q}_{ref} \tag{49}$$

Normalization of the temperature, spatial, and temporal variables are performed in this simulation in order to obtain a dimensionless set of governing equations for the solid and fluid. By doing so regenerators operating at different frequencies or sizes may be more easily tested. The temperature of the solid and fluid are normalized by the temperature span set by the two heat exchangers:

$$T_s^* = \frac{(T_s - T_{CHEX})}{(T_{HHEX} - T_{CHEX})} \tag{50}$$

$$T_f^* = \frac{(T_f - T_{CHEX})}{(T_{HHEX} - T_{CHEX})} \tag{51}$$

The spatial variable is normalized over the length of the regenerator:

$$x^* = {}^{x}/_{L} \tag{52}$$

The time variable is normalized by the mean transit time of the heat transfer fluid traveling through the regenerator, expressed as:

$$t_r = {}^{L}/_{v} \tag{53}$$

where v is the interstitial velocity of the fluid obtained by dividing the Darcy velocity by the porosity of the regenerator. The resulting normalized time takes on the form:

$$t^* = {}^{t}/_{t_r} \tag{54}$$

Using these normalized quantities, the dimensionless form of the solid governing equation is now expressed as:

$$\frac{\partial T_s^*}{\partial t^*} = \alpha_1\left(T_f^* - T_s^*\right) + \alpha_2\left(\frac{\partial^2 T_s^*}{\partial x^{*2}}\right) \tag{55}$$

and the dimensionless fluid governing equation:

$$\frac{\partial T_f^*}{\partial t^*} = \alpha_3\left(T_s^* - T_f^*\right) - \alpha_4\left(\frac{\partial T_f^*}{\partial x^*}\right) + \alpha_5\left(\frac{\partial^2 T_f^*}{\partial x^{*2}}\right) \tag{56}$$

where the dimensionless coefficients for the governing equations are listed in *Tab. 3*.

Table 3: Normalized coefficients for the solid and fluid governing equations.

Normalized Governing Equation	Normalized Coefficient
Solid	$\alpha_1 = \frac{hLa_s}{\rho_s(1-\varepsilon)c_s(T_s,B)v}$
Solid	$\alpha_2 = \frac{k_{eff,s}}{\rho_s(1-\varepsilon)c_s(T_s,B)Lv}$
Fluid	$\alpha_3 = \frac{hLa_s}{\rho_f c_f \varepsilon v}$
Fluid	$\alpha_4 = \frac{Lc_f}{Lc_f}\left(\frac{\dot{m}_f}{\varepsilon A_c \rho_f v}\right) = 1$
Fluid	$\alpha_5 = \frac{k_{eff,f}}{\rho_f c_f \varepsilon Lv}$

For ease of reference the implicit effects of the magnetization system, pumping system, and normalized boundary conditions set by the heat exchangers for each blow period are presented in *Tab. 4*.

For an AMR device to be accurately simulated, there are a great deal of quantities to consider. Since the purpose of this simulation is to give a general sense of various magnetocaloric materials' performance, certain limitations must be set in place for the

AMR geometry and size. The current Matlab model is set for a regenerator geometry of randomly packed spherical particles of constant particle diameter and porosity.

Table 4: Governing equation implicit effects and boundary conditions after normalizing.

Warm Blow	Cold Blow
$0 \le t^* \le \frac{1}{2ft_r}$	$0 \le t^* \le \frac{1}{2ft_r}$
$\dot{m}_f(t^*) = \dot{m}_f$	$\dot{m}_f(t^*) = -\dot{m}_f$
$B(t^*) = B_{max}$	$B(t^*) = B_{min}$
$T_f^*(x^* = 0, t^*) = 0$	$T_f^*(x^* = 1, t^*) = 1$
$\left.\frac{\partial T_s^*}{\partial x^*}\right\|_{0,t^*} = \left.\frac{\partial T_s^*}{\partial x^*}\right\|_{1,t^*} = \left.\frac{\partial T_f^*}{\partial x^*}\right\|_{1,t^*} = 0$	$\left.\frac{\partial T_s^*}{\partial x^*}\right\|_{0,t^*} = \left.\frac{\partial T_s^*}{\partial x^*}\right\|_{1,t^*} = \left.\frac{\partial T_f^*}{\partial x^*}\right\|_{0,t^*} = 0$

In regard to the size of the regenerator, an optimal aspect ratio (regenerator length over diameter) is used based on predictions made by a similar model [6]. The mass of magnetocaloric material contained within the regenerator is also set to a constant value among multiple simulations. In the majority of simulations water is used as the heat transfer fluid, due to its favorable thermal properties, but a comparison is performed with a 50-50 water-glycol mixture. Unless otherwise explicitly stated, the quantities listed in *Tab. 5* are constant over the course of the performed simulations.

The main system parameters that will be varied to determine their effects on overall MCM performance are the cycle frequency, mass flow rate (utilization factor), and heat exchanger temperature span.

Table 5: AMR geometric parameters held constant during multiple simulations.

Parameter	Value
Particle Diameter (d_p)	400 μm
Porosity (ε)	0.36
Aspect Ratio	3
MCM Mass	0.75 kg

AMR systems operate at very low frequencies, between 0.5 – 2 Hz, in most practical applications so frequencies within this range will be investigated. The effects of different fluid flow rates are determined by altering the value of the utilization factor, which for this thesis will take on values in the range of 0.5 – 2. Magnetocaloric material performance can be greatly influenced by the temperature span in which they operate. The effects on performance of increasing and decreasing the temperature span set by the heat exchangers is investigated in this simulation as well, but the actual temperature span used will depend on the selection of material.

The AMR simulation is created in Matlab and uses the built-in "pdepe" function to solve the coupled partial differential equations describing the solid and fluid temperatures. Before the simulation can initiate a large number of cycle parameters, magnetocaloric material physical properties, and heat transfer fluid physical properties must be input so the regenerator geometry parameters can be calculated. "If" statements are in place to quickly select the correct physical properties of the selected MCM and heat transfer fluid. Next, data for the heat capacity and adiabatic temperature change of the MCM at different magnetic field values are loaded into the program. Data for the simulations involving gadolinium are provided by the mean-field model, while the data for the NiMnCuGa alloy is provided by prior experimental measurements and calculations.

In order to initialize the solid and fluid temperatures in the simulation, a linear temperature profile is enforced spanning from the cold heat exchanger temperature to hot heat exchanger temperature. The precision of the spatial and temporal stepping can be

modified to any desired value, but 110 spatial steps and 75 time steps have been used. It was determined that these values gave the best compromise between model accuracy and computation time. The simulation then runs through the four AMR cycles of magnetization, warm blow, demagnetization, and cold blow for each utilization factor value. The AMR cycle continues for a given utilization factor value until the solid and fluid temperatures reach steady state conditions. In the current model steady state is considered to be achieved once the temperature profiles of two consecutive AMR cycles are less than the prescribed tolerance of 10^{-6} K. To ensure that the simulation does not end prematurely it is required that at least 60 AMR cycles be completed before steady state can be achieved. If the temperature profiles do not converge after 250 completed cycles, then the simulation moves on to the next flow rate.

Solving of the solid and fluid governing equations can be done simultaneously using the "pdepe" function in Matlab. Function files are created for the warm blow and cold blow processes of the AMR cycle. During these steps of the simulation the temperature profiles of the solid and fluid are calculated at each spatial step on the regenerator for every time step. Once the qualifications for steady state conditions have been met, the solid and fluid temperatures of the last completed AMR cycle are saved so that the evolution of the temperature profiles for a given flow rate may be observed. Also included within the warm and cold blow function files is the calculation of the rejected heat and absorbed heat, respectively. Upon calculating the rejected and absorbed heat, the COP may be calculated and the performance of the magnetocaloric material is determined.

Example outputs for the temperature profiles of the main AMR processes are presented using gadolinium as the regenerator material and water as the heat transfer fluid. The remaining operational parameters selected during this simulation are presented in *Tab. 6*.

Table 6: Parameters for the AMR cycle using gadolinium and water.

Frequency [Hz]	MCM Mass [kg]	Mass Flow Rate [kg/s]	Magnetic Field Strength [T]	HHEX Temperature [°C]	CHEX Temperature [°C]
1	0.75	0.0563	1.8	25	5

The model first simulates the adiabatic magnetization of the regenerator bed, shown in *Fig. 19*.

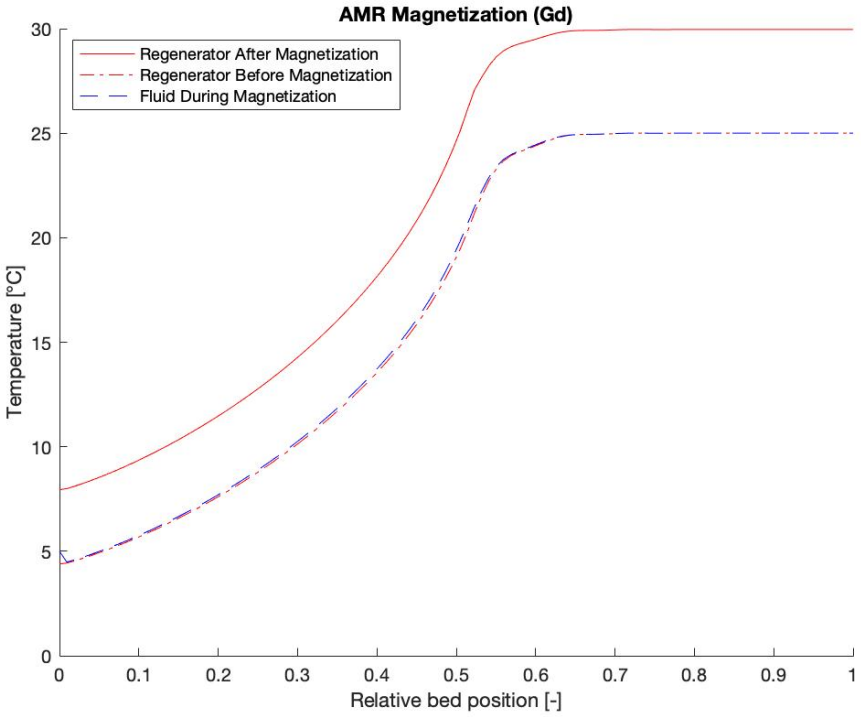

Figure 19: AMR magnetization process for gadolinium.

During this process the temperature profile of the regenerator bed rises due to the magnetocaloric effect. The temperature profile of the heat transfer fluid does not change during this process and matches that of the regenerator bed before magnetization occurs.

The second process that is simulated is the warm blow period, shown in *Fig. 20*.

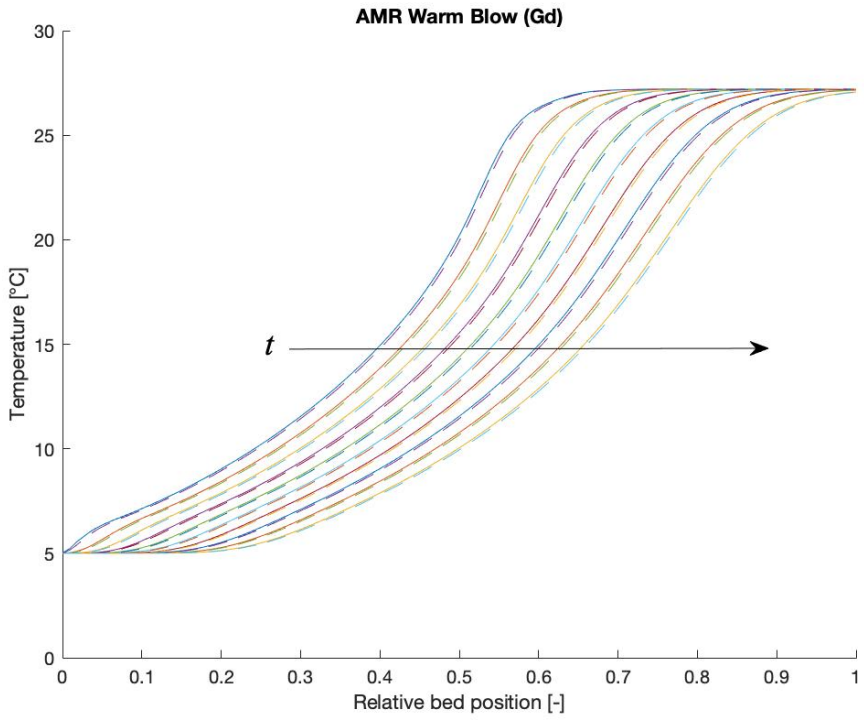

Figure 20: AMR warm blow process for gadolinium.

The solid lines in this plot represent the magnetocaloric material temperature profiles and the dashed lines represent those of the heat transfer fluid. Time evolution of the temperature profiles move from the right to left of the plot with each set of solid/dashed lines corresponding to a single time step. In *Fig. 20* temperatures are plotted every 5 time steps, starting at the 5^{th} step and ending at the 50^{th}, with the total amount of elapsed time being approximately 0.3 s. At the far right of the plot the temperatures seen to exceed that

of the hot heat exchanger temperature of 25 °C. These temperatures, namely those of the heat transfer fluid, are used to calculate the rejected heat during a warm blow period.

The third process in the simulation is the adiabatic demagnetization of the regenerator bed, shown in *Fig. 21*.

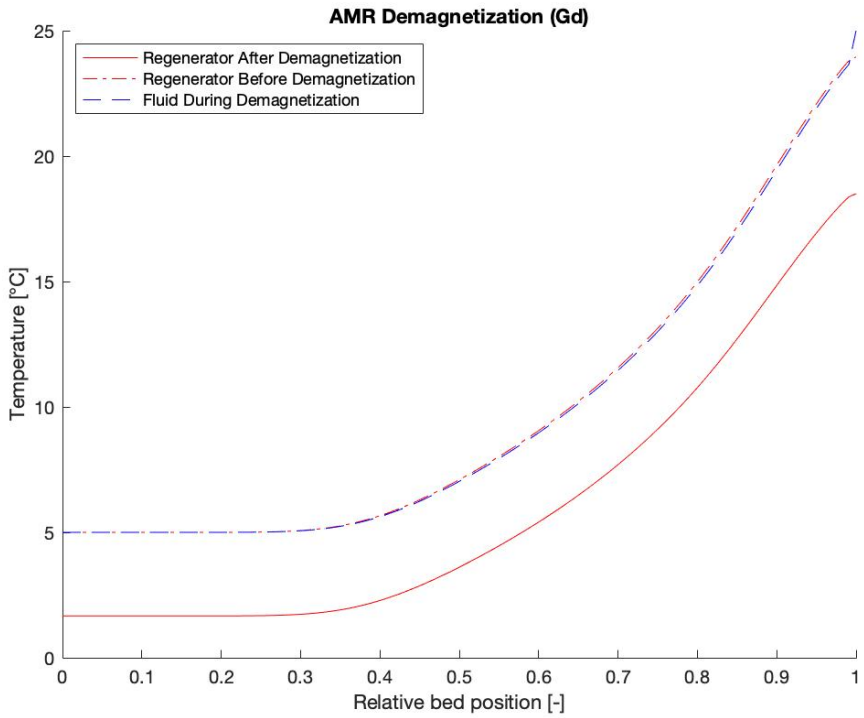

Figure 21: AMR demagnetization process for gadolinium.

Conversely to the magnetization process, the temperature of the MCM in the regenerator bed adiabatically decreases as a result of the magnetocaloric effect. Once more the temperature of the heat transfer fluid remains unchanged during the demagnetization process.

The final process to complete the AMR cycle is the cold blow period, as shown in *Fig. 22*. For the cold blow process time evolves from the right to the left of the plot, as indicated by the arrow. Once again, the solid lines pertain to regenerator temperatures and the dashed lines pertain to fluid temperatures. During this process it can be seen that

the temperature profiles fall to a point lower than the set cold heat exchanger temperature of 5 °C.

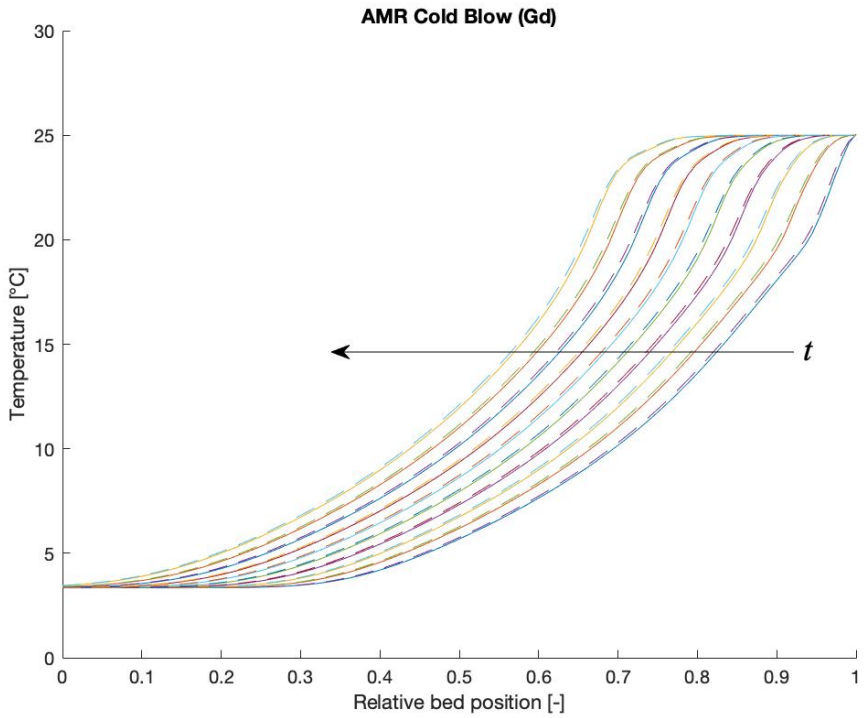

Figure 22: AMR cold blow process for gadolinium.

The fluid temperatures at this point are used to calculate the absorbed heat (cooling capacity) that the magnetocaloric material is capable of providing.

V. RESULTS

5.1 MEAN-FIELD MODEL: GADOLINIUM

In this section the magnetothermal properties of gadolinium, as determined from the developed mean-field model, are presented. The results collected from this model allow for thermodynamically accurate data for gadolinium to be used in the AMR simulation, which provides a sound basis for validating the current AMR model. The results presented for gadolinium show the effects that varying magnetic field strengths have on its magnetothermal properties. The current model also takes into account the electronic contribution of the total entropy, a quantity often ignored due to its small impact. With the aid of the mean-field model the magnetothermal properties of any SOMT material may be calculated, making it an extremely useful tool for MCM performance testing in the AMR simulation.

In *Fig. 23*, it can be seen that at zero applied magnetic field the specific magnetic entropy value reaches its maximum at gadolinium's Curie temperature before leveling out. As the applied magnetic field value increases, the specific magnetic entropy value decreases for a given temperature. The greatest difference in the magnetic entropy values is also seen at the Curie temperature. The temperature evolution of the change in specific magnetic entropy is illustrated in *Fig. 24*.

Here the change in specific magnetic entropy is presented for applied magnetic field swings of 2, 5, and 10 T. As confirmed by *Fig. 24*, the change in specific magnetic entropy is maximum at the Curie point and increases with larger magnetic field swings. Since the change in total entropy must be zero, under adiabatic conditions, a larger

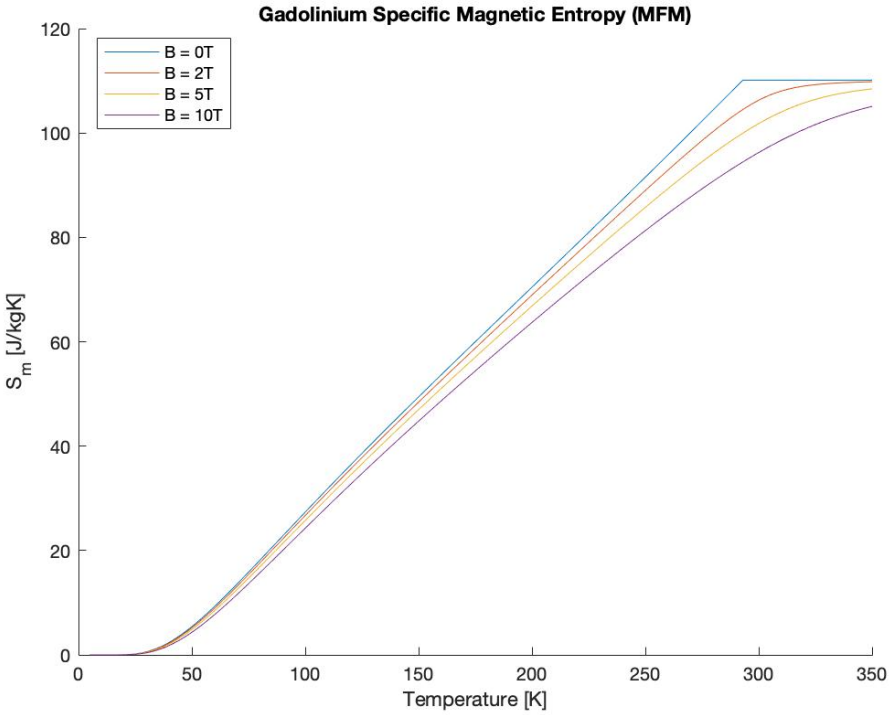

Figure 23: Gadolinium specific magnetic entropy vs. temperature.

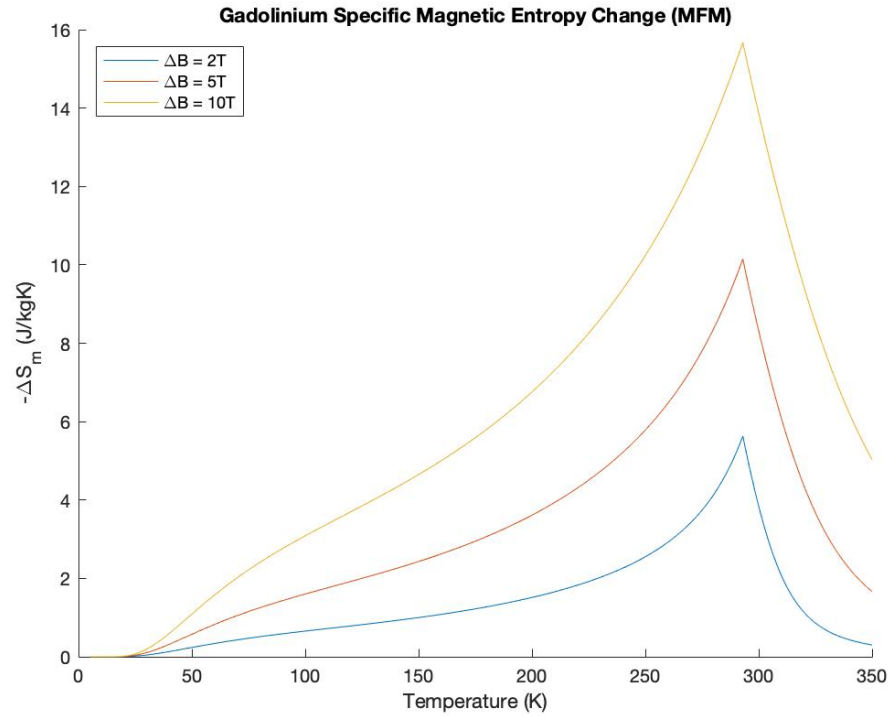

Figure 24: Gadolinium change in specific magnetic entropy vs. temperature.

magnetic entropy change indicates a larger change in the lattice contribution, thus a larger temperature change in the material. Also of note are the widths of the specific magnetic entropy change curves. They encompass a large temperature range, indicating that gadolinium can provide cooling over significant temperature spans.

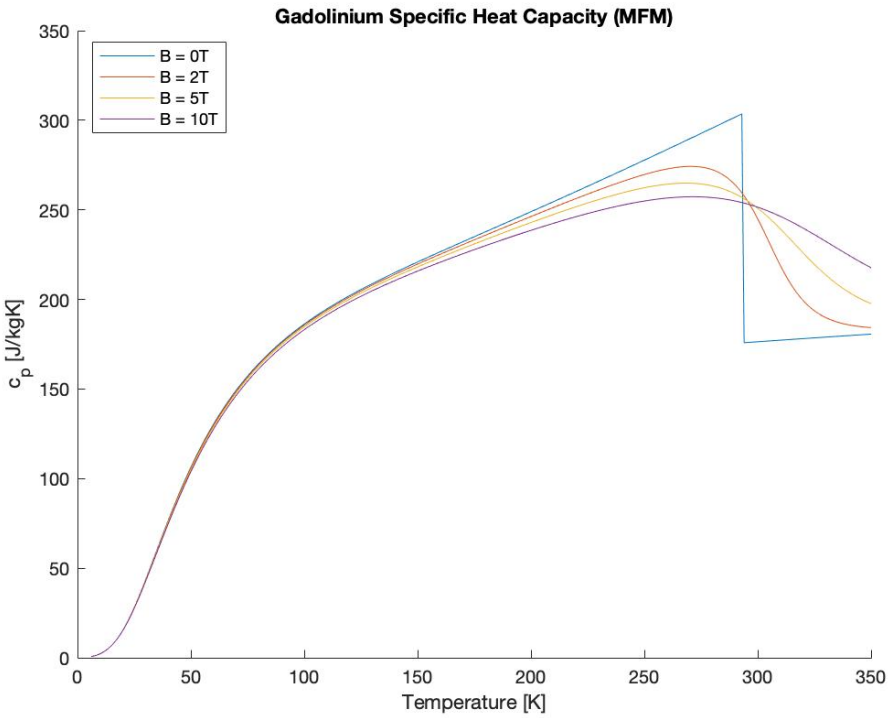

Figure 25: Gadolinium specific heat capacity vs. temperature.

In *Fig. 25* the specific heat capacity for gadolinium with inclusion of the electronic contribution is presented for magnetic fields ranging from 0-10 T. When no magnetic field is applied, the heat capacity peaks at the Curie temperature where it is then observed to steeply decrease. The maximum value of the heat capacity at zero applied field is approximately 303 J/kgK. The curves of the heat capacity also become more constant around the Curie temperature as the strength of magnetic field is increased.

The final output of the mean-field model is the adiabatic temperature change, as presented in *Fig. 26*. Since this quantity depends heavily on the change in magnetic

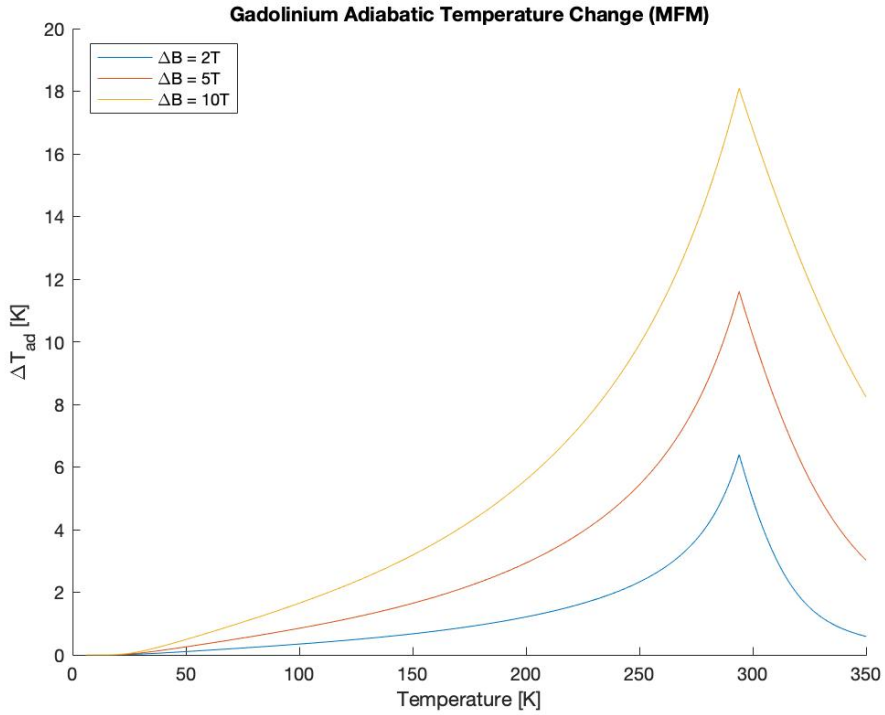

Figure 26: Gadolinium adiabatic temperature change vs. temperature.

entropy, many of the same features can be seen. The adiabatic temperature change is greatest where the magnetic entropy change peaks, which again occurs at the Curie temperature. The magnetic field and temperature dependent nature of the adiabatic temperature change is visible as well. Larger applied magnetic fields cause overall increases to the adiabatic temperature change over the tested temperature range, and the magnitude of ΔT_{ad} decreases more rapidly at temperatures above the Curie point.

5.2 1D AMR MODEL: GADOLINIUM

In this section the results of the mean-field model for gadolinium are implemented in the AMR simulation. Gadolinium is used as a benchmarking material to ensure the simulation operates as intended, and to get a baseline of material performance. Aside from this, gadolinium is used to analyze the effects that certain operational parameters have on overall system performance. Material performance is based on the cooling capacity (absorbed heat from load) and coefficient of performance. Unless otherwise noted, all gadolinium simulations are run for a magnetic field strength of 1.8 T.

The effect of mass flow rate on the cooling capacity is seen through variation in the nondimensional utilization factor at a given operational frequency.

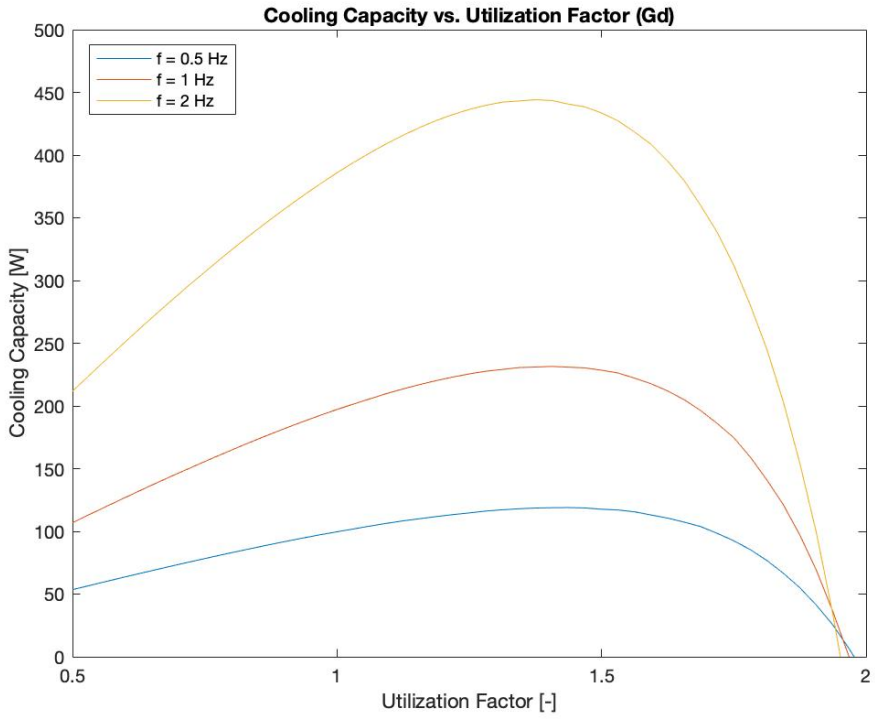

Figure 27: Gadolinium cooling capacity vs. utilization factor for varying frequencies.

For utilization factors up to ~1.5 the cooling capacity of the AMR increases, but quickly approaches zero as the utilization factor increases to its maximum value. For high utilization factors the mass flow rate is too high for sufficient heat transfer between the regenerator and circulating fluid, which results in the inability to provide useful cooling. The effect of cycle frequency on the cooling capacity is clearly seen in *Fig. 27* as well, with higher operating frequencies capable of providing larger cooling capacities. For all three tested frequencies a utilization factor of approximately 1.4 provides the maximum cooling power.

While cooling capacity trends can be obtained when plotted against the utilization factor, plotting against the true mass flow rate is more physically revealing.

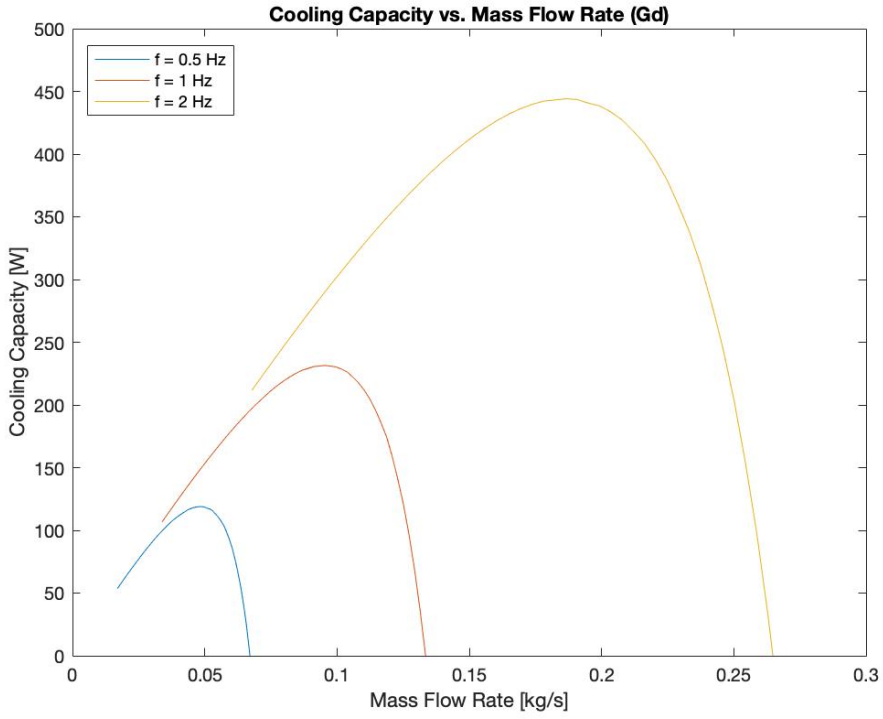

Figure 28: Gadolinium cooling capacity vs. mass flow rate for varying frequencies.

From *Fig. 28*, the true effects of mass flow rate on the cooling capacity can be seen. For lower frequencies, the regenerative capacity of the magnetocaloric material is

overwhelmed at lower flow rates. As frequency is increased there is a noticeable widening of the cooling capacity curves, meaning that higher operating frequencies can withstand a larger range of flow rates before the cooling capacity becomes insignificant. Perhaps the biggest difference seen between *Fig. 27* and *Fig. 28* are the points at which the cooling capacity is maximum for each operating frequency. For 0.5 Hz the cooling capacity peaks around a flow rate of ~0.05 kg/s, for 1 Hz the peak is at ~0.1 kg/s, and for 2 Hz the peak is at ~0.18 kg/s.

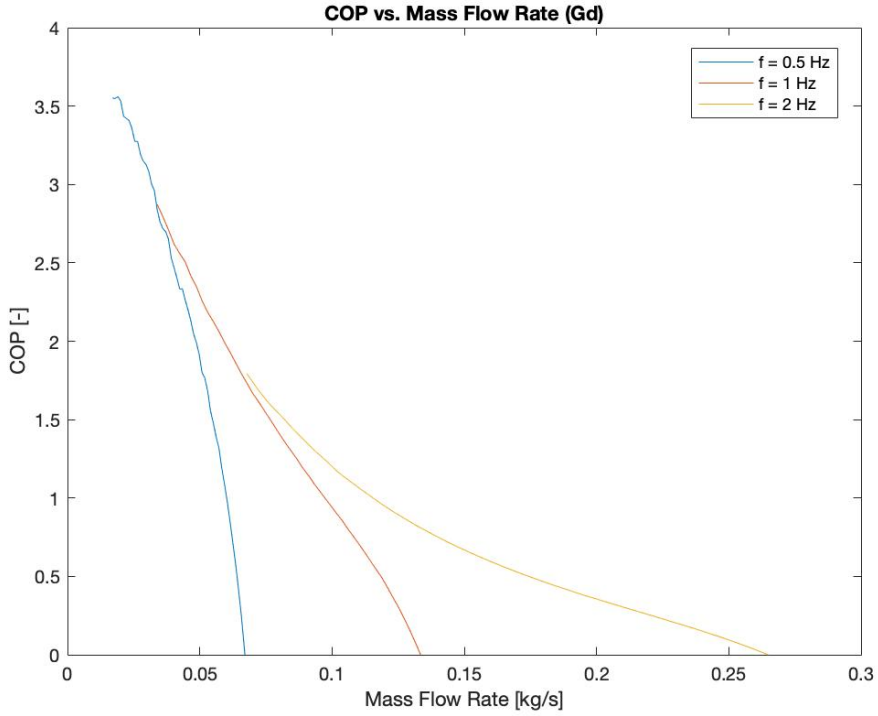

Figure 29: Gadolinium COP vs. mass flow rate at varying frequencies.

In *Fig. 29* the efficiency (COP) of the AMR is plotted against the mass flow rate. The COP is maximum at the lowest flow rate and decreases as flow rate increases. As flow rate increases, so does the pumping and magnetic work required by the system which largely decreases efficiency when cooling powers are not high. The effect of varying operational frequency on the efficiency of an AMR is clearly seen as well. Lower

frequencies are capable of achieving higher efficiency values, but the efficiency decreases much more rapidly than simulations run at higher frequencies. Similarly to the results of the cooling capacity vs. mass flow rates, the simulation running at 2 Hz maintains a more consistent COP value over a larger range of flow rates.

Since the greatest efficiency is seen at the lowest flow rate values, there is an obvious compromise that must be made between cooling capacity and efficiency. By combining the plots of cooling capacity and COP against the mass flow rate, plots of the efficiency versus cooling capacity may be created. These types of plots are useful tools in determining the desired combination of cooling power and efficiency for a given flow rate. *Fig. 30* shows the resulting combination of *Fig. 28* and *Fig. 29*.

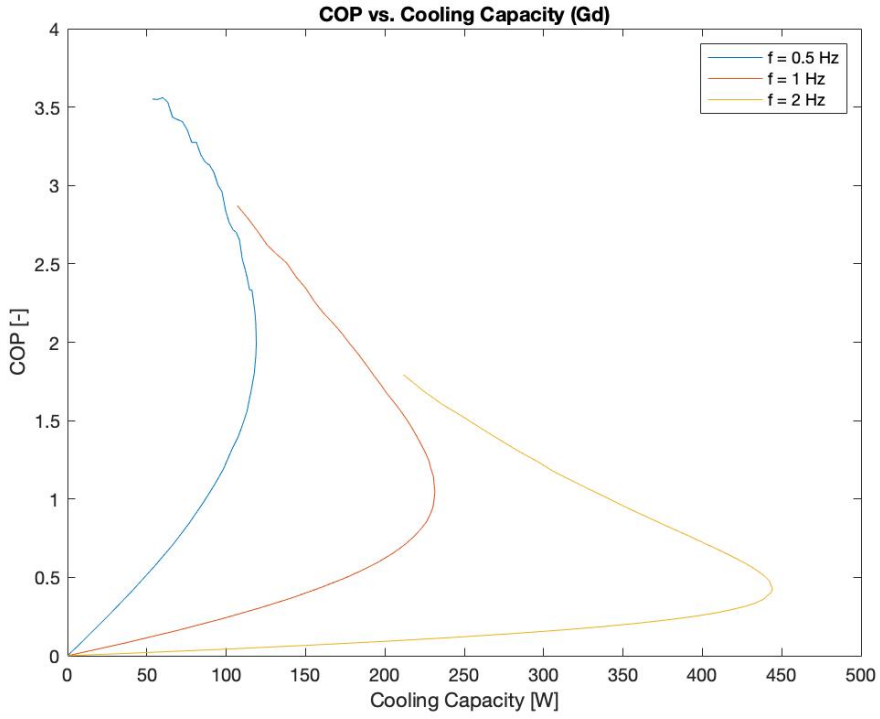

Figure 30: Gadolinium COP vs. cooling capacity for varying frequencies.

For these types of plots, the mass flow rate increases from the top to bottom, since COP are values are highest at the lowest flow rates. By setting limits on the desired

cooling capacity and efficiency for a given application, an optimal operative range can be easily viewed from *Fig. 30*. The simulation run for a frequency of 1 Hz appears to offer the best compromise between efficiency and cooling power by offering a cooling power between 130-210 W of cooling over an efficiency range of 2.5-1.5.

Next, the mass of magnetocaloric material was varied in order to observe its effect on the AMR performance. The results of these simulations are presented in *Fig. 31* and were run using a frequency of 1 Hz. An increase in the mass of magnetocaloric material contained within the regenerator bed increases the magnitude of potential cooling power at the cost of higher mass flow rates. With more MCM mass in the regenerator more heat is capable of being absorbed and expelled at the end of the blow processes. Due to this, higher mass flow rates are required so that sufficient heat transfer can take place between the fluid and solid matrix. In terms of efficiency, regenerators containing more magnetocaloric material mass are able to provide larger cooling powers at a given efficiency value. For example, at a COP value of 2 a regenerator containing 0.5 kg of Gd can provide 120 W of cooling, 0.75 kg provides 180 W of cooling, and 1 kg provides 225 W of cooling.

The effect of varying magnetic field strength is also tested using an operational frequency of 1 Hz and MCM mass of 0.75 kg. The results of these simulations are shown in *Fig. 32*. As to be expected, an increase in the applied magnetic field strength causes an increase in the overall AMR performance. For a given mass flow rate the cooling capacity is always higher when a larger magnetic field is applied. Increased magnetic field strengths show that it takes higher flow rates to overwhelm the regenerator, with the simulation run for a 2.4 T magnetic field still providing a nonzero cooling capacity at the

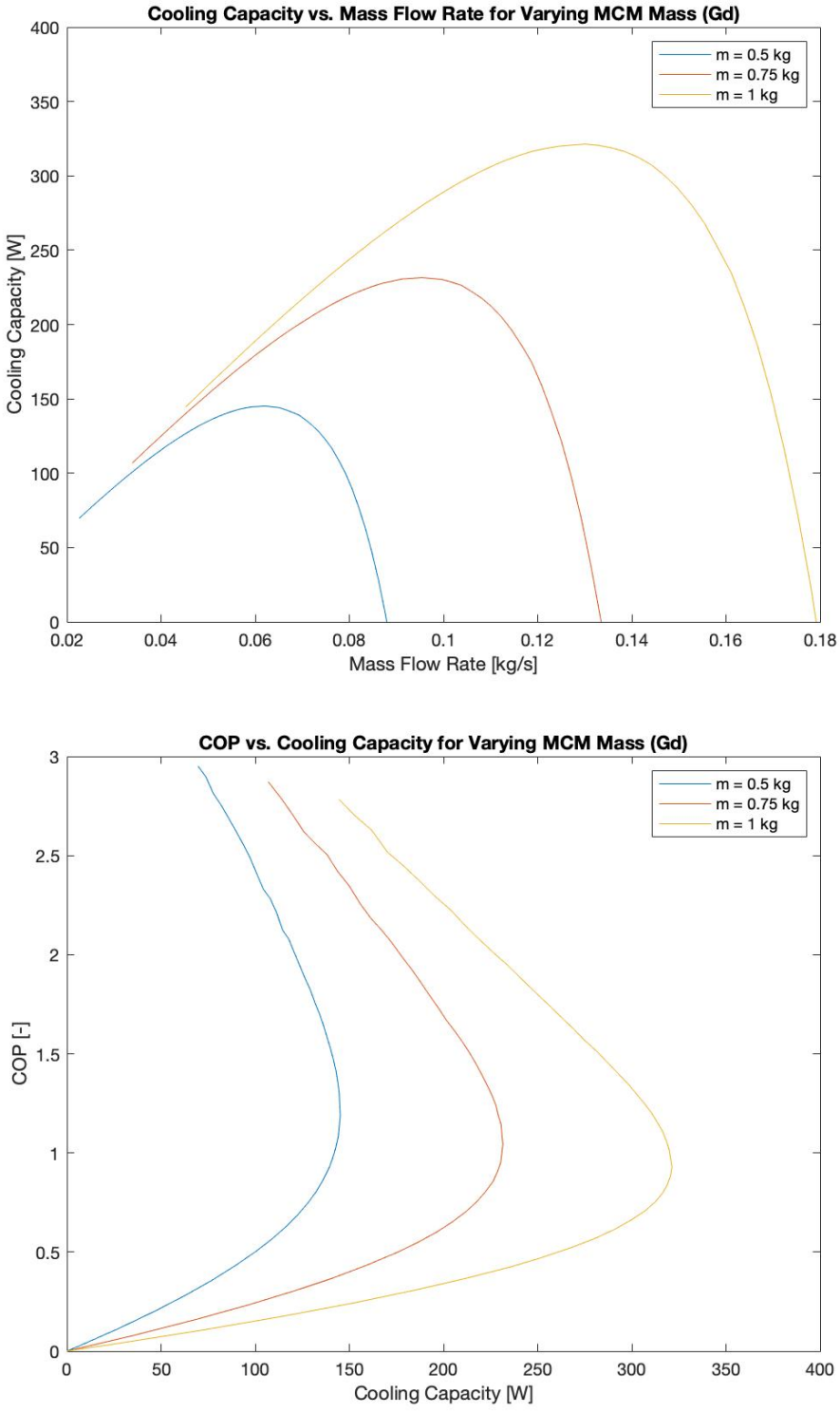

Figure 31: Gadolinium cooling capacity vs. mass flow rate and COP vs. cooling capacity for varying MCM mass.

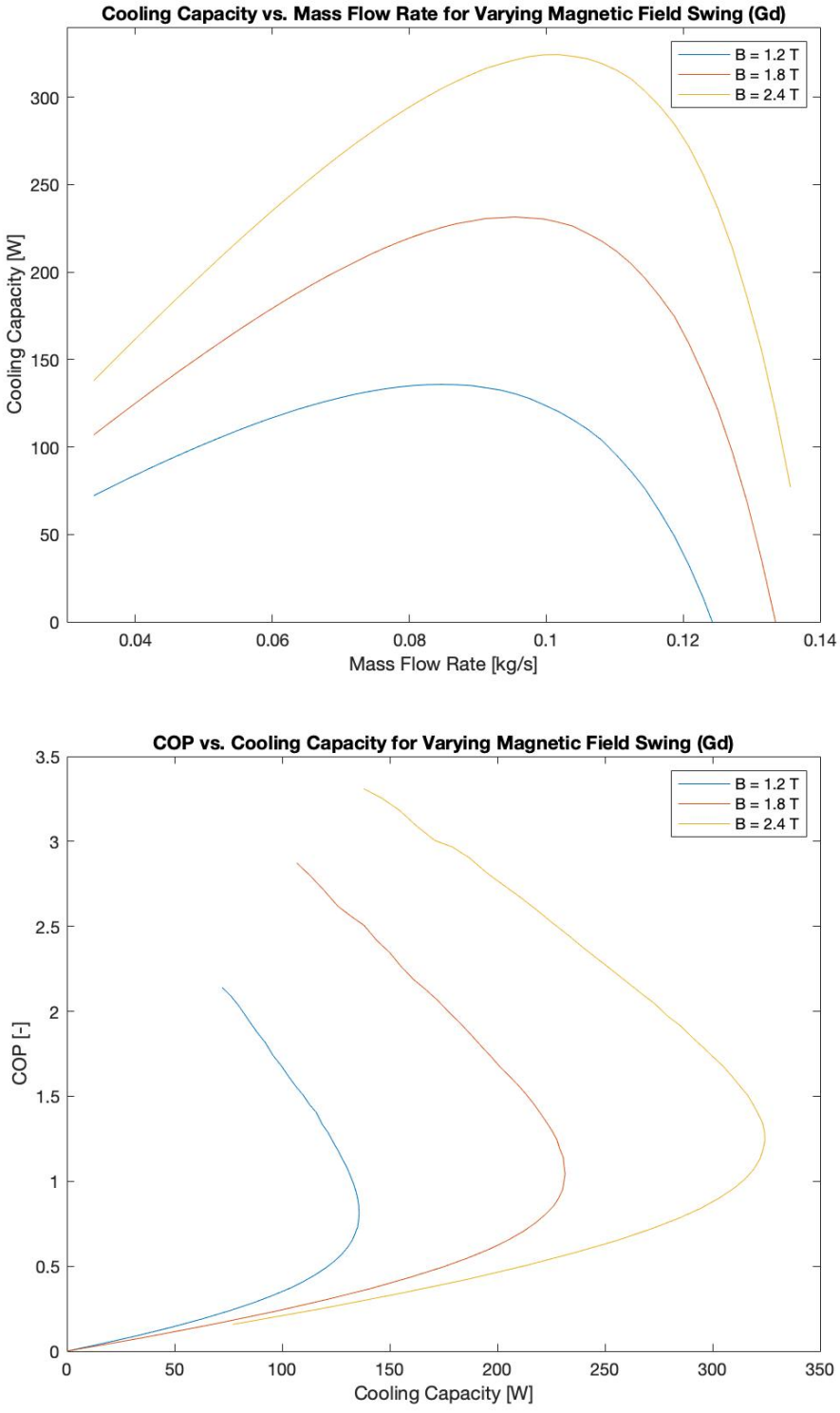

Figure 32: Gadolinium cooling capacity vs. mass flow rate and COP vs. cooling capacity for varying magnetic field swings.

maximum tested flow rate. A significant increase in cooling power can also be observed at specific COP values. Once again, the 2.4 T magnetic field not only shows the highest attainable cooling capacity, but also the highest efficiency when compared to the other field strengths.

The effect of varying temperature span (heat exchanger temperatures) on AMR performance is presented next. For these simulations the cold heat exchanger temperature was held constant at 5 °C, while the hot heat exchanger temperature was varied from 20, 25, and 30 °C. The resulting plots are shown in *Fig. 33*. It can be observed that for an increasing temperature span there is a decrease in overall AMR performance. The largest tested temperature span of 25 °C causes the regenerator to become overwhelmed at lower flow rates and provides the lowest peak cooling capacity. AMR systems with larger temperature spans are seen to operate at lower efficiencies as well. These results reinforce the importance of magnetocaloric material selection for a given operating temperature range. If the peak adiabatic temperature change is not captured within the operating temperature, then the overall MCE effectiveness is reduced.

A final consideration is the effect of heat transfer fluid selection on AMR performance. Water is typically used in AMR devices due to its high heat capacity but can cause corrosion to the MCM over many cycles. The results of using a 50-50 water-glycol mixture as a heat transfer fluid, as compared to water, are shown in *Fig. 34*. The water-glycol mixture has a slightly lower heat capacity than that of pure water, which is shown to negatively affect the cooling capacity for a given mass flow rate. At the lower range of mass flow rates differences in cooling capacity are not significant, only differing by about 10-15 W.

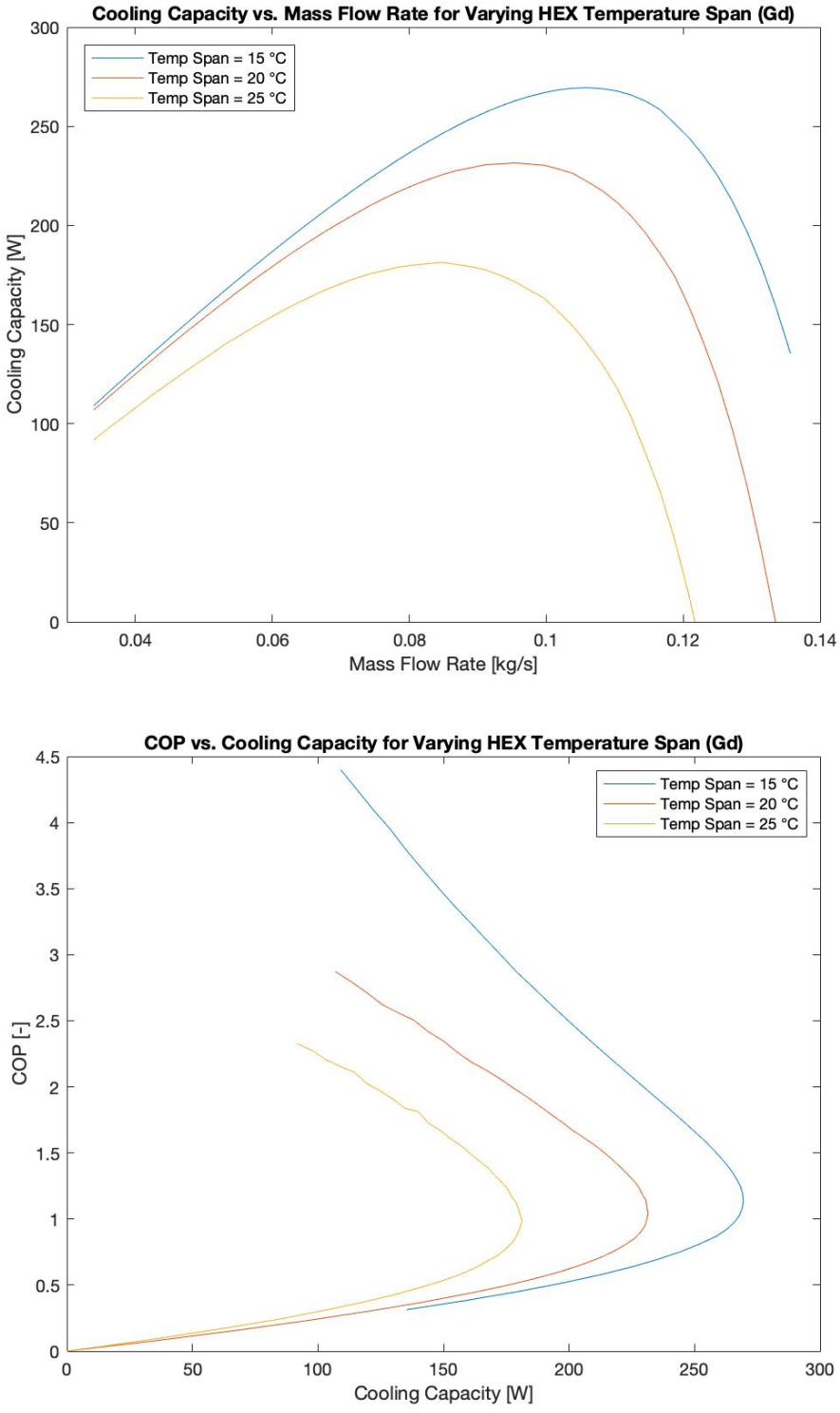

Figure 33: Gadolinium cooling capacity vs. mass flow rate and COP vs. cooling capacity for varying heat exchanger temperature spans.

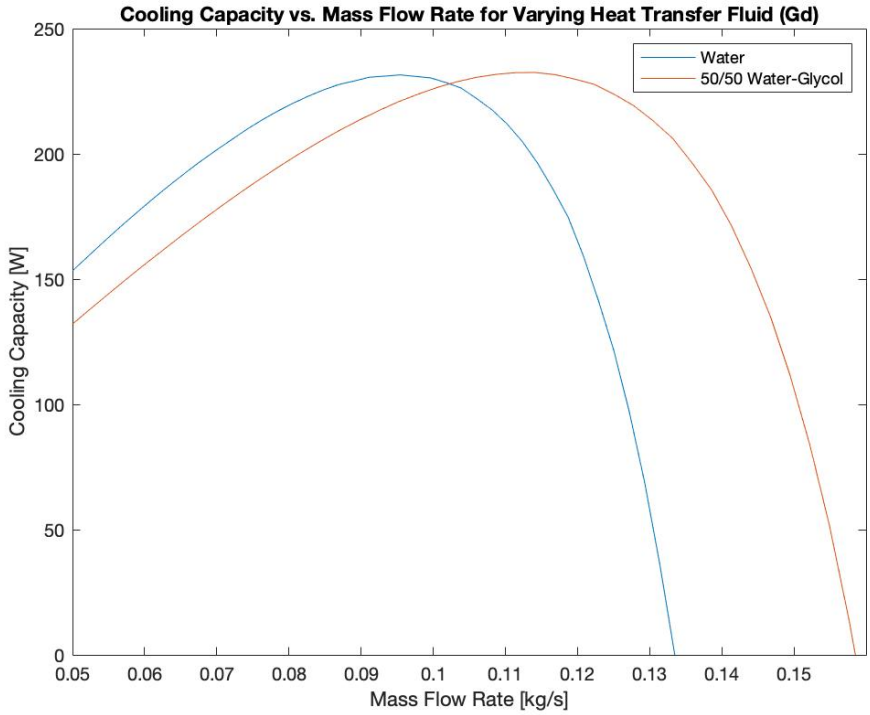

Figure 34: Gadolinium cooling capacity vs. mass flow rate for varying heat transfer fluid.

At a mass flow rate of ~0.13 kg/s the cooling capacity achieved by the water-glycol mixture matches that of pure water, before showing greater performance losses at higher flow rates.

5.3 1D AMR MODEL: NI-MN-CU-GA ALLOY AFTER SATC

In this section the performance of the $Ni_{0.50}Mn_{0.19}Cu_{0.06}Ga_{0.25}$ alloy after SATC is presented. Since this alloy is a FOMT material and cannot have its adiabatic temperature change calculated through the mean-field model, an equation developed by Fabbrici et al [31] for such materials is used. The equation to determine the adiabatic temperature change of the $Ni_{0.50}Mn_{0.19}Cu_{0.06}Ga_{0.25}$ alloy, both before and after SATC, is presented below:

$$\Delta T_{ad} = \frac{\Delta S_{mag} \cdot \Delta T_M}{\Delta S_{mag} + \Delta T_M \cdot {c_p^M}/{T_M}} \tag{57}$$

where T_M is the martensitic transformation temperature, ΔT_M is the change in martensitic transformation temperature, and c_p^M is the heat capacity of the martensitic phase.

The martensitic heat capacity of this alloy is obtained from measurements using a physical properties measurement system (PPMS). The raw data collected for the heat capacity of the as received and after SATC sample are presented in *Fig. 35* and *Fig. 36*. From the heat capacity curves, the values of the martensitic transformation temperature and change in martensitic transformation temperature for a given magnetic field strength may be obtained from the peak heat capacity values. The temperature at which the heat capacity curve peaks is taken as the martensitic transformation temperature, and the difference in temperature between peaks at a given field value and zero field is taken as the change in martensitic transformation temperature.

Using the data obtained from the change in magnetic entropy and heat capacity curves for the AR and SATC $Ni_{0.50}Mn_{0.19}Cu_{0.06}Ga_{0.25}$ alloy, the adiabatic temperature change is calculated over for a range of temperatures. The resulting adiabatic temperature

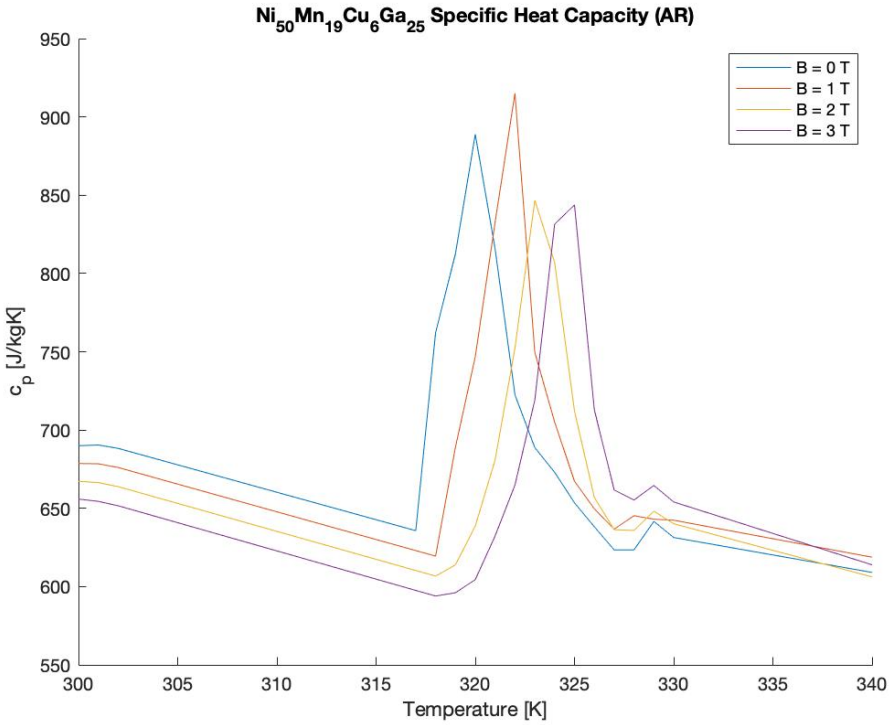

Figure 35: Raw data for $Ni_{0.50}Mn_{0.19}Cu_{0.06}Ga_{0.25}$ specific heat capacity (AR).

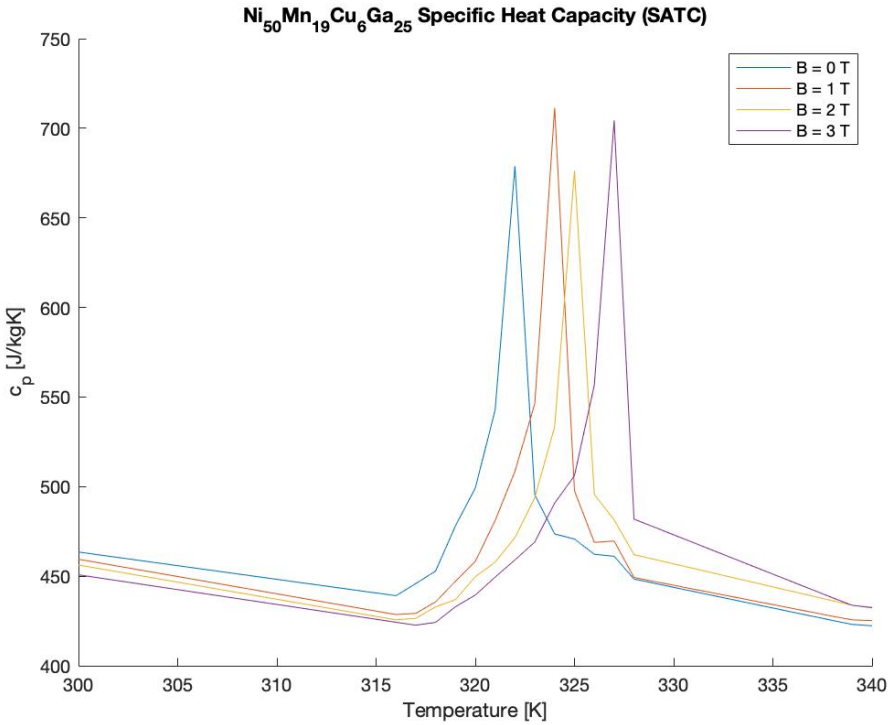

Figure 36: Raw data for $Ni_{0.50}Mn_{0.19}Cu_{0.06}Ga_{0.25}$ specific heat capacity (SATC).

curves for the AR and SATC samples are shown, respectively, in *Fig. 37* and *Fig. 38*.

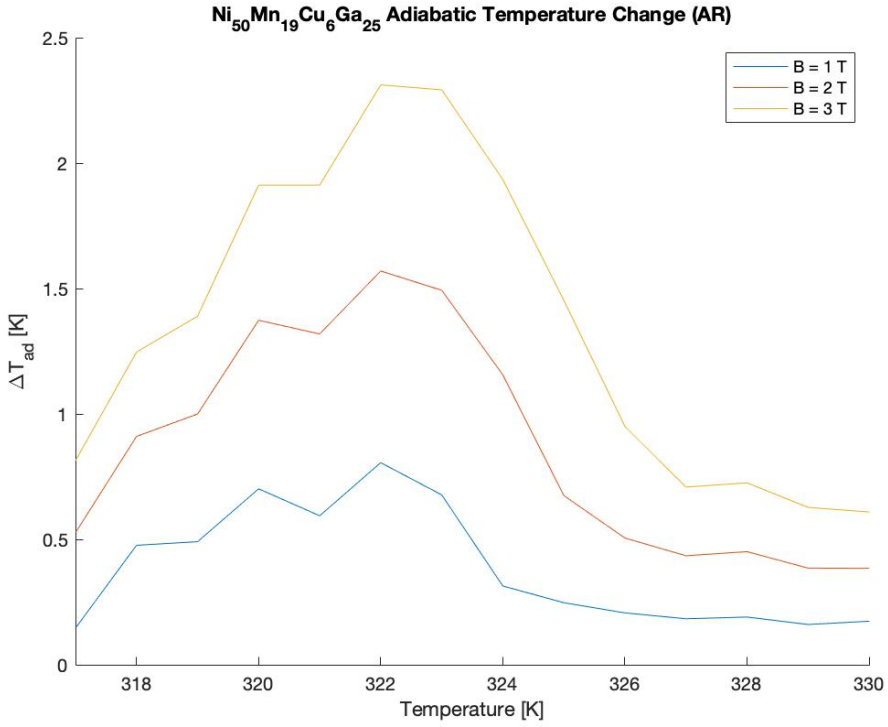

Figure 37: $Ni_{0.50}Mn_{0.19}Cu_{0.06}Ga_{0.25}$ adiabatic temperature change (AR).

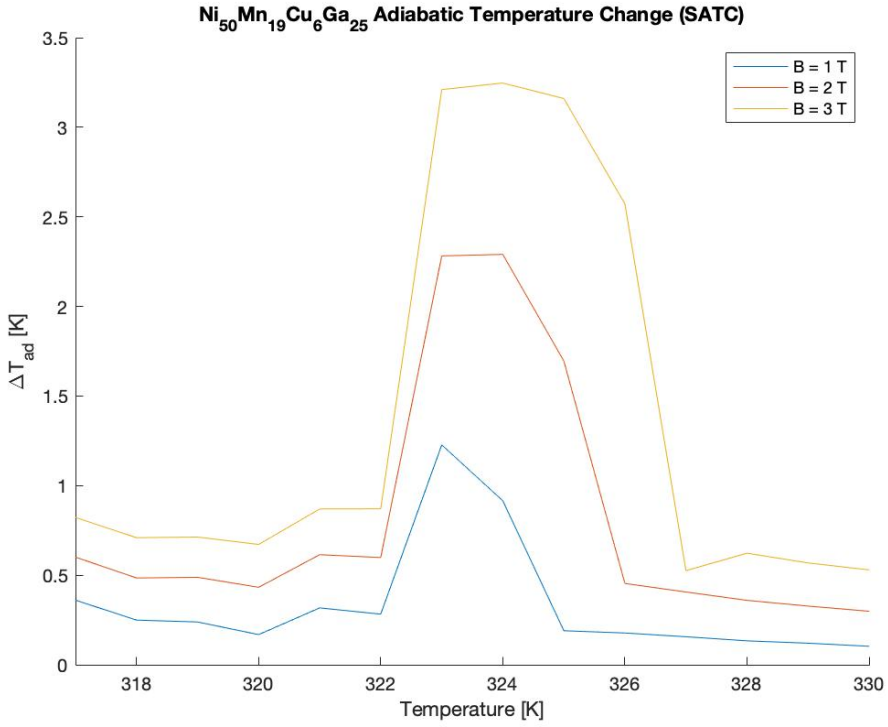

Figure 38: $Ni_{0.50}Mn_{0.19}Cu_{0.06}Ga_{0.25}$ adiabatic temperature change (SATC).

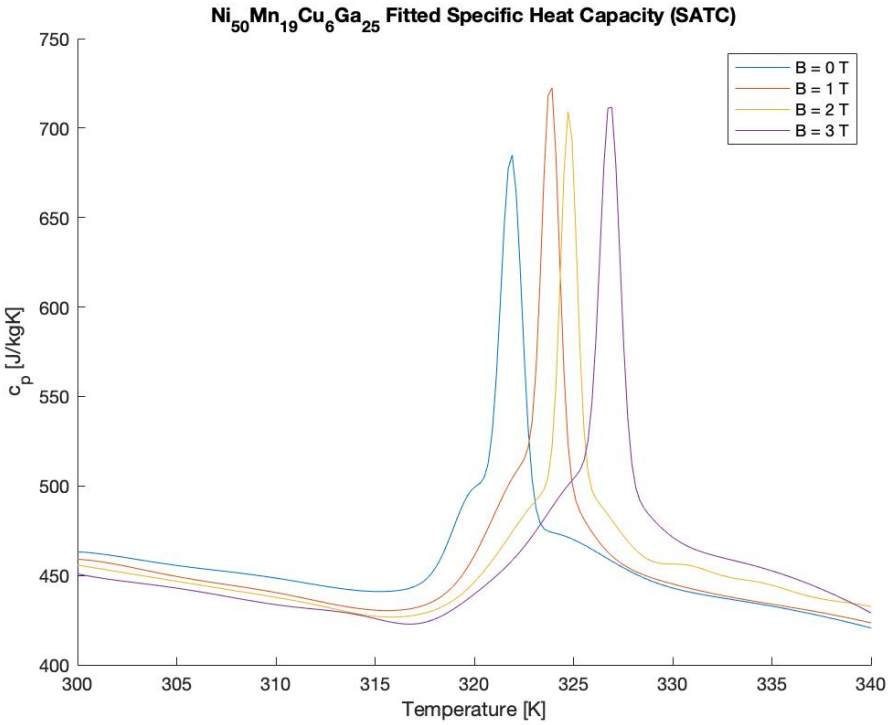

Figure 39: Fitted data for $Ni_{0.50}Mn_{0.19}Cu_{0.06}Ga_{0.25}$ specific heat capacity (SATC).

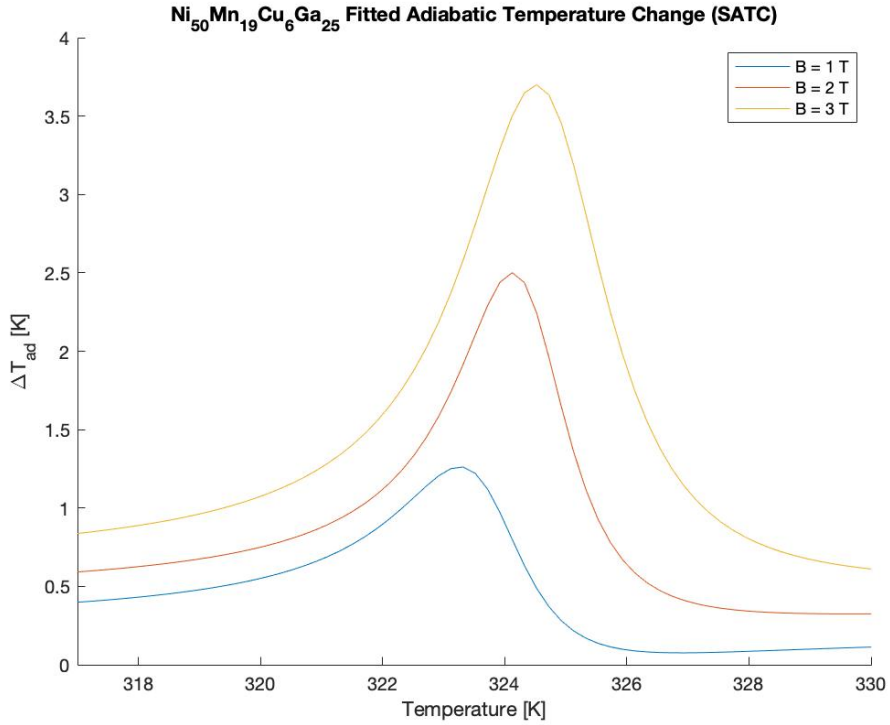

Figure 40: Fitted data for $Ni_{0.50}Mn_{0.19}Cu_{0.06}Ga_{0.25}$ adiabatic temperature change (SATC).

For the purpose of simulation, curve fits were applied to both the heat capacity and adiabatic temperature change data for the after SATC material. The raw data for the heat capacity was fit using a Gaussian method with 6 terms, with the resulting R^2 values for each magnetic field strength being greater than 0.98. The calculated plots of the adiabatic temperature change were fit using a rational method with numerator and denominator terms of degree 2. The fits of the adiabatic temperature changes showed slightly less agreement, with R^2 values ranging between 0.84-0.94. The fitted data required by the AMR simulation are shown in *Fig. 39* and *Fig. 40*.

Taking into account the results from the simulations using gadolinium as the regenerator material, the simulations run for the SATC Ni-Mn-Cu-Ga alloy use an operating frequency of 1 Hz, MCM mass of 0.75 kg, and use the same geometric parameters listed in *Tab. 5*. In an effort to maximize the performance of this material during testing, specific temperature spans were set for each magnetic field strength so as to center the peak adiabatic temperature change about the heat exchanger temperatures. The associated temperature spans for each of the three tested magnetic field strengths are shown in *Tab. 7*.

Since the peak value of the adiabatic temperature change increases with increasing magnetic field strength, a single temperature span during testing was undesirable.

Table 7: Operating temperature spans for Ni-Mn-Cu-Ga simulations.

Magnetic Field Swing [T]	HHEX Temperature [°C]	CHEX Temperature [°C]
1	51.1716	47.5535
2	52.3776	48.3575
3	52.9807	48.9606

Other material properties required in the simulation are the density and thermal conductivity. The density of the SATC Ni-Mn-Cu-Ga alloy was measured to be 8001.6 kg/m^3 and the thermal conductivity is 8.8867 W/m•K.

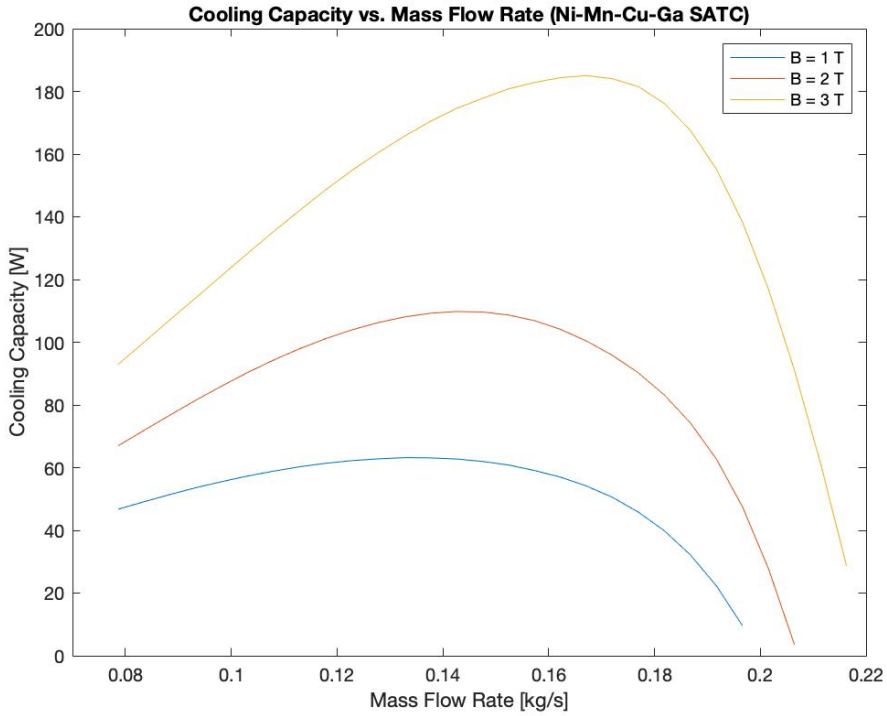

Figure 41: $Ni_{0.50}Mn_{0.19}Cu_{0.06}Ga_{0.25}$ (SATC) cooling capacity vs. mass flow rate for varying magnetic field strength.

In *Fig. 41* the cooling capacity's evolution with mass flow rate for the three tested magnetic field strengths is presented. Due to the peak heat capacity being much larger than that of gadolinium, there is a larger range of flow rates for the same simulated range of utilization factor values. This indicates that the Ni-Mn-Cu-Ga alloy can withstand higher rates of fluid flow during a blow period before overwhelming the regenerative capacity of the MCM bed. Of main interest is the performance of the material at the 2 T field strength, as this is closest to the current maximum obtainable magnetic field is

prototype AMRs. The maximum cooling capacity is ~110 W for a mass flow rate of ~0.14 kg/s.

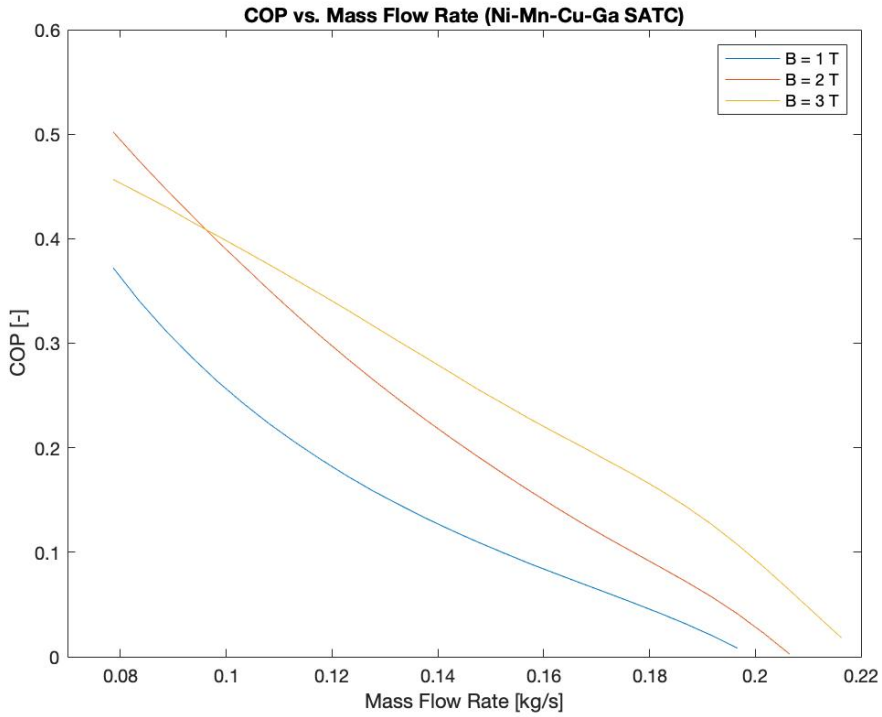

Figure 42: $Ni_{0.50}Mn_{0.19}Cu_{0.06}Ga_{0.25}$ (SATC) COP vs. mass flow rate for varying magnetic field strength.

Fig. 42 shows the efficiency of the Ni-Mn-Cu-Ga alloy as a function of mass flow rate. In the low flow rate regime, it can be seen that the simulation for the 2 T magnetic field is slightly more efficient than that of the 3 T case. This is likely due to the influence of the heat capacity over the selected operating temperature span. As flow rate increases the efficiency of the material for the 2 T simulation decreases more rapidly than that of the 3 T simulation. The maximum efficiency achieved by this material is ~0.5 for a magnetic field strength of 2 T.

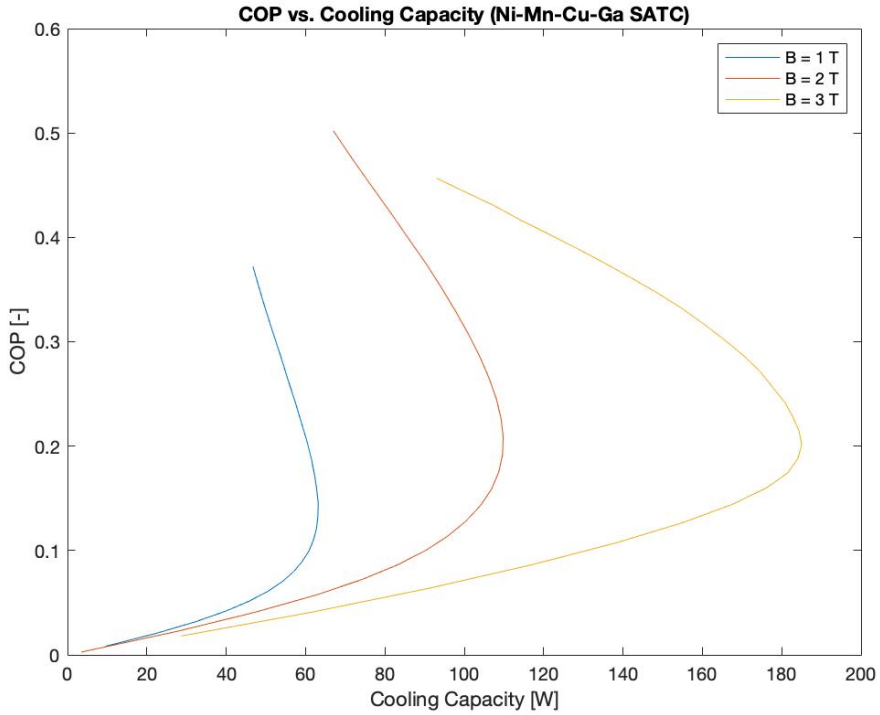

Figure 43: $Ni_{0.50}Mn_{0.19}Cu_{0.06}Ga_{0.25}$ (SATC) COP vs. cooling capacity for varying magnetic field strength.

Once again, it can be seen that AMRs operating with larger magnetic field strengths can achieve greater cooling capacities and maintain higher efficiencies over a larger range of mass flow rates. However, there is not a substantial increase in efficiency as the magnetic field strength increases. These relatively low efficiencies can be attributed to the material's less than desirable magnetothermal properties. The adiabatic temperature change has a low magnitude peak and does not cover a large range of temperatures, putting a strict limitation on its operative temperature range. Also contributing to this is the material's heat capacity, which shows drastic changes in magnitude over the selected operating temperatures.

In order to further explore the effects that heat capacity can have on a magnetocaloric material's performance, a hypothetical material is simulated by creating

artificial adiabatic temperature change and heat capacity curves. Both of these curves are created using a Gaussian function of the form:

$$f(x) = ae^{-(x-b)^2/2c^2} \tag{58}$$

where *f(x)* is either the adiabatic temperature change or heat capacity and *x* spans values from -1 to 1. The arbitrary variables *a*, *b*, and *c* are used to alter the peak value, the position of the peak, and the width of the curve respectively. Once the curves have been generated, they are plotted over a 20 K temperature span from 310-330 K. The values of *a*, *b*, and *c* used to compute the hypothetical adiabatic temperature changes and heat capacities are given in *Tab. 8*.

Table 8: Gaussian function constants for the hypothetical material simulations.

Quantity	***a***	***b***	***c***
Adiabatic Temperature Change	5	0	0.20
	4		0.18
	3		0.16
	2		0.14
Heat Capacity (During Cold Blow)	500	-0.3	0.35
Heat Capacity (During Warm Blow)	450	0	0.35
	400		
	350		
	300		
	250		

The adiabatic temperature changes range in peak values from 5 K to 2 K, with a corresponding decrease in curve widths for each 1 K decrease in peak height. The width of these curves are set to decrease with decreasing peak height to more closely resemble the behavior of adiabatic temperature change curves observed in real magnetocaloric

materials. Plots of the adiabatic temperature change curves used for the hypothetical simulations are shown in *Fig. 44*.

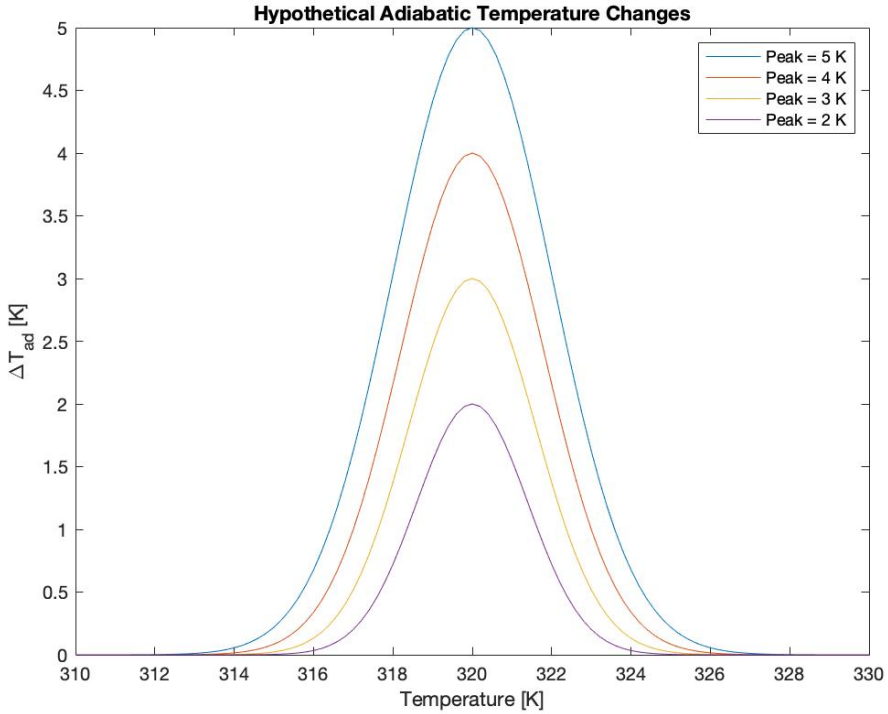

Figure 44: Hypothetical adiabatic temperature change curves.

A single heat capacity curve for the cold blow is created, as well as five different warm blow heat capacities of decreasing peak height. All heat capacity curves are set at a baseline of 100 J/kg•K, rather than approaching zero, to more closely mimic the behavior of heat capacity curves observed on FOMT materials. The heat capacity curve created for the cold blow (zero field) is offset to the left from the warm blow heat capacity curves by 3 K, while the warm blow heat capacities peak at the same temperature as the adiabatic temperature changes. The generated heat capacities used for the hypothetical material study are presented in *Fig. 45*.

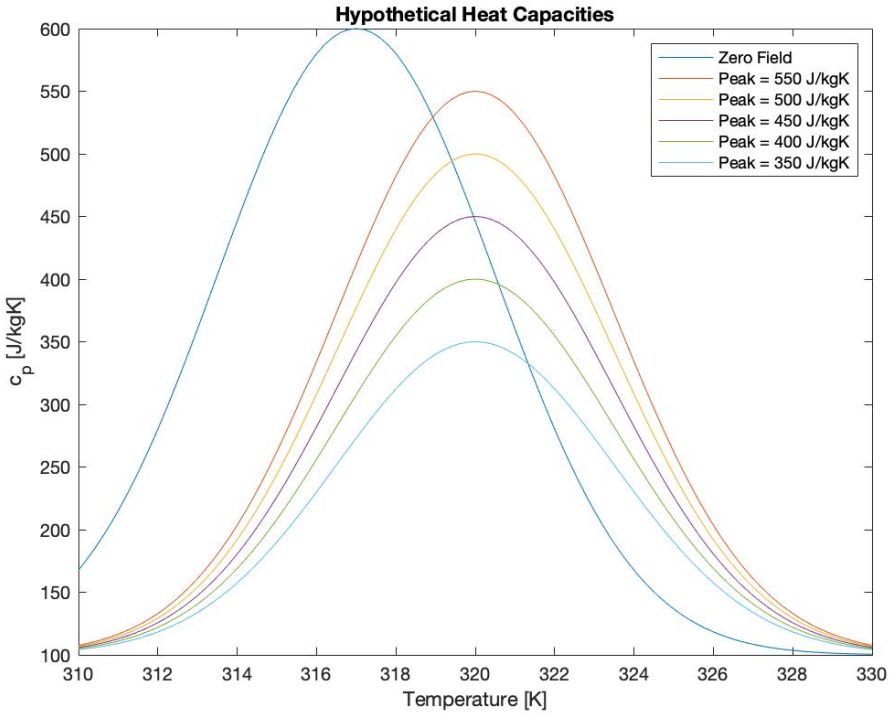

Figure 45: Hypothetical heat capacity curves.

The goal of the hypothetical material study is to determine the effect that heat capacity has on overall MCM performance. To study this, simulations were run using material properties, the mass density and thermal conductivity, similar to those of the Ni-Mn-Cu-Ga alloy. The hypothetical material was assigned a mass density of 8000 kg/m^3 and a thermal conductivity of 9 W/m•K. The same operational parameters used for the Ni-Mn-Cu-Ga alloy simulations are used for the hypothetical material simulations, with the exception of the operational temperature. For this study, a single operational temperature span of 44.85-48.85 °C (318-322 K) and mass flow rate of 0.0689 kg/s is considered for all simulated adiabatic temperature changes and heat capacities. The results of the hypothetical study are shown in *Fig. 46*.

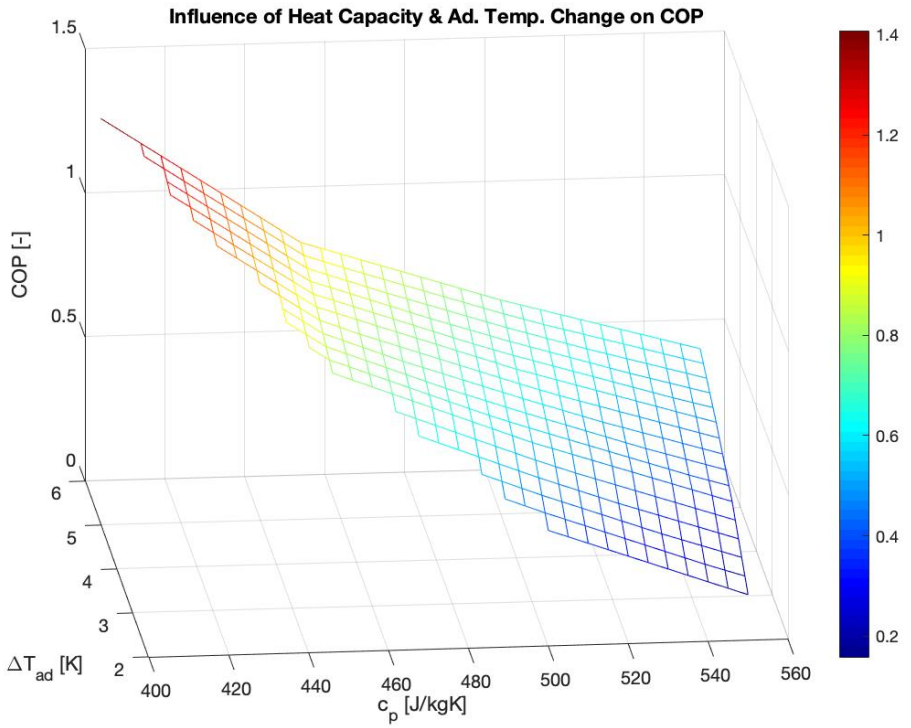

Figure 46: COP as a function of heat capacity and adiabatic temperature change for hypothetical material.

It is typical when selecting a MCM for use in an AMR cooling system to only consider the magnitude of the adiabatic temperature change as the main indicator of how well the material will perform. However, the magnitude of the heat capacity also plays an important role, as can be seen from *Fig. 46*. As to be expected, materials with a large adiabatic temperature change and low heat capacity will show the best overall efficiency. The results of this study also show that similar efficiencies can be achieved with materials that have a smaller adiabatic temperature change and lower heat capacity when compared to a material with a larger adiabatic temperature change and higher heat capacity.

This study also reveals a downfall of small adiabatic temperature change materials. As the change in heat capacity becomes greater between the warm and cold

blows, materials with a small adiabatic temperature change are unable to preserve the temperature span across the regenerator. This is visualized in *Fig. 46* with the jagged edges that appear on the front side of the surface plot. Therefore, even though comparable efficiencies can be produced between materials with smaller adiabatic temperature changes/low heat capacity and larger adiabatic temperature changes/high heat capacity, there exists a point where this combination becomes insufficient and cooling can no longer take place.

VI. CONCLUSIONS AND FUTURE WORK

Comparing the results of the mean-field model developed in this thesis to those of Bouchekara and Nahas [23] and the experimental measurements of gadolinium performed by Dan'Kov et al [20], a substantial amount of agreement can be seen. Therefore, the developed mean-field model is verified to provide physically meaningful data for use in an AMR simulation. Inclusion of the electronic contribution to the total entropy did not have a major impact on the overall results. The heat capacity at each magnetic field strength increased by ~20 J/kgK when this term was included. The adiabatic temperature change peak values also increased on average by ~1 K, but increased by larger amounts for larger magnetic field strengths.

In the 1D AMR simulations using gadolinium as the regenerator material the general AMR performance trends were established, and the model is verified according to similar studies, namely those of Borbolla [4] and Tagliafico et al [28]. Low flow rates offer the best efficiency at the cost of lower cooling capacities, so a compromise must be made to best suit the specific application. Simulations which varied the operating frequency and regenerator MCM mass found that a frequency of 1 Hz offers the best performance for reasonably low flow rates and that increasing the amount of MCM mass provides higher cooling capacities with better efficiency. Across all simulations, AMR performance is greatly increased for larger magnetic field strengths and smaller operating temperature spans.

From the simulations of the $Ni_{0.50}Mn_{0.19}Cu_{0.06}Ga_{0.25}$ alloy after SATC, its performance as a regenerator material is determined. The material was seen to have moderate cooling capacities but suffered from relatively low operating efficiencies. Since

the adiabatic temperature change curves for this material covered a much smaller range of temperatures, small operative temperature spans had to be used. As a single regenerator material, the $Ni_{0.50}Mn_{0.19}Cu_{0.06}Ga_{0.25}$ alloy would not be a sufficient.

In the simulations performed for a hypothetical material, the influence of heat capacity on MCM performance is established. It is found that the magnitude of heat capacity plays a vital role in a magnetocaloric material's performance. Similar efficiencies produced by a material with a larger adiabatic temperature change and higher heat capacity can be achieved by a material with a smaller adiabatic temperature change and lower heat capacity. Materials with a large adiabatic temperature change are still more desirable, as they are capable of maintaining the regenerator temperature span at lower heat capacities than materials with smaller adiabatic temperature changes.

Future work will involve the further development of magnetocaloric materials to be tested for performance in the AMR simulation. In the magnetic cooling community, there is much work underway to improve upon the magnetothermal properties of existing magnetocaloric materials. Modifications can also be made to the AMR simulation in order to more closely resemble physical AMR prototypes or test other regenerator geometries. The current implemented model does not take into account the many loss factors that burden AMR prototypes, and in this way will overpredict the performance of tested materials. Loss factors such as heat transfer with the regenerator casing and the effect of fluid flow in void volumes between the regenerator and heat exchangers could be implemented to more closely match the results of real AMR systems. The simulation can also be changed to model other regenerator bed geometries, through modifying the

Reynolds number and pressure drop correlations, so that the performance of varying geometries can be determined.

VII. REFERENCES

[1] G. V. Brown. *Magnetic Heat Pumping Near Room Temperature*. Journal of Applied Physics, 47 (1976) 3673-3680.

[2] R. Gimaev, Y. Spichkin, B. Kovalev, K. Kamilov, V. Zverev, and A. Tishin. *Review on Magnetic Refrigeration Devices Based on HTSC Materials*. International Journal of Refrigeration, 100 (2019) 1-12.

[3] S. Jacobs, J. Auringer, A. Boeder, J. Chell, L. Komorowski, J. Leonard, S. Russek, and C. Zimm. *The Performance of a Large-scale Rotary Magnetic Refrigerator*. International Journal of Refrigeration, 37 (2014) 84-91.

[4] I. M. Borbolla. *Assessment of Magnetic Cooling for Domestic Applications*. MS Thesis. KTH Royal Institute of Technology, Stockholm, 2013. ResearchGate.

[5] A. M. Tishin and Y. I. Spichkin. *The Magnetocaloric Effect and its Applications*. Series in Condensed Matter Physics, (2003).

[6] C. Aprea, A. Greco, and A. Maiorino. *Modelling an Active Magnetic Refrigeration System: A Comparison with Different Models of Incompressible Flow Through a Packed Bed*. Applied Thermal Engineering, 36 (2012) 296-306.

[7] P. V. Trevizoli. *Development of Thermal Regenerators for Magnetic Cooling Applications*. PhD Thesis. Federal University of Santa Catarina, 2015. ResearchGate.

[8] D. S. Arnold, A. Tura, A. Ruebsaat-Trott, and A. Rowe. *Design Improvements of a Permanent Magnet Active Magnetic Refrigerator*. International Journal of Refrigeration, 37 (2014) 99-105.

[9] U. Legait, F. Guillou, A. Kedous-Lebouc, V. Hardy, and M. Almanza. *An Experimental Comparison of Four Magnetocaloric Regenerators Using Three Different Materials*. International Journal of Refrigeration, 37 (2014) 147-155.

[10] T. Kawanami, K. Chiba, K. Sakurai, and M. Ikegawa. *Optimization of a Magnetic Refrigerator at Room Temperature for Air Cooling Systems*. International Journal of Refrigeration 29 (2006) 1294-1301.

[11] L. A. Tagliafico, F. Scarpa, F. Valsuani, and G. Tagliafico. *Preliminary Experimental Results from a Linear Reciprocating Magnetic Refrigerator Prototype*. Applied Thermal Engineering, 52 (2013) 492-497.

[12] M. Balli, O. Sari, C. Mahmed, Ch. Besson, Ph. Bonhote, D. Duc, and J. Forchelet. *A Pre-industrial Magnetic Cooling System for Room Temperature Application*. Applied Energy, 98 (2012) 556-561.

[13] A. Czernuszewicz, J. Kaleta, M. Królewicz, D. Lewandowski, R. Mech, and P. Wiewiórski. *A Test Stand to Study the Possibility of Using Magnetocaloric Materials for Refrigerators*. International Journal of Refrigeration, 37 (2014) 72-77.

[14] J. Tušek, S. Zupan, A. Šarlah, I. Prebil, and A. Poredoš. *Development of a Rotary Magnetic Refrigerator*. International Journal of Refrigeration, 33 (2010) 294-300.

[15] Z. Li, J. Shen, K. Li, X. Gao, X. Guo, and W. Dai. *Assessment of Three Different Gadolinium-based Regenerators in a Rotary-type Magnetic Refrigerator*. Applied Thermal Engineering, 153 (2019) 159-167.

[16] T. Okamura, K. Yamada, N. Hirano, and S. Nagaya. *Performance of a Room-temperature Rotary Magnetic Refrigerator*. International Journal of Refrigeration, 29 (2006) 1327-1331.

[17] X. N. He, M. Q. Gong, H. Zhang, W. Dai, J. Shen, and J. F. Wu. *Design and Performance of a Room-temperature Hybrid Magnetic Refrigerator Combined with Stirling Gas Refrigeration Effect*. International Journal of Refrigeration, 36 (2013) 1465-1471.

[18] K. Engelbrecht. *A Numerical Model of an Active Magnetic Regenerator Refrigerator with Experimental Validation*. PhD Thesis. University of Wisconsin-Madison, 2008.

[19] K. L. Engelbrecht, G. F. Nellis, S. A. Klein, and C. B. Zimm. *Recent Developments in Room Temperature Active Magnetic Regenerative Refrigeration*. HVAC&R Research, 13 (2007) 525-542.

[20] S. Yu. Dan'Kov, A. M. Tishin, V. K. Pecharsky, and K. A. Gschneidner. *Magnetic Phase Transitions and the Magnetothermal Properties of Gadolinium*. Physical Review B, 56 (1998) 3478-3490.

[21] S. Stadler, M. Khan, J. Mitchell, N. Ali, A. M. Gomes, I. Dubenko, A. Y. Takeuchi, and A. P. Guimarães. *Magnetocaloric Properties of $Ni_2Mn_{1-x}Cu_xGa$*. Applied Physics Letters, 88 (2006) 192511.

[22] M. V. McLeod, A. K. Giri, B. A. Patterson, C. L. Dennis, L. Zhou, S. C. Vogel, O. Gourdon, H. M. Reiche, K. C. Cho, Y. H. Sohn, R. D. Shull, and B. S. Majumdar. *Magnetocaloric Response of Non-stoichiometric Ni_2MnGa Alloys and the Influence of Crystallographic Texture*. Acta Materialia, 97 (2015) 245-256.

[23] H. Bouchekara and M. Nahas. *Magnetic Refrigeration Technology at Room Temperature*. InTech, 10 (2012) 225-251.

[24] G. Grosso and G. P. Parravicini. *Solid State Physics Second Edition*. Academic Press, (2014) 731-739.

[25] N. Wakao, S. Kaguei, and T. Funazkri. *Effect of Fluid Dispersion Coefficients on Particle-to-Fluid Heat Transfer Coefficients in Packed Beds*. Chemical Engineering Science, 34 (1979) 325-336.

[26] M. Frischmann, K. Engelbrecht, G. Nellis, and S. Klein. *Heat Transfer Coefficient in a Packed Sphere Regenerator for Use in Active Magnetic Regenerative Refrigeration*. International Refrigeration and Air Conditioning Conference, (2008) 1-8.

[27] Y. Feng, B. Yu, M. Zou, and D. Zhang. *A Generalized Model for the Effective Thermal Conductivity of Porous Media Based on Self-similarity*. Journal of Physics D: Applied Physics, 37 (2004) 3030-3040.

[28] A. Tura and A. Rowe. *Progress in the Characterization and Optimization of Permanent Magnet Magnetic Refrigerator*. 3rd International Conference on Magnetic Refrigeration, Des Moines, 11-15 May 2009.

[29] G. Tagliafico, F. Canepa, and F. Scarpa. *A Dynamic 1-D Model for a Reciprocating Active Magnetic Regenerator; Influence of the Main Working Parameters*. International Journal of Refrigeration, 33 (2010) 286-293.

[30] J. Yang, Q. Wang, M. Zeng, and A. Nakayama. *Computational Study of Forced Convective Heat Transfer in Structured Packed Beds with Spherical or Ellipsoidal Particles*. Chemical Engineering Science, 65 (2010) 726-738.

[31] S. Fabbrici, G. Porcari, F. Cugini, M. Solzi, J. Kamarad, Z. Arnold, R. Cabassi, and F. Albertini. *Co and In Doped Ni-Mn-Ga Magnetic Shape Memory Alloys: A Thorough Structural, Magnetic, and Magnetocaloric Study*. Entropy, 16 (2014) 2204-2222.

APPENDIX A

Mean-Field Model Matlab Code

```
% General Physical Constants %
R = 8.314; % universal gas constant [J/mol*K]
NA = (6.022*10^23); % Avogadro constant [atoms/mol]
kB = R/NA; % Boltzmann constant [J/K]
mu0 = (4*pi*10^-7); % permeability of free space [T*m/A]
q_e = 1.602177*10^-19; % elementary charge [C]
m_e = 9.109384*10^-31; % electron rest mass [kg]
hbar = 1.054572*10^-34; % reduced Planck constant [J*s]
muB = (q_e*hbar)/(2*m_e); % Bohr magneton [J/T]

% Gadolinium Property Constants %
TD = 184; % Debye temperature [K]
gL = 2; % Landé factor [-]
J = 3.5; % total angular momentum [N*m*s]
TC = 293; % Curie temperature [K]
MM = 0.157; % molar mass [kg/mol]
p = 7900; % density [kg/m^3]
N = p*NA/MM; % atoms per volume [atoms/m^3]
c_el = 0.0108784; % electronic heat capacity coefficient [J/mol*K^2]

load('SmGd0T.mat') % gadolinium zero field magnetic entropy

% Input Magnetic Field %
B = 2; % magnetic field strength [T]

% Temperature Inputs %
T_start = 5; % initial temperature [K]
T_stop = 350; % final temperature [K]
nn = (T_stop-T_start+1); % setting spacing between temperatures to be 1
T = linspace(T_start,T_stop,nn); % temperature array
xroot = zeros(1,length(T)); % initializing "xroot" array for loop
int = zeros(1,length(T)); % initializing "int" array for loop

for ii = 1:length(T) % setting index to run from 1st to last element of
T

b1 = ((2*J+1)/(2*J)); % first Brillouin coefficient
b2 = (1/(2*J)); % second Brillouin coefficient

if B == 0 && T(ii)<TC % ferromagnetic region
        cW = (3*kB*TC)/(NA*(gL*muB)^2*J*(J+1)); % molecular field
constant
        A = (kB.*T(ii))/(NA*(gL*muB*J)^2*cW); % slope of linear
function
        D = B/(NA*gL*muB*J*cW); % y-intercept of linear function
    else % paramagnetic region
        A = 0; % slope of linear function
        D = 0; % y-intercept of linear function
end
```

```
if B>0 % any nonzero field value
        cW = (3*kB*TC)/(NA*(gL*muB)^2*J*(J+1)); % molecular field
constant
        A = (kB.*T(ii))/(NA*(gL*muB*J)^2*cW); % slope of linear
function
        D = B/(NA*gL*muB*J*cW); % y-intercept of linear function
end

sig1 = @(X) b1*coth(b1*X) - b2*coth(b2*X); % 1st reduced magnetization
function
sig2 = @(X) A.*X - D; % 2nd reduced magnetization function

% A guess value of "100" may be used for temperatures between, and
% including, 5 - 11.
% A guess value of "30" may be used for temperatures between, and
% including, 12 - 186.
% A guess value of "3" may be used for temperatures between, and
% including, 187 - 290.

if T(ii)<=11 && B == 0
        guess = 100;
    elseif T(ii)>=12 && T(ii)<=186 && B == 0
        guess = 30;
    elseif T(ii)>=187 && T(ii)<=290 && B == 0
        guess = 3;
    elseif T(ii)>=291 && T(ii)<=292 && B == 0
        guess = 0.3;
    elseif T(ii)>=TC && B == 0
        xroot(ii) = 0;
end

if T(ii)<=70 && B>0
        guess = 100;
    elseif T(ii)>=71 && T(ii)<=350 && B>0
        guess = 10;
end

% Finding the value of the Brillouin function argument where the two
% reduced magnetization functions are equal to one another.
xroot(ii) = fzero(@(X)sig1(X)-sig2(X),guess);

% Solving the integral located in the lattice entropy expression %
fun = @(y) ((y.^3)./(exp(y)-1)); % integrand
ymin = 0; % lower limit of integration
ymax = TD/T(ii); % upper limit of integration
int(ii) = integral(fun,ymin,ymax); % integral solution

B_J = b1*coth(b1*xroot) - b2*coth(b2*xroot); % Brillouin function

a1 = sinh(b1*xroot); % term for magnetic entropy expression
a2 = sinh(b2*xroot); % term for magnetic entropy expression

% Expressions for the entropy contributions %

S_m = R*(log(a1./a2)-xroot.*B_J); % magnetic specific entropy [J/mol*K]
```

```
S_lat = R*(((12*((T./TD).^3)).*int)-(3*log(1-exp(-TD./T)))); % lattice
specific entropy [J/mol*K]
S_el = c_el.*T; % electronic specific entropy [J/mol*K]
S_Tot = S_m + S_lat + S_el; % total specific entropy [J/mol*K]

end

% MFM Thermodynamic Properties Calculations %
Magz = NA*gL*muB*J*B_J; % magnetization [A/m] or [emu/g]
plot(T,Magz)

dS_Tot = diff(S_Tot); % change in total specific entropy [J/mol*K]
% Note: Using this numerical method of calculating the 1st derivative
to
% get the change in entropy causes its solution array to have one less
% element than the temperature array (the first point is excluded). So,
in
% order to plot quantities that depend on "dS_Tot", you must exclude
the
% first temperature element to avoid getting an error message.

cp = T(1:end-1).*dS_Tot./MM; % specific heat capacity [J/kg*K]
%plot(T(2:end),cp)

dS_m = -(S_m - S_m0); % change in magnetic specific entropy [J/mol*K]
dS_mkg = dS_m/MM; % change in magnetic specific entropy [J/kg*K]
%plot(T,dS_mkg)

dT_ad = (T(1:end-1)./cp).*dS_mkg(1:end-1); % adiabatic temperature
change [K]
%plot(T(2:end),dT_ad)
```

APPENDIX B

1D AMR Simulator Matlab Code

```
% Input Values %
f = 1; % cycle frequency [Hz]
HotTemp = 49; % HHEX temperature [K]
ColdTemp = 45; % CHEX temperature [K]
HTF = 1; % heat transfer fluid selection
Uf = linspace(0.5,2,49); % utilization factor range [-]
asprat = 3; % aspect ratio [-]
m_MCM = 0.75; % mass of MCM [kg]
res = 110; % spatial resolution
prec = 1e-6; % steady-state precision
MCM = 4; % MCM selection

% Initializing terms that are updated after each loop %
MFR = zeros(1,length(Uf));
Qr = zeros(1,length(Uf));
Qc = zeros(1,length(Uf));
W_mag = zeros(1,length(Uf));
COP = zeros(1,length(Uf));
W_pump = zeros(1,length(Uf));
warm(75,res,2,length(Uf)) = -1;
cold(75,res,2,length(Uf)) = -1;
ii = 1; % indexing variable

% Loading in Material Data %
load('GdSimDataV2')
load('Cu6AbaSimData')
load('Cu6AAdTempfits')
load('Cu6AHeatCapfits1')
load('HypAdTemps1')
load('HypTest_350')

% MCM Properties %

if MCM == 1 % Gadolinium
    p_s = 7900; % mass density [kg/m^3]
    k_s = 10.6; % thermal conductivity [W/m*K]
    cs_max = 303.5696; % max specific heat capacity at zero field
[J/kg*K]
    Material = 'Gadolinium';
elseif MCM == 2 % Cu6A As Recieved (AR)
    p_s = 8185.6; % mass density [kg/m^3]
    k_s = 8.8867; % thermal conductivity avg. from 300-340K [W/m*K]
    cs_max = 894.0333; % max specific heat capacity at zero field
[J/kg*K]
    Material = 'Cu6A AR';
elseif MCM == 3 % Cu6A after SATC
    p_s = 8001.6; % mass density [kg/m^3]
    k_s = 8.8867; % thermal conductivity avg. from 300-340K [W/m*K]
    cs_max = 684.9377; % max specific heat capacity at zero field
[J/kg*K]
    Material = 'Cu6A SATC';
```

```
elseif MCM == 4 % Hypothetical Material
    p_s = 8000; % mass density [kg/m^3]
    k_s = 9; % thermal conductivity [W/m*K]
    cs_max = 600; % max specific heat capacity at zero field [J/kg*K]
    Material = 'Hypothetical';
end

% Regenerator Geometry Properties %
d = ((4.*m_MCM)./(pi.*p_s.*asprat)).^(1/3); % regenerator bed diameter
[m]
L_reg = d.*asprat; % regenerator length [m]
A_cs = pi.*(d./2).^2; % regenerator cross-sectional area [m^2]
dp = 400e-6; % mean particle diameter [m]
eps = 0.36; % porosity [-]
dh = ((2/3).*eps.*dp)./(1-eps); % hydraulic diameter [m]
a_surf = 6.*(1-eps)./dp; % volume specific surface area [m^-1]

% Pressure Drop Terms
ce1 = 133; % Ergun constant term [-]
ce2 = 2.33; % Ergun constant term [-]
pump_eff = 0.8; % pump efficiency [-]

% Fluid Properties %

if HTF == 1 % Water
    p_f = 1000; % mass density [kg/m^3]
    %mu_f = 8.2373e-4; % dynamic viscosity [kg/m*s]
    mu_f = 9.77e-4; % dynamic viscosity [kg/m*s]
    k_f = 0.59803; % thermal conductivity [W/m*K]
    c_f = 4180; % specific heat capacity [J/kg*K]
    Pr = c_f.*mu_f./k_f; % Prandtl number [-]
    Fluid = 'Water';
elseif HTF == 2 % 50-50 water-glycol mixture
    p_f = 1082; % mass density [kg/m^3]
    mu_f = 7.5e-4; % dynamic viscosity [kg/m*s]
    k_f = 0.402; % thermal conductivity [W/m*K]
    c_f = 3260; % specific heat capacity [J/kg*K]
    Pr = c_f.*mu_f./k_f; % Prandtl number [-]
    Fluid = '50-50 water-glycol mixture';
end

while ii <= length(Uf)
    UtilizationFactor = Uf(ii);
    t_blow = 0.5/f; % blow time [s]
    mdot = UtilizationFactor./(t_blow.*c_f./(L_reg.*A_cs.*(1-
eps).*p_s.*cs_max)); % mass flow rate [kg/s]
    MFR(ii) = mdot;
    v_D = mdot./(A_cs*p_f);
    vel = v_D./eps; % Interstitial velcoity [m/s]
    Re = (p_f.*v_D.*dh)./(mu_f.*eps); % Reynolds number [-]
    Nu = 0.7*Pr.^(0.23)*Re.^(0.6); % Nusselt number correlation (Wakao)
[-]

    % Differential Equation Terms %
    h = Nu.*k_f./dh; % heat transfer coefficient [W/m^2*K]
    keff_f = (eps.*k_f)+(0.5.*k_f.*Pr.*Re.*(dp./dh)); % effective fluid
thermal conductivity [W/m*K]
```

```
    keff_s = (1-eps).*k_s; % effective solid thermal conductivity
[W/m*K]
    b1 = (h.*a_surf.*L_reg)./(p_f.*c_f.*eps.*vel);
    b2 = 1;
    b3 = keff_f./(p_f.*c_f.*eps.*L_reg.*vel);
    b4 = (h.*a_surf.*L_reg)./(p_s.*(1-eps).*vel); % w/out MCM heat
capacity
    b5 = keff_s./(p_s.*(1-eps).*L_reg.*vel); % w/out MCM heat capacity

    % Temperature Parameters %
    T_hot = 273.15 + HotTemp; % room (heat sink) temperature [K]
    T_cold = 273.15 + ColdTemp; % cold reservoir (load) temperature [K]
    % Initial Temperature Profile
    T(1,:) = linspace(T_cold,T_hot,res)'; % fluid temperature [K]
    T(2,:) = T(1,:); % MCM (solid) temperature [K]
    T = (T - T_cold)./(T_hot - T_cold); % normalized temperature [-]
    % Temperature definitions for MCM property data
    Tfn_cp = (Tfncp - T_cold)./(T_hot - T_cold); % temperatures for
heat capacity data [-]
    Tfn_ad = (T_dTad - T_cold)./(T_hot - T_cold); % temperatures for
adiabatic temperature change [-]
    Tfn_Cu6A = (T_Cu6A - T_cold)./(T_hot - T_cold); % temperatures used
for Cu6A thermo props [-]
    Tfn_fit = (fitTemp - T_cold)./(T_hot - T_cold); % temperatures for
fitted Cu6A data [-]
    Tfn_hyp = (temphyp - T_cold)./(T_hot - T_cold); % temperatures for
hypothetical material [-]

    % Position and Time Inputs %
    x = linspace(0,1,res); % normalized position along regenerator [-]
    t_rd = L_reg./vel; % normalized time along regenerator [s]
    t_start = 0; % starting time [-]
    t_stop = t_blow./t_rd; % stopping time [-]
    t = linspace(t_start,t_stop,75); % dimensionless time vector

    % Pressure Drop (Ergun) %
    delP = 0.5.*(p_f./dh).*((ce1./Re)+ce2).*((v_D./eps).^2); % pressure
drop [Pa]
    W_p = mdot.*delP./(pump_eff.*p_f); % pumping power [W]
    W_pump(ii) = W_p*L_reg; % Storing the pumping powers values into a
vector.

    % Start of Simulation %

    tic
    for N_Cycles = 1:250 % Setting max number of cycles
        T_sim = T; % storing the previous cycle's temperature

        % Step 1: Magnetization
        T(2,:) = T(2,:) + interp1(Tfn_hyp',dT_5hm',T(2,:))./(T_hot-
T_cold);

        % Step 2: Warm Blow
        [sol_warm,T,Q_rej] = ...

warmblowfn(x,t,T,b1,b2,b3,b4,b5,cp_F,Tfn_hyp,T_cold,T_hot,mdot,c_f,t_rd
);
```

```
        % Step 3: Demagnetization
        T(2,:) = T(2,:) - interp1((temphyp'+dT_5hm'-T_cold)./(T_hot-
T_cold),dT_5hm',T(2,:))./(T_hot-T_cold);

        % Step 4: Cold Blow
        [sol_cold,T,Q_ref] = ...
            coldblowfn(x,t,T,b1,-
b2,b3,b4,b5,cp_NF,Tfn_hyp,T_cold,T_hot,mdot,c_f,t_rd);

        % Test for Steady State %
        ctl = max(abs(T_sim(2,:)-T(2,:))./T(2,:));
        if ctl < prec && N_Cycles > 60
            disp('The temperatures have reached steady state
conditions!')
            break
        end
        ctl1 = ctl;

    end
    toc

    Qr(ii) = Q_rej; % Storing the rejected heat values into a vector
    Qc(ii) = Q_ref; % Storing the absorbed heat values into a vector
    W_mag(ii) = Qr(ii)+Qc(ii); % Calculating and storing the magnet
work values into a vector
    COP(ii) = -Q_ref./(Q_rej+Q_ref+W_p); % Storing the COP values into
a vector
    warm(:,:,:,ii) = sol_warm; % Storing the warm blow solutions into a
4D matrix
    cold(:,:,:,ii) = sol_cold; % Storing the cold blow solutions into a
4D matrix
    ii = ii+1; % increasing the indexing variable to populate vectors
end
```

Warm Blow Function

```
function [sol,T,Q_rej] = ...

warmblowfn(x,t,T,b1,b2,b3,b4,b5,cp_F,Tfn_hyp,T_cold,T_hot,mdot,c_f,t_rd
)

c_p = cp_F; % setting the heat capacity for the MCM (field on)
options = odeset('RelTol',5e-3,'AbsTol',1e-5); % setting ode options
sol = pdepe(0,@(f1,f2,f3,f4) ...
    pdex1pde(f1,f2,f3,f4,b1,b2,b3,b4,b5,c_p,Tfn_hyp),@(x1)
pdex1ic(x1,T,x),...
    @(xl,ul,xr,ur,t) pdex1bc(xl,ul,xr,ur,t,T_cold),x,t,options);

% Initializing the variables for the next step of the function
T = [];
T(1,:) = sol(end,:,1); % fluid temperatures
T(2,:) = sol(end,:,2); % solid temperatures
T_rej = sol(:,end,1);
int_rej = mean((T_hot-T_cold)*(T_rej-1));
Q_rej = mdot*c_f*0.5*int_rej; % Calculating rejected heat

% ------------------------------------------------------------------------
- %

function [c,f,s] = pdex1pde(x,t,u,dudx,b1,b2,b3,b4,b5,cp_F,Tfn_hyp)
c = [1 1]'; % terms in front of the time derivatives (left side of eq.)
cp_w = interp1(Tfn_hyp,cp_F,u(2)); % defining the MCM heat capacity for
"f"
f = [b3;b5./cp_w].*dudx; % flux term (terms multiplied by 2nd spatial
derivative)
s = [b1.*(u(2)-u(1))-b2.*dudx(1);(b4./cp_w).*(u(1)-u(2))]; % source
term
% "s" is any term not multiplied by a 2nd spatial derivative on the
right
% side of the eq.

% ------------------------------------------------------------------------
- %

function u0 = pdex1ic(x1,T,x)
if length(T(1,:)) == 100
    u0 = interp1(linspace(0,1,100),T',x1)';
else
    u0 = interp1(x,T',x1)';
end
% This step of the function defines the initial conditions for the
% temperatures.

% ------------------------------------------------------------------------
- %

function [pl,ql,pr,qr] = pdex1bc(xl,ul,xr,ur,t,T_cold)
pl = [ul(1); 0];
ql = [0; 1];
pr = [0; 0];
```

```
qr = [1; 1];
% This step of the function defines the boundary conditions for the two
% governing equations.

% The terms "pl" and "ql" refer to the left boundary
% and the terms "pr" and "qr" refer to the right boundary.

% The first entry within the brackets correspond to the fluid
temperature,
% and the second entry corresponds to the solid temperature.
```

Cold Blow Function

```
function [sol,T,Q_ref] = ...

coldblowfn(x,t,T,b1,b2,b3,b4,b5,cp_NF,Tfn_hyp,T_cold,T_hot,mdot,c_f,t_r
d)

c_p = cp_NF;% setting the heat capacity for the MCM (field off)
options = odeset('RelTol',5e-3,'AbsTol',1e-5); % setting ode options
sol = pdepe(0,@(f1,f2,f3,f4) ...
    pdex1pde(f1,f2,f3,f4,b1,b2,b3,b4,b5,c_p,Tfn_hyp),@(x1)
pdex1ic(x1,T,x),...
    @(xl,ul,xr,ur,t) pdex1bc(xl,ul,xr,ur,t,T_cold),x,t,options);

% Initializing the variables for the next step of the function
T = [];
T(1,:) = sol(end,:,1); % fluid temperatures
T(2,:) = sol(end,:,2); % solid temperatures
T_ref = sol(:,1,1);
int_ref = mean((T_hot-T_cold)*T_ref);
Q_ref = mdot*c_f*0.5*int_ref; % Calculating absorbed heat

% ------------------------------------------------------------------
- %

function [c,f,s] = pdex1pde(x,t,u,dudx,b1,b2,b3,b4,b5,cp_NF,Tfn_hyp)
c = [1 1]'; % terms in front of the time derivatives (left side of eq.)
cp_c = interp1(Tfn_hyp,cp_NF,u(2)); % defining the MCM heat capacity
for "f"
f = [b3;b5./cp_c].*dudx; % flux term (terms multiplied by 2nd spatial
derivative)
s = [b1.*(u(2)-u(1))-b2.*dudx(1);(b4./cp_c).*(u(1)-u(2))]; % source
term
% "s" is any term not multiplied by a 2nd spatial derivative on the
right
% side of the eq.

% ------------------------------------------------------------------
- %

function u0 = pdex1ic(x1,T,x)
if length(T(1,:)) == 100
    u0 = interp1(linspace(0,1,100),T',x1)';
else
    u0 = interp1(x,T',x1)';
end
% This step of the function defines the initial conditions for the
% temperatures.

% ------------------------------------------------------------------
- %

function [pl,ql,pr,qr] = pdex1bc(xl,ul,xr,ur,t,T_cold)
pl = [0; 0];
ql = [1; 1];
pr = [ur(1)-1; 0];
```

```
qr = [0; 1];
% This step of the function defines the boundary conditions for the two
% governing equations.

% The terms "pl" and "ql" refer to the left boundary
% and the terms "pr" and "qr" refer to the right boundary.

% The first entry within the brackets correspond to the fluid
temperature,
% and the second entry corresponds to the solid temperature.
```

APPENDIX C

Uncertainty Analysis

In order to assess the level of uncertainty in the material performance, as determined by the 1D AMR simulator, specific quantities pertaining to the magnetocaloric material were increased or decreased by 5% to represent a possible uncertainty which they may possess. These quantities include the mass density, the thermal conductivity, the heat capacity, and the adiabatic temperature change. Initially, each individual quantity was increased or decreased by 5% while all other quantities remained unchanged. This allows for the effect that each quantity has on the COP and cooling capacity to be determined, and also illuminates which quantity has the largest effect on performance. The effect of increasing and decreasing all quantities by 5% on material performance is carried out as well. The uncertainty analysis is done using gadolinium as the regenerator material using the system parameters listed in *Tab. 6*.

Increasing or decreasing the mass density of the material during a simulation had a small impact on performance. A density increase of 5% showed a decrease in COP of 1.13% and increase in cooling capacity of 2.30%, while decreasing the density showed a negligible increase in COP of 0.03% and a decrease in cooling capacity of 2.46%.

Changing the thermal conductivity had the overall lowest effect on performance. Increasing the thermal conductivity caused a decrease in both the COP and cooling capacity by 0.33% and 0.05%, respectively. By decreasing the thermal conductivity a 0.28% increase in the COP and 0.05% increase in the cooling capacity is observed.

Differences in the heat capacity influenced the performance slightly more than the previous quantities. The COP had a 0.46% increase and the cooling capacity had a 2.76% increase given the increase in heat capacity. Conversely, for a decrease in. heat capacity the COP decreased by 1.62% and the cooling capacity decreased by 2.92%.

The variation in adiabatic temperature change exhibited the largest changes to the performance metrics. The increase in adiabatic temperature change decreased the COP by 1.60% and increased the cooling capacity by 4.73%. The decrease in adiabatic temperature change increased the COP by 0.59% and decreased the cooling capacity by 4.79%.

Upon increasing all quantities by 5%, the COP displayed a 2.19% decrease and the cooling capacity displayed a 9.98% increase. By decreasing all quantities by 5% a slight decrease of 0.25% in the COP is observed as well as a 9.85% decrease in the cooling capacity.

Upon performing the uncertainty analysis it can be determined that with an uncertainty of 5% for each quantity the COP does not drastically change, remaining within a ~2% range of its original value. However, the cooling capacity does show larger variation upon varying material properties, remaining within a ~10% range of the original value. In the future, it may be useful to further investigate the uncertainty of the AMR simulator by utilizing a Monte Carlo method. In this way simulations could be run with the above quantities taking on random values within the +/- 5% range in order to see what the maximum percent difference is for the COP and cooling capacity.